

Nonlinear analysis of the solar updraft tower under static wind action

Siyu. Li

17-2-2017



Nonlinear analysis of the solar updraft tower under static wind action

by

Siyu. Li

in partial fulfilment of the requirements for the degree of

Master of Science
in Civil Engineering

at the Delft University of Technology

An electronic version of this thesis is available at
<http://repository.tudelft.nl/>.

Student: Siyu.Li
E.du Perronlaan 516
Student ID:4424638
E: lisiyu201407@gmail.com
T:(+31)(0)636032551

Thesis committee: Chair
dr. ir. J. L. Coenders
Delft Unveristy of Technology
BEMNext Laboratory
White Lioness technologies
E:J.L.Coenders@tudelft.nl

Supervisors
dr. ir. P. C. J. Hoogenboom
Delft University of Technology
P.C.J.Hoogenboom@tudelft.nl
(+31)(0)152788081

Prof. dr. ir. J. G. Rots
Delft University of Technology
E:J.G.Rots@tudelft.nl
T(+31)(0)152783799

ir. S. R. G. van Eck
Pieters Bouwtechniek B.V.
E:s.vaneck@pbt-delft.nl
T:(+31)(0)153161125

Abstract

The near future is challenging: depletion of non-renewable energy depletion, electricity shortage and sustainability give the need of developing renewable energy technology. The solar updraft tower power generation technology using solar and wind generates a reasonable amount of electricity with zero carbon footprint during operation. The working principle is rather simple: the heated air underneath a large transparent roof (air collector) is sucked into a central vertical chimney; the driven wind generates electricity by wind turbines. The solar updraft towers are mainly suitable for high power output, which also requires a large scale structure. The solar updraft tower in this research project is a 1000m reinforced concrete tall tower stiffened by ten stiffening rings every 100m.

The wind load is the most hazardous action for ultra-high ultra-thin SUT shells. The constitutive behavior of the reinforced concrete structure will give nonlinear responses under a certain wind loading level, which requires a careful study. Additionally, the SUT structural design under large wind load treated in a linear elastic stage could be costly. The dimensions of the reinforcement calculated by linear-elastic analysis can be improved by nonlinear analysis. It gives a real structural behavior including the stress redistribution caused by concrete cracking, crushing and reinforcement yielding. Nonlinear analysis can achieve a more economic design while maintaining sufficient safety.

This main thesis objective is to perform a physical nonlinear analysis of the SUT under static wind action to acquire realistic structural behavior and conduct a further optimization. A finite element model is built and a linear analysis is done for the model verification. Then a detailed linear model is built to determine the necessity of detailing the stiffening rings. The analysis shows that by detailed modeling the stiffening rings provide a higher stiffness compared to modeling the simplified way, hence improving the overall structural behavior of the Solar Updraft Tower.

A discussion about the feasibility of the chosen nonlinear material models has been done. The total strain crack rotating model is chosen whose crack is rotating continuously with the direction of principal stress. The simple working principle gives the model a robust and stable behavior. For concrete tensile behavior, a linear ultimate strain based stress-strain relation is used including the tension stiffening effect. A nonlinear stress-strain behavior is adopted for concrete in compression, considering effects of lateral crack and lateral confinement. For the reinforcement steel, elastoplastic material modeling is used with strain hardening.

Few models according to the original design of Krätzig & Partner have been built. The shell walls have a one layer reinforcement grid located at the mid-surface of the shell walls with minimum reinforcement ratio both in the meridional and the circumferential directions. The difference between these models is the way of modeling the stiffening rings: one is modeled by 3D beam elements with 1% reinforcement ratio modeled in the longitudinal direction, and the other is modeled by curved shell elements with 1% reinforcement ratio modeled both in the longitudinal direction and the transverse direction. Both models experienced a large ovalization failure mechanism at the upper cone at the serviceability limit state. This is caused by 1) the low reinforcement ratio which provides a low stiffness to the stiffening rings; 2) The eccentricity of the stiffening rings which generates a large bending moment, thus weakening the ring-wall connections. The model with beam elements showed weaker structural response than the model with curved shell elements because the beam elements do not take the transverse stiffness into consideration. The model using curved shell elements is adopted for further nonlinear analysis.

Models with increasing reinforcement ratio in two directions up to 3% on the stiffening rings are built to improve the structural behavior. The stiffness of the Solar Updraft Tower has improved, which gives less ovalization deformation. However, all models experienced the ovalization failure mechanism at a certain loading stage. Unfortunately, the concrete crushing and reinforcement yielding still

occur, even with the maximum reinforcement ratio on the stiffening rings. It is because the large bending crack at the ring-wall connection caused by the eccentricity of the stiffening rings decreases the contribution of the stiffening ring to the overall structural behavior.

Several models are built using the same reinforcement ratio in two directions on the stiffening rings with increasing tension stiffening effect. The nonlinear result shows that the influence of tension stiffening rings is high at a low loading level and is decreasing at a higher loading level.

One possibility of removing the bending failure at the ring-wall connection is to move the mass center of the cross-section of the stiffening rings to the mid-surface of the shell walls. Two re-centered models with increasing reinforcement ratio are built. With 1% reinforcement ratio, the model with re-centered stiffening ring gives a similar structural response as the original design model with a reinforcement ratio of 2%. The re-centered model with 2% reinforcement ratio gives an almost linear behavior of the structure without ovalization failure mechanism at the upper cone. No cracking is found both at the ring-wall connection and the concrete shell wall, no concrete crushing occurs and also no reinforcement is yielding. A maximum deflection around 1m meets the requirement of the maximum allowable displacement in the serviceability limit state. However, a large crack width of 1.1mm is found in the stiffening rings which should be further improved by modeling the structure using two layer reinforcement or by prestressing. Last but not least, the effect of moving the stiffening rings inside the airflow on the power output should be further investigated. But re-centering geometry gives a triple time of improvement on the structural behavior, and eventually saved a high amount of material use.

Preface

This thesis analysis the nonlinear material behavior of the solar updraft tower under static wind action and is the final part of my MSc Structural Engineering at the Delft University of Technology. The research project was carried out in collaboration with the Faculty of Civil Engineering and Geosciences and the Dutch engineering company 'Pieters Bouwtechniek'

I will thank my chairman at the Delft University of Technology, dr. ir. Jeroen Coenders, for his time and constructive comments on my thesis research. He helped in keeping me on the right track during the research.

This thesis research could not have done it without the tireless support of ir. Steven van Eck, my daily supervisor at Pieters Bouwtechniek. He had shared this knowledge in order to make me understand more about the topic. I would like to thank him for giving me substantive feedback and useful tips on my report. I am extremely grateful to him for his support both academically and otherwise.

I would also like to thank my other two committee members, Prof. dr. ir. Jan Rots, and dr. ir. Pierre Hoogenboom, whom all help in keeping me on the right track during this research project. For being several thought-provoking and fruitful discussion, they helped me in getting insight in the Finite Element Modeling.

I am very grateful to Dr. ir. Max Hendrix from the Delft University of Technology and Support Engineering Kesio Palacio at DIANA FEA BV, for continuously positive support on DIANA nonlinear material modeling.

Furthermore, I would also very much like to thank the Dutch company 'Pieters Bouwtechniek', for offering me the chance to perform my thesis within the company and providing me the chance to understand Dutch culture. I would like to thank ir. Maarten Koekoek for being a constant source of motivation and for encouraging me with your kind words during this thesis project.

Finally, I would like to express my gratitude to my parents for their love and encouragement. I would like to thank my friends Ladislav, Anand, Andrea, for providing me language feedback on my report.

Siyu. Li
Delft, January 2017

Contents

Abstract	iii
Acronyms	xi
1 Introduction	1
1.1 Possible threats to reinforced concrete solar updraft tower	1
1.2 Problem analysis	3
1.3 Research question	3
1.3.1 Main research questions	3
1.3.2 Sub research questions.	3
1.4 Research Methodology	3
1.5 The scope of the research	4
1.6 Expectations	4
1.7 Thesis layout	4
2 Geometry of Solar Updraft Tower	7
2.1 Introduction	7
2.2 Upper cone	7
2.3 Lower Hyperboloid	9
2.3.1 Defining the hyperbola parameters a and b	10
2.3.2 Determining the tilt angle at the base of the SUT.	11
2.4 Geometrical matching	12
2.5 Thickness function	13
2.6 Selected Geometry	13
2.7 The stiffening rings	13
2.8 Conclusions.	13
3 Loads on solar updraft tower	17
3.1 Introduction	17
3.2 Wind load.	17
3.2.1 Wind speed profile.	17
3.2.2 Wind pressure	22
3.3 Serviceability limit state.	27
3.4 Conclusions.	28
4 Finite element modeling	29
4.1 Software Choice.	29
4.2 Modeling methodology	29
4.3 Material properties	31
4.3.1 Concrete material	31
4.3.2 Reinforcement	32
4.4 Meshing.	32
4.4.1 Shear locking	32
4.4.2 Mesh refinement.	34

4.5	Structural elements	35
4.5.1	Introduction	35
4.5.2	The shell wall modeling	35
4.5.3	The stiffening rings modeling	36
4.5.4	Reinforcement	39
4.5.5	Integration schemes	39
4.6	Boundary conditions	40
4.7	Conclusions.	40
5	Linear analysis	43
5.1	Introduction	43
5.2	Model setup.	43
5.2.1	Similarities.	43
5.2.2	Differences.	44
5.3	Model Verification	44
5.3.1	Eigenvalue analysis	44
5.3.2	Linear static analysis.	45
5.4	Detailed Linear model	48
5.4.1	Eigenvalue analysis	48
5.4.2	Linear static analysis.	49
5.5	Conclusions.	51
6	Nonlinear Material Models	53
6.1	Introduction	53
6.2	Concrete model.	53
6.2.1	Concrete cracking behavior	53
6.2.2	Tension behavior.	56
6.2.3	Compressive behavior	59
6.3	Reinforcing steel	63
6.4	Conclusions.	63
7	Material nonlinear analysis	65
7.1	Introduction	65
7.2	Model setup.	65
7.3	Nonlinear analysis	67
7.3.1	Solution method.	67
7.3.2	Iteration method.	67
7.3.3	Integration scheme for nonlinear analysis	68
7.4	Result and Discussion.	69
7.4.1	Load steps-Deflection Curve.	69
7.4.2	Point A.	69
7.4.3	Point B.	72
7.4.4	Point C.	74
7.4.5	Point D.	74
7.4.6	Point E.	76
7.4.7	Reinforcement.	83
7.5	Conclusions.	84
8	Model Optimisation	87
8.1	The structural model with increasing reinforcement ratios	87
8.1.1	Model setup	87
8.1.2	Load steps-deflection curve	88
8.1.3	Influence of ultimate strain	89

8.1.4	Maximum principal strain	90
8.1.5	Deformation	90
8.1.6	Crack strain distribution	92
8.1.7	Compression.	93
8.1.8	Reinforcement	94
8.1.9	Stress-resultant	94
8.2	Recentered Model.	94
8.2.1	Load steps-displacement curve	97
8.2.2	Maximum principal strain	98
8.2.3	Deformation at the last load step.	99
8.2.4	Crack distribution at the discontinuity.	101
8.2.5	Crack distribution at the last load step	101
8.2.6	Concrete crushing and reinforcement yielding.	103
8.3	Top ring deformation	103
8.3.1	Top ring deformation of 1%NM	104
8.3.2	Top ring deformation of 2%NM	107
8.3.3	Top ring deformation of 1%RNM.	107
8.3.4	Top ring deformation 2%RNM	107
8.3.5	Conclusions	108
8.4	Conclusions.	108
9	Discussion	109
9.1	Geometry of the solar updraft tower	109
9.2	Load on the solar updraft tower	109
9.3	Finite element modeling	109
9.4	Linear analysis	110
9.5	Nonlinear Material Model.	110
9.6	Material Nonlinear Analysis.	110
9.7	Model Optimisation.	110
10	Conclusions and recommendations	113
10.1	Conclusions.	113
10.2	Recommendations	114
	Bibliography	117
A	Background information	119
A.1	Solar Updraft Tower	119
A.2	Wind-induced effects on SUT.	119
A.3	Concrete models	120
A.3.1	Concrete compressive curve	120
A.3.2	Cracking models	123
A.3.3	Concrete tensile behavior	124
A.4	Finite element software	124
A.5	Wind load on the SUT.	127
B	Reinforcement layout analysis	129
B.1	Finite element modeling	129
B.1.1	Geometry	129
B.1.2	Material model.	129
B.1.3	Concrete cover.	129
B.1.4	Element type, meshing and boundary conditions	129
B.1.5	Results and conclusions	130

C	Stiffening ring analysis	133
C.1	Structural elements for modeling the stiffening rings	133
C.1.1	Variable	133
C.2	Sub-research on the stiffening rings analysis	134
C.2.1	Introduction	135
C.2.2	Mesh.	135
C.2.3	Reinforcement setup.	135
C.3	Results and conclusions.	136
D	Nonlinear Result	139
D.1	Displacement	139
D.2	First principal strain distribution	139
D.3	Stress-resultant in the meridional direction.	139
E	2% Recentered Nonlinear Model	147
E.1	Load steps-displacement curve	147
E.2	Deformations	147
E.3	First principal strain distribution	147
E.4	Crack strain distribution	147
E.5	Stress resultant in the meridional direction	153
	List of Figures	155
	List of Tables	161

Acronyms

SUT	Solar Updraft Tower
RC	Reinforced Concrete
FEM	Finite Element Method
SLM	Simple Linear Model
DLM	Detailed Linear Model
BNM	Beam Nonlinear Model
STNM	Shell no Transverse Nonlinear Model
SNM	Shell Nonlinear Model
1%NM	1% Nonlinear Model
2%NM	2% Nonlinear Model
3%NM	3% Nonlinear Model
1%RNM	1% Re-centered Nonlinear Model
2% RNM	2% Re-centered Nonlinear Model
BRM	Beam Ring Model
SRM	Shell Ring Model



Introduction

High quantity of energy consumption worldwide drives the needs of renewable and sustainable energy for the sake of sustainable development of economics. On the other hand, some developing countries in Africa have been facing the electricity shortage for decades due to the lack of raw material and water source. In 1903, the Spanish engineer I. Cavanyes proposed the concept of the solar updraft power generation technology that generates a reasonable amount of electricity under a sunny but energy-brutal environment. The wind and solar are the two renewable energy applied to this technology which give zero carbon footprint during operation. Since 1981, a team including German civil engineer J. Schlaich designed and built a prototype of SUT in Manzanares in Spain (Bourget (2013)), with 200m high and a maximum power output of 50kW. More investigation and research have been done in recent years to improve this new generation of renewable power technology.

Figure 1.1 provides insight into how the solar updraft tower(SUT) operates. As shown in the figure, the solar updraft plant consists of three components: the solar air collector, the tower, and the wind turbine. Its working principle explained in the following.

- Air collector consists of a glass or plastic roof that horizontally several meters above the ground for the greenhouse effect. The air beneath the transparent roof is heated up under the solar radiation and the re-radiation from the Earth.
- The solar updraft tower locates at the center of air collector with a large air inlet connects to the air collector.
- The pressure differences between heated air and atmosphere generate the driving force to let solar updraft tower updraft heated air move to the top atmosphere of the tower. In a large SUT with temperature rise by about 30K to 35K, the updraft velocity in the tower is about 15m/s (Bergermann (2011)). At the mean time, a suction force in tower drives cold air around the frontier of the air collector move into the air collector.
- Wind turbines are installed at the base of the tower. The turbine is a shrouded pressure-staged wind turbo generator. The power output is determined by the product of the volume flow per unit time and the pressure differences over the turbine. So, the air velocity stays the same before and after the turbine. Depending on the design scheme, it can be one large wind turbine or many small turbines.

1.1. Possible threats to reinforced concrete solar updraft tower

Solar updraft towers can be both constructed of steel or reinforced concrete. Lately, there have been many investigations about constructing a SUT of steel. But some decisive shortcomings of a steel SUT

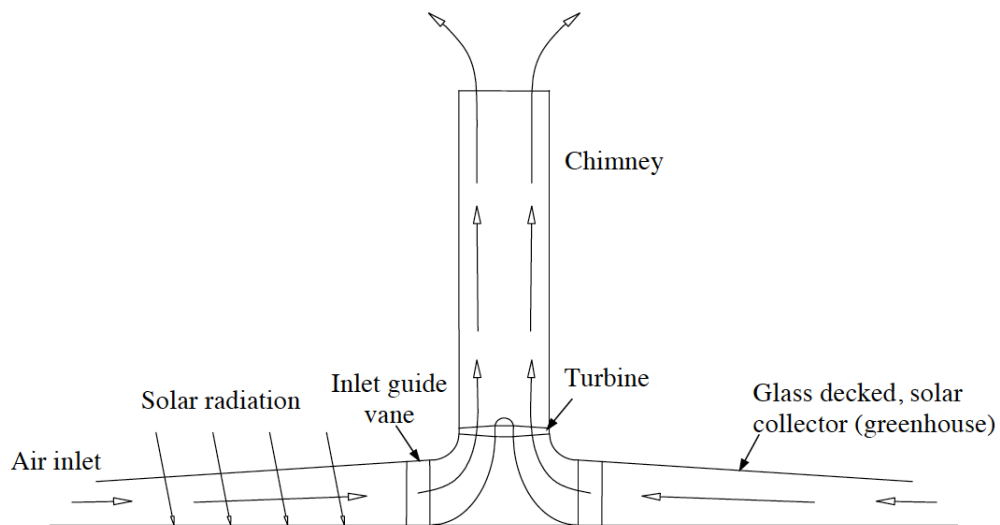


Figure 1.1: The solar updraft tower power plant schematic (Gannon (2002)).

do hinder its construction possibilities. Firstly, steel structures are too light to resist wind load and much more prone to the dynamic resonance. Secondly, slender steel structures with thin wall thickness can lead to the global buckling, the shell buckling, and the local buckling easily. Furthermore, the air-tightness cannot be ensured in the long term. The high cost of connection and maintenance and inspection are also the drawbacks compared to concrete. Additionally, cracks caused by fatigue under cyclic wind load leads to a much lower structural resistance. On the contrary, reinforced concrete is durable and has achievable performance both on the stability and the dynamic resistance. Around all proposed locations for constructing the SUT, the reinforced concrete (RC) material regards as the most economic choice (Lohaus and Abebe (2010)). Even for a SUT constructed by using the high-performance reinforced concrete, due to its extra height and extra thin thickness, some structural challenges need to be considered.

- The combination of selfweight and static wind load acting on the concrete shell may cause extensive cracking at windward side.
- The natural vibration frequency of solar updraft tower is rather low, which is close to the frequency of gust wind fluctuation. Along-wind oscillation is vulnerable to occur.
- Stress and thermal fatigue problem for concrete material.
- Durability of concrete material during the end of service life around the 80-120 years.
- Buckling and instability problems of the thin shell structure.
- Shrinkage causes residual stress in the freshly reinforced concrete shell.
- Construction load.
- Cross-wind loading caused by vortex shedding on the leeward side.
- Seismic load by earthquakes.

Among all these problems, some loads should be addressed here. The large self-weight is treated as a favorable load that compensates part of the tension force on the windward side. Wind load and temperature load are the unfavorable loads for SUT. Temperature differences may cause cracks on the

shell wall due to structural fixation. The static wind load gives the large tensile force on the windward side and deforms the top cross-section of the tower. Dynamic wind action is another serious hazards for SUT because the first natural frequency is very close to the peak of the wind power spectrum.

1.2. Problem analysis

The SUT is costly due to its structural size, and until now the SUT has not been built yet. The stiffening rings require an enormous amount of construction effort which leads to an even higher cost. The solar updraft tower would be the largest shell structure if it were ever built. A research project from Eck et al. (2015) did a structural optimization of RC solar updraft tower under dynamic wind actions. Continuing with the structural improvement, an accurate model to simulate the structure is needed including material nonlinearity. The cracking of concrete is expected to redistribute the strain over the cross-section, which mainly activates the reinforcement and eventually saves a substantial amount of reinforcement (Harte et al. (2013)). By understanding the nonlinear structural response, a less conservative structural design can be achieved by strengthening or modifying the structure only at the critical area.

1.3. Research question

1.3.1. Main research questions

What is the problem areas of the solar updraft tower by performing the physical nonlinear analysis under static wind action? How the model can be improved to achieve a feasible structural behavior at the serviceability limit state?

1.3.2. Sub research questions

There are some sub research questions in order to achieve answering the main research question. The answers to these sub-research questions can be found in chapters that are denoted in parentheses.

- How to built a finite element model for material nonlinear analysis to get a reasonable results (Chapter 4, 5).
- What are these proper nonlinear material models that can provide a reasonable structure response of the SUT (Chapter 6).
- What is the suitable element type for modeling the stiffening rings (Chapter 7).
- What is the nonlinear structural behavior of the SUT with a minimum reinforcement ratio modeled at the shell walls and 1% reinforcement ratio modeled at the stiffening rings (Chapter 7)
- What is the influence of the tension stiffening effect on the overall structural behavior (Chapter 8).
- How does the eccentricity of the stiffening rings affect the structural bearing capacity (Chapter 8).

1.4. Research Methodology

1. Review state-of-art related to the structural behavior of SUT under self-weight and wind action. Review nonlinear material models for the concrete and the reinforcing bar.
2. Calculate the geometry of solar and wind load profile over the whole structure.
3. Perform linear analysis both for structural verification and then build a more detailed model for the nonlinear analysis.

4. To determine the nonlinear material models for both concrete, the reinforcing bar and their bonding behavior.
5. To perform a material nonlinear analysis with to find the realistic structural response under self-weight and static wind action.
6. To perform material nonlinear structural optimization to find the recommended structural design.
7. Gives conclusions and recommendations of further research.

1.5. The scope of the research

For the sake of keeping the power performance of the SUT, the geometry was determined according to the original design of Krätzig & Partner. The analysis related to the turbine and the air collector is out of the research scope. The openings at the base of the tower will not be modeled and no substructure is considered. According to the analysis of foundation stiffness from the original research project of Eck et al. (2015), the boundary conditions at the base of the tower would be fixed constraint. Reinforcement will be added both in the shell wall and the stiffening rings. The pre-stressed load might be a design choice while it will not be considered in this research project.

This research project focuses on the structural behavior under static self-weight and wind load. The solar updraft tower will be built in reinforced concrete. Physical non-linearities are included without considering time-dependent behavior. The load at construction phase is not counted. It was concluded that compared to static and dynamic wind load, the temperature differences has no significant impact on structure response (Dyk (2008)), which is not considered in this research project. Furthermore, it is expected that a non-seismic region is chosen for constructing SUT. No fatigue load is considered because a high-performance concrete can compensate this effect. It was assumed that the SUT is built on an uninformed soil environment without neighboring structure then the settlement will also be ignored.

1.6. Expectations

The nonlinear structural response is expected to be different from the linear response so as to the problem area of the structure. Failure mechanisms and the stress redistribution might occur in the nonlinear analysis. From the original research project of Eck et al. (2015), it was known that the stiffening rings play a significant role in the structural response of SUT. More attention to stiffening rings will be given in this research project.

1.7. Thesis layout

This thesis is organized as follows. Chapter 1 presents the background and motivation of this research project and its possible structural challenges.

Chapter 2 Geometry of Solar Updraft Tower

In Chapter 2, the calculation procedure of the geometry of solar updraft tower is performed. The calculation includes the upper cone, the hyperbolic and their geometrical matching. The discussion for choosing a certain geometry parameter is given. Thickness function over tower height and technical design drawing of stiffening ring are presented at the end of this chapter.

Chapter 3 Loads on Solar updraft tower

Chapter 3 presents the loading conditions acting on SUT. The self-weight and static wind load will be defined. This chapter gives the calculation method of the wind profile, the maximum wind speed, the pressure coefficient.

Chapter 4 Finite element modeling In this chapter, the methodology of finite element modeling of solar updraft tower is presented. This chapter also gives the meshing refinement, the definition of

material properties, boundary conditions. The element types choices and their comparisons for modeling stiffening ring are discussed. By doing so, a cross-section analysis of stiffening ring is performed.

Chapter 5 Linear Analysis

The result related to the linear analysis of different models is shown in this chapter. First, a model was set for verification of the model setup. Then the models with different stiffening ring geometry are compared. One model is chosen to continue the physical nonlinear analysis.

Chapter 6 Material nonlinear Model

Before the nonlinear analysis, selecting the proper nonlinear material models should be done. In this chapter, a concrete model will be explained including the input and their background theory. They are cracking model, tensile behavior, compressive behavior, lateral cracking and lateral confinement. For reinforcement, a von Mises Plasticity theory and stress and strain relation are introduced.

Chapter 7 Physical nonlinear analysis

This chapter will start with the load step-displacement curve between three different models. From the discontinuities of the curve, a structural analysis is performed. The structural behavior at certain load level is shown. At the mean time, a comparison between the model modeled by beam element and curved shell element on the rings is given. All physical nonlinear result gives a clue about structural optimization.

Chapter 8 Nonlinear structural optimization

Given the nonlinear structural behavior of SUT, some solutions are given to improve structural behavior. The reinforcement ratio will be increased and their result will be compared. Models with recentered ring geometry will be built to improve the structure behavior.

Chapter 9 Discussion

This chapter gives the brief discussion and conclusion on each chapter.

Chapter 10 Conclusions and Recommendations

The conclusion is driven in this chapter, so as some recommendations for the future research.

2

Geometry of Solar Updraft Tower

This chapter starts with the geometry component of the solar updraft tower. The upper cone geometry and lower hyperbola are mathematically derived. Next, the matching condition is determined to result in a smooth connection between two geometries. The mathematical and geometrical limitations determined the base tilt angle. The thickness function and drawing details of stiffening ring are also mentioned in this chapter.

2.1. Introduction

The development of framework technology of large reinforced concrete (RC) shell wall in constructing cooling tower gives the possibility of construction SUT by RC shell wall with varying wall diameter and thickness. The geometry of SUT is highly related to the power output, and its power efficiency increases with the increasing height of tower and diameter of the collector. Only extra-high solar updraft tower ranging from 750 to 1500 meter high can reach a sufficient power output efficiency. The tower of 1000 meter is a challenge, while it is possible to be built. Additionally, for the sake of keeping consistency with original research of Eck et al. (2015), a tower height of 1000 meter will be used for this research. In this chapter, the calculation method of SUT geometry will be detailed reported. Two geometries will be considered, one is the original design from Krätzig & Partner, and the other is structurally optimized model according to the research of Eck et al. (2015).

For the sake of stabilizing the air flow velocity, the upper part of the tower is assumed to be an expanded cylinder with the cross-sectional area increased about 13% to 14% from the base to the upper end. The lower part of the tower will be a hyperboloid of revolution. It is formed by rotating a hyperbolic profile around a central axis over 360 degrees. The junction between the upper cone and lower hyperboloid should be smooth and has one slope. With default values including the height of the tower, the throat height, the base diameter, throat diameter and the tilt angle, the geometry of solar updraft tower can be defined by geometrical and mathematical equations and limitations. In this chapter, the wall thickness profile over height is also present. It was implemented into finite element method by inserting thickness function in the direction of height.

2.2. Upper cone

The upper part of SUT is an inverted truncated cone. To keep the flow velocity constant, the cross-sectional area must be increased to the top end with around 13% to 14%. The increment is assumed an inverted truncated cone from the base of the SUT to the top end. A virtual base diameter is assumed. Figure 2.1 shows the cone geometry with virtual base diameter. By following this requirement, the following equalities can be got

$$A_{top} = 1.14A_{bas} \quad (2.1)$$

$$\pi r_{top}^2 = 1.14\pi r_{bas}^2 \quad (2.2)$$

$$r_{top} = \sqrt{1.14}r_{bas} \quad (2.3)$$

where

- A_{top} area of circle at top of cone
- A_{bas} area of circle if cone formula extend to the base
- r_{top} radius of circle located at top of cone
- r_{bas} radius of circle located if cone formula extended to the base.

The upper part cone needs to connect to lower hyperboloid, and the slop of two geometries at connection point needs to keep consistent. Now it gives the slope function of the cone:

$$r'(h) = \frac{r_{top} - r_{bas}}{H} \quad (2.4)$$

Where

- $r'(h)$ slop of the cone
- H height of tower=1000m

The linear increment of the diameter gives the function of cone diameter. The inverted truncated cone can be got by sweep the linear function along the center axis.

$$r(h) = r_{bas} + \frac{r_{top} - r_{bas}}{H} h \quad (2.5)$$

where

- $r(h)$ radius of tower with varying height

For a solar updraft tower, the throat diameter and throat height are predefined as known variables. Once the throat diameter and throat height are known, from Equations 2.1 and 2.6, the radius at the top end of the tower can be determined.

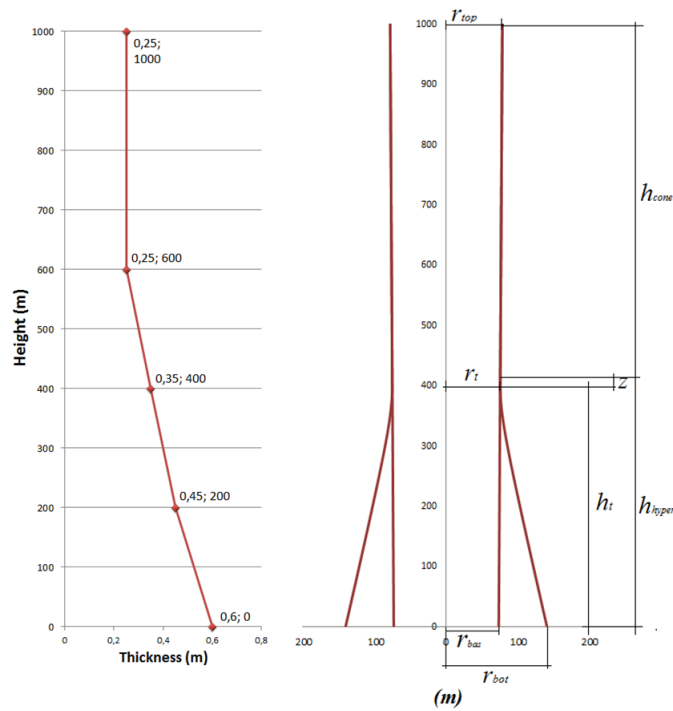


Figure 2.1: Parameter indication on the geometry and the shell wall thickness over height.

$$r_{bas} = \frac{r_t}{1 + \frac{\sqrt{1.14}-1}{H} h_t} \quad (2.6)$$

where

h_t throat height

2.3. Lower Hyperboloid

The hyperbolic structure has a negative Gaussian curvature, meaning the curve is inward. Stability of hyperbolic structure is superior compared to the cone and the straight structure. Firstly, the hyperbola profile equation will be determined, and then the hyperbola parameters will be defined. The geometry can be created eventually. The hyperboloid at the lower part of the tower is formed by rotating the defined hyperbola about its central axis for 360° . A hyperbola with transverse axis is aligned with the x-axis of a Cartesian coordinate system, the equation of the hyperbola is written as

$$\frac{x^2}{a^2} - \frac{y^2}{b^2} = 1 \quad (2.7)$$

$$x(z) = \frac{a}{b} \sqrt{b^2 + y^2} \quad (2.8)$$

For tower geometry, the x coordinate refers to the radius of tower and y coordinate refers to the height of the tower.

$$r(z) = \frac{a}{b} \sqrt{b^2 + z^2} \quad (2.9)$$

For the geometry model, the curve is shifted from the central axis to a certain distance a . It should be noted that, in the coordinate system of hyperbola, $z = 0$ is the location of the throat of the solar tower. The expression of radius at lower hyperboloid is written as

$$r(z) = \Delta r + \frac{a}{b} \sqrt{b^2 + z^2} \quad (2.10)$$

After taking the derivative of z in Equation 2.9, the slope of hyperbola can be found

$$r'(z) = \frac{a}{b} \frac{z}{\sqrt{b^2 + z^2}} \quad (2.11)$$

2.3.1. Defining the hyperbola parameters a and b

In the expression of hyperbola, two important parameters a and b should be determined. These parameters are determined by default values. The the radius of tower at throat height is summation of offset and a parameter.

$$r_t = r(z = 0) = \Delta r + \frac{a}{b} \sqrt{b^2 + 0^2} = \Delta r + a \quad (2.12)$$

where

r_t radius of tower at throat height

The expression of the radius at the base of the tower shows below and the parameter a can be found be expressed by default values including bottom radius, throat radius, throat height and unknown parameter b .

$$r_{bot} = r(z = -h_t) = \Delta r + \frac{a}{b} \sqrt{b^2 + h_t^2} \Leftrightarrow a = \frac{r_{bot} - r_t}{\frac{1}{b} \sqrt{b^2 - h_t^2} - 1} \quad (2.13)$$

where

r_{bot} radius at bottom of tower

Using Equation 2.13 and Equation 2.10, the tilt angle at the base of tower can be expressed in the following equations

$$r'_{bot} = \tan(\varphi_{bot}) = \frac{r_{bot} - r_t}{\sqrt{b^2 + h_t^2} - b} \frac{h_t}{\sqrt{b^2 + h_t^2}} \quad (2.14)$$

where

φ_{bot} tilt angle at the bottom of the tower.

From Equation 2.14, the parameter b can be expressed by default bottom radius, throat radius, and throat height and unknown base tilt angle.

$$b = \sqrt{\frac{h_t r'_{bot}}{2(r_{bot} - r_t) - h_t r'_{bot}} \left(\frac{r_{bot} r_t}{r'_{bot}} - h_t \right)} \quad (2.15)$$

2.3.2. Determining the tilt angle at the base of the SUT

Theoretically, infinite variations of a hyperbola exist. But they can be only achieved under a certain geometrical and mathematical limitation. These borders give the limitation of tilt angle. The bottom radius has to be larger than throat radius.

$$r_{bot} > r_t \quad (2.16)$$

The bottom tilt angle has to be bigger than the slope of the line connect from bottom to throat. Figure 2.2 shows minimum tilt angle.

$$\tan(\varphi_{minimum}) > \frac{r_{bot} - r_t}{h_t} \quad (2.17)$$

The tilt angle also has its upper limit according to the expression of the parameter b . The expression $2(r_{bot} - r_t) - h_t u'_{bot}$ has to be positive.

$$2(r_{bot} - r_t) - h_t u'_{bot} > 0 \quad (2.18)$$

$$u'_{bot} < 2 \frac{r_{bot} - r_t}{h_t} \quad (2.19)$$

The tilt angle can subsequently be expressed into the following inequality.

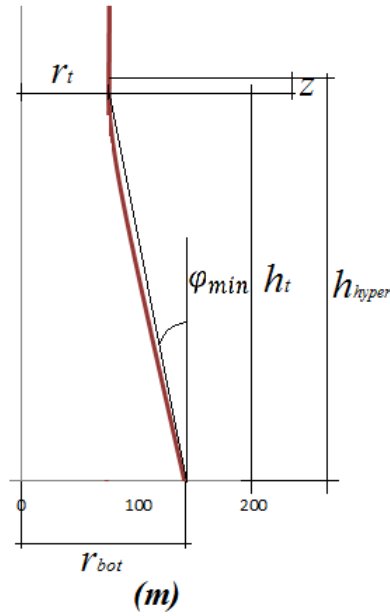


Figure 2.2: Minimum tilt angle of hyperbola at the base.

$$\arctan\left(\frac{r_{bot} - r_t}{h_t}\right) > \varphi_{bot} > \arctan\left(2\frac{r_{bot} - r_t}{h_t}\right) \quad (2.20)$$

In this research project, the middle value of this range will be chosen.

2.4. Geometrical matching

The principal for matching between cone and paraboloid is that the connection point has only one slope in order to decrease the geometrical discontinuity. Assume the height of hyperboloid is H_{hyper} .

$$r'_{H_{hyper}} = r'_{con} \quad (2.21)$$

where

$$\begin{aligned} r'_{con} & \text{ slop of the cone} \\ r'_{H_{hyper}} & \text{ slop of hyperboloid at matching height} \end{aligned}$$

$$\frac{a}{b} \frac{z}{\sqrt{b^2 + z^2}} = r'_{con} \quad (2.22)$$

The location of matching point can be expressed in the following

$$z = \pm \sqrt{\frac{b^4 r_{con}^2}{a^2 - b^2 r_{con}^2}} \quad (2.23)$$

Table 2.1: Geometry details of the design model of Krätzig & Partner

	Model of Krätzig & Partner
Tower Height (m)	1000.00
Throat Height (m)	400.00
Transition Height (m)	401.81
Bottom Radius (m)	140.00
Throat Radius (m)	75.00
Top Radius (m)	77.97
Tilt Angle (degree)	14°

The height of lower hyperboloid would be sum of throat height and the distance from throat and matching point.

$$H_{hyper} = h_t + \sqrt{\frac{b^4 r_{con}^2}{a^2 - b^2 r_{con}^2}} \quad (2.24)$$

2.5. Thickness function

To save concrete material, a major design principle is to construct the tower shell wall as thin as possible. The wall thickness varies with height. The top 400m has a constant wall thickness of 0.25m, and then gradually increases to 0.6m to the base. Figure 2.1 shows the wall thickness detail that will be modeled in the research project.

2.6. Selected Geometry

The original design according to Krätzig & Partner has a throat radius of 75m and throat height of 400m. This design is widely accepted in both structural engineering and other related scientific field. The contraction and diffuser shape of the chimney can affect the amount of flow and pressure drop over the turbine. Except for chimney geometry, the wall thickness and obstruction in the chimney also play a role in pressure drop over the turbine. The design of Krätzig & Partner will be used in this research project. Table 2.1 and Figure 2.3 give the geometrical details and the 3D images of the models.

2.7. The stiffening rings

The configuration of stiffening rings shown in Figure 2.4. Stiffening rings divide the shell tower into segments, which will increase effectively the natural frequencies (Arndt et al. (2011)). More importantly for the use of stiffening rings is that it can reduce the tensile force by increasing the internal level arm. The throat height is vulnerable to the concrete tensile crack because the self-weight of the tower is not able to counterbalance wind action Eck et al. (2015). The increasing number of stiffening rings leads to a more cosine shape stress distribution in the circumferential direction, which means a linear distribution over the diameter of the cross section.

One top stiffening ring is constructed at the top end of the tower. The nine intermediate stiffening rings are located evenly on the tower with the spacing of 100m. All rings are located in the shell wall in a certain eccentricity, which means the mass center line of stiffening ring is outside the mid-surface of the shell wall. Reinforcements will be embedded in the stiffening rings.

2.8. Conclusions

In this chapter, the approach of defining SUT geometry has been explained. It mainly consists of defining upper cone and lower hyperbola and their geometrical matching. For a given throat height,

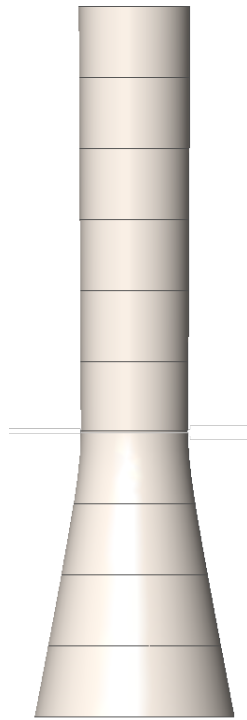


Figure 2.3: Geometry of design model of Krätzig & Partner

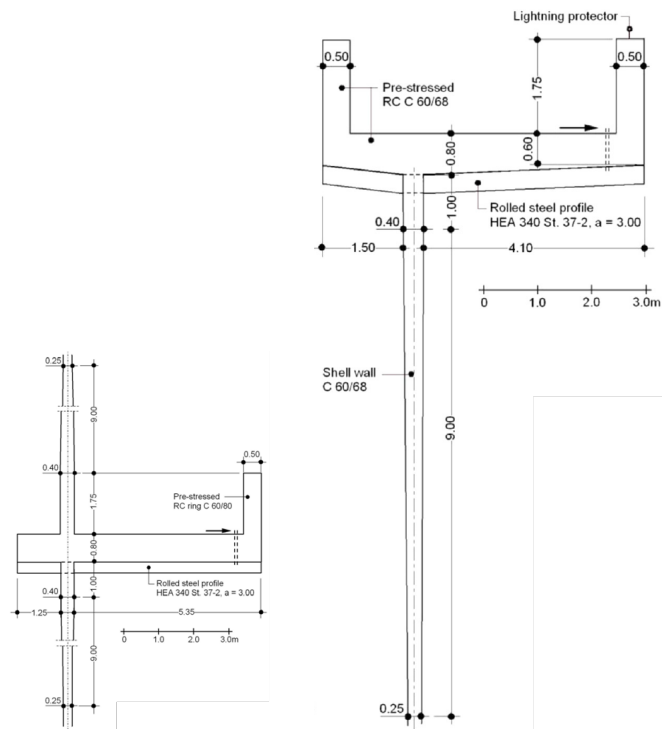


Figure 2.4: Drawing of the top and intermediate stiffening rings by Krätzig & Partner, Germany (Lupi et al., 2015) (Niemann et al., 2009)

throat diameter and base diameter, the geometry of an SUT can be defined. Two geometries are mentioned in this chapter for modeling nonlinear analysis. The original geometry design from Krätzig & Partner is chosen for this research project. The tower has a height of 1000 meters with a throat radius of 75 meters at height of 400 meters. It has a base radius of 140 meters and tilts angle of 14° . For the sake of increasing stiffness and stability of SUT, the top and intermediate stiffening rings geometry are defined. The stiffening rings are located over the whole height of solar updraft tower every 100m.

3

Loads on solar updraft tower

This chapter starts with a background introduction of wind characteristics. Given the modeling purpose, the need for select a proper wind load profile is apparent. The derivation of the wind load pressure vertical direction and the wind coefficient over circumferential direction are discussed in details.

3.1. Introduction

A variety of loads is acting on the solar updraft tower. The problematic loads are dead load, wind load, earthquake load, temperature variations, construction load and settlement. In this research, the wind load and self-weight load are taken into account. The wind load is recognized as an unfavorable load which plays the most critical role in design the solar updraft tower. The amount of reinforcement in the shell wall and stiffening ring are determined by the net difference between tension caused by wind load and compression caused by the dead load.

For the ultra-high structure (1000m) with varying diameter from 140m to 280m, the determination of wind pressure can be challenging. The particular engineering structures, such as cooling towers, are often designed by special regulations or guidelines. The regulations are based on years of experience in engineering design and construction. However, no specific design code is made for design the solar updraft tower, and it is, therefore, would be reasonable to calculate the loading conditions based on current existing design code. The effects of different loading conditions can result in the wind by factoring and combining according to the code. The existing German cooling tower code VGB-R-610E2010 (2010) gives both ultimate limit state and serviceability limit state design for the large cooling tower. In this chapter, the calculation of the wind speed profile, the maximum wind speed profile, the wind pressure and the pressure coefficient will be explained.

3.2. Wind load

For the calculation of wind load, the free stream means wind speed profile over 1000 meter high should first be defined. For taking into account, the fluctuation of wind speed by gust wind, a conversion from the mean wind speed profile to the maximum wind speed profile should be done. Subsequently, the free stream wind pressure profile can be generated by defining the air density function over height. Lastly, the circumferential direction wind load coefficient is derived according to the code VGB-R-610E2010 (2010) for natural draft cooling towers.

3.2.1. Wind speed profile

The definition of wind is air flowing from the high pressure to low pressure. The wind speed and direction can be highly variable over time and space. In space, it can be described on a large scale

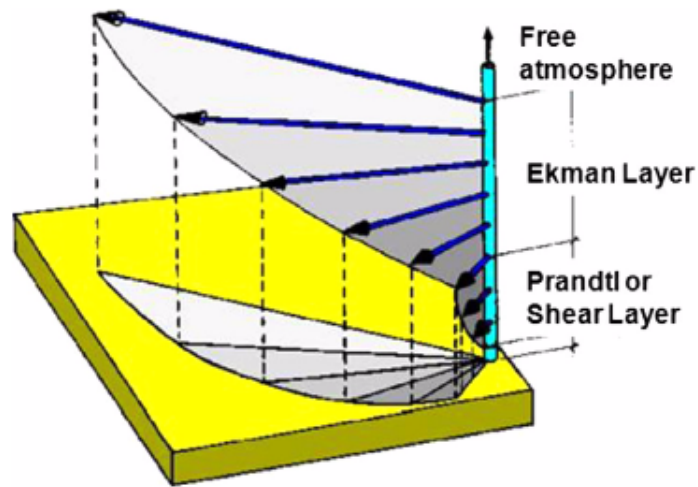


Figure 3.1: The Ekman spiral (Lupi et al. (2015))

such as climatic region, while it can be localized into obstacles such as trees and buildings. It can also be measured according to the different time scale. In the time, it can be a seasonal variation or it can also be the second variation.

When wind passing over Earth's surface, swirling of air and the reverse current called eddies are generated if the Earth's surface is not smooth. The characteristics of eddies highly depend on the roughness of Earth's surface. In wind perspective, an atmosphere can be divided into several layers. Prandtl layer is the layer that extends from ground level to a height of around 300m (Lupi et al. (2015)). It consists of eddies with different size and moving and rotating along the ground surface. The ground surface roughness and turbulence play a significant role in wind speed. The mean wind speed increases with the increase of height while the turbulence tends to decrease with height. The solar updraft tower with a height of 1000m crosses Prandtl layer and steps into Ekman layer. In Ekman layer, the shear, and turbulence decrease, the Coriolis force plays a role in changing wind direction. For a wind profile of a structure up to 1000m high, both Earth's surface roughness and Coriolis effect should be considered. Harris and Deaves (ISO4353 (2012)) derived a wind profile both for Prandtl and Ekman layer which including both effects. This is based on the traditional logarithmic law with additional consideration of Coriolis effect.

The mean wind speed profile averaged over one hour over flat open country terrain can be produced. Zimbabwe, where the latitude falls between 15° and 22° specifies a design wind speed of 35m/s with 50-years return period 3-s gust (Holmes (2007)). This wind speed was analyzed at five different locations by Lewis(1983). Zimbabwe is chosen for the construction location in this research project for keeping the consistency of wind load profile from the original research project of Eck et al. (2015). The expected dominant windstorm would be thunderstorm winds created by local convection (Holmes (2007)). The Harris and Deaves wind profiles over flat terrain for synoptic storm:

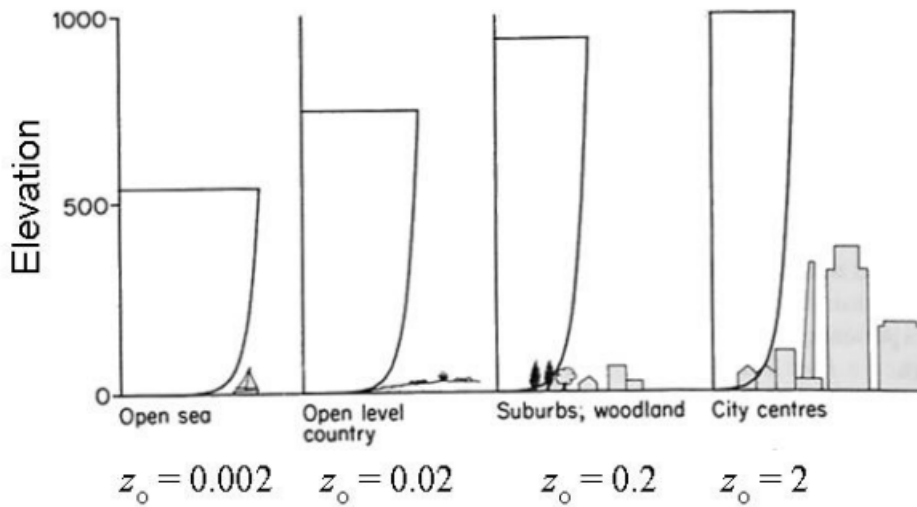


Figure 3.2: The mean wind profiles for different terrains (P. Mendis and Cheung (2007)).

$$V_{tr,z,T=3600s} = \frac{u_*}{0.4} \left\{ \ln\left(\frac{z}{z_0}\right) + 5.75\left(\frac{z}{z_G}\right) - 1.88\left(\frac{z}{z_G}\right)^2 - 1.33\left(\frac{z}{z_G}\right)^3 + 0.25\left(\frac{z}{z_G}\right)^4 \right\} \quad (3.1)$$

where

- z the height above ground level
- z_G the atmospheric boundary layer thickness

$$z_G = \frac{u_*}{6f} \quad (3.2)$$

The thickness of the boundary layer highly depends on the type of terrain. The higher the roughness of Earth's surfaces the larger the boundary layer thickness. Figure 3.2 shows the mean wind profiles for different terrains.

Logarithmic law fits right to wind speed distribution near the surface, for a given reference wind speed at the reference height of 10 meters. The function of logarithmic law can be used for calculation of friction velocity. The log law is shown below (Scanlan and Simiu (1996)).

$$U(z) = \frac{1}{k} u_* \ln\left(\frac{z}{z_0}\right) \quad (3.3)$$

$$V_{ref} = \frac{1}{k} u_* \ln\left(\frac{10}{z_0}\right) \quad (3.4)$$

Then the expression for friction velocity can be found.

$$u^* = \sqrt{V_{ref}^2 \kappa} \quad (3.5)$$

κ is the corresponding values of the surface drag coefficient defined as

$$\kappa = \left[\frac{k}{\ln\left(\frac{10}{z_0}\right)} \right]^2 \quad (3.6)$$

where

- V_{ref} reference wind speed
- u^* friction velocity
- z_0 surface roughness with a variety of terrain roughness given Figure 3.3
- k well-known Von Kármán constant is assumed to be $k = 0.4$

To take the Coriolis effect into account, f factor is applied.

$$f = 2\Omega \sin\phi \quad (3.7)$$

where

- ϕ latitude which is 15° for selected location
- Ω angular velocity of the Earth rotation ($= 72.9 \times 10^{-6}$)

ISO04353 (2012) gives the analysis procedures for conversion wind speeds with different averaging time. The calculations depend on an averaging time factor and a peak factor and terrain roughness.

$$V_T = k_T V_{T=3600s} \quad (3.8)$$

ISO04353 (2012) provided the average peak factors and reference averaging time factors along different averaging time at reference condition of $z = 10m$ and $z_0 = 0.03$. It shows on Table 3.1.

The conversion needed for this research project is to converse 3s gust wind speed to hourly mean wind speed. According to Table 3.1, for 3s gust wind speed, the average peak factor is 3, and reference averaging time factor is 1.53.

Table 3.1: Averaging peak factors and evaluation of reference averaging time factor (ISO04353 (2012)).

Averaging time T(s)	Average peak factor g_v	Reference averaging time k_T $z=10m, z_0 = 0.03$
1	3.90	1.62
3	3.00	1.53
10	2.40	1.42
30	1.65	1.27
100	0.90	1.15
600	0.28	1.05
3600	0	1.00

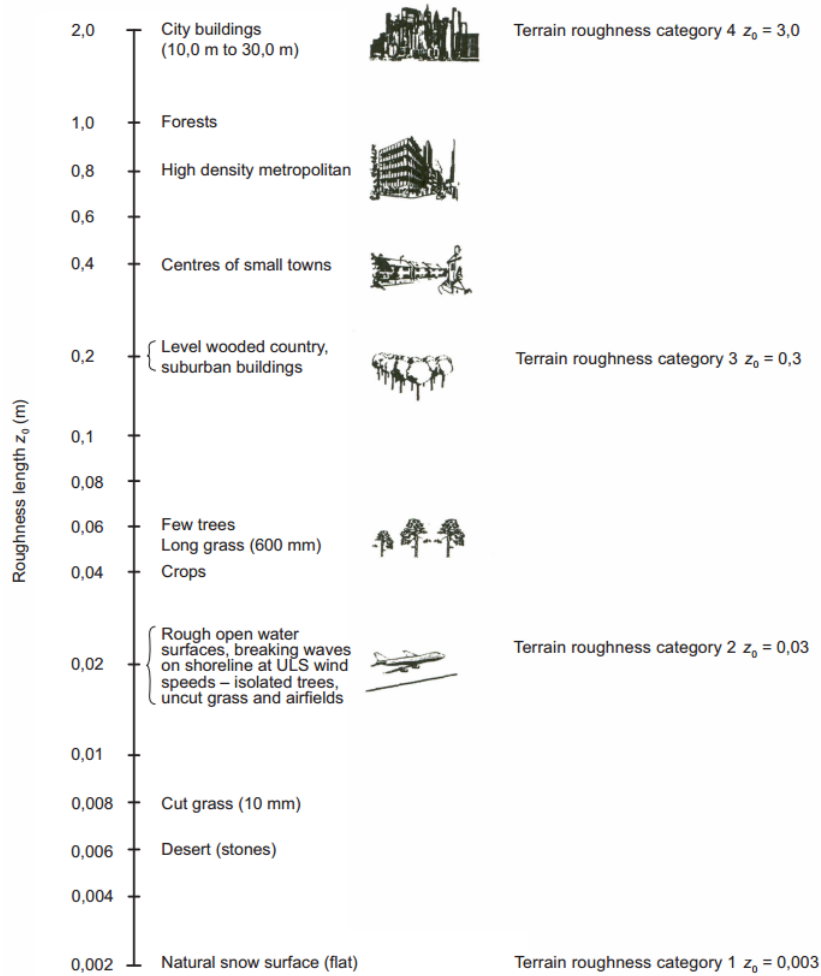


Figure 3.3: Description of terrain roughness lengths, z_0 (ISO04353 (2012)).

Table 3.2: Correction factor for other return period (ASCE7 (2013)).

Return period (year)	Correction factor
500	1.23
200	1.14
100	1.07
50	1.00
25	0.93
10	0.84
5	0.78

$$V_{T=3s} = 1.53V_{T=3600s} \quad (3.9)$$

The design service life for the solar updraft tower is over 100 years, the correction factor for wind speed should be applied to determine the wind load. The ASCE7 (2013) gives the correction factor from year 5 to 500 years (Table 3.2). For SUT with a service life of 100 year, the correction factor is 1.07.

$$V_{T=3600,10m} = 35m/s \times \frac{1}{1.53} \times 1.07 = 24.5m/s \quad (3.10)$$

3.2.2. Wind pressure

Wind pressure distribution on a structural surface is determined by the wind speed and the shape and surface roughness of the structure. The total wind pressure consists of the mean wind pressure and pressure fluctuations produced by gusts and separation-induced turbulence. A sufficient accuracy for the structural design can be achieved if both effects are considered (Niemann and Höffer (2009)). For the wind pressure load acting on solar updraft tower, a maximum pressure expected gust velocity pressure should be adapted. The wind pressure on concrete shell surface is formulated as follows,

$$q_{z,\theta} = [C_{pe,\theta} - C_{pi}] \times q_{max,z} \quad (3.11)$$

where

- $q_{max,z}$ maximum pressure calculated from gust velocity
- $C_{pe,\theta}$ external pressure coefficient
- C_{pi} internal pressure coefficient

Maximum free stream wind load pressure

The expression of maximum free stream wind pressure is the following,

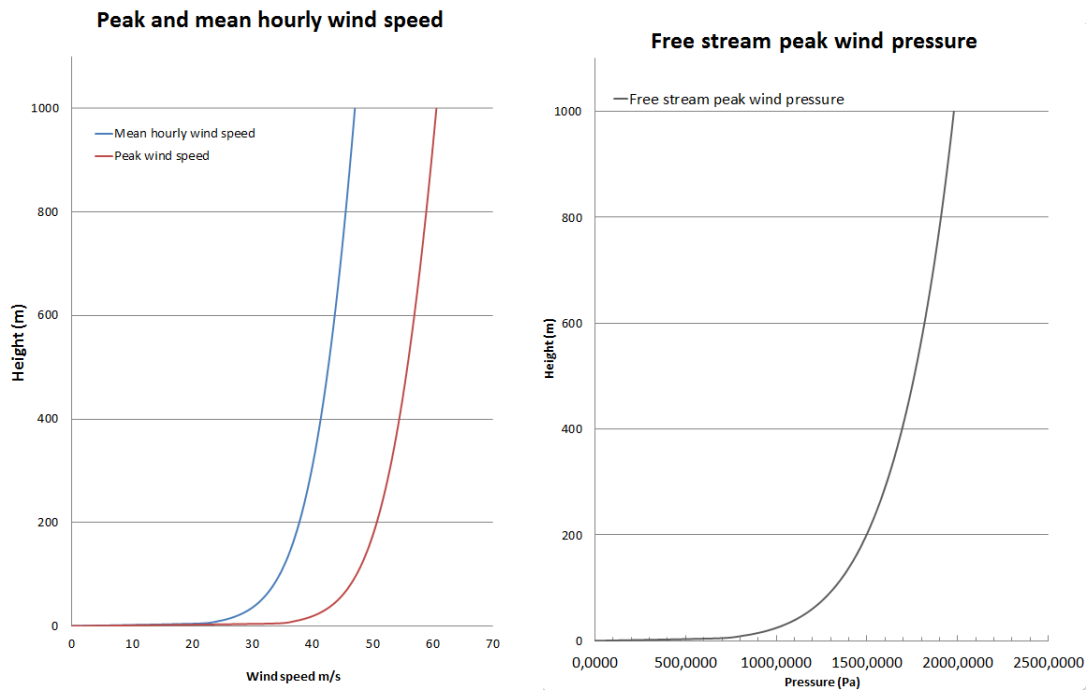


Figure 3.4: Free stream wind velocity[m/s](left); free stream wind pressure[Pa](right).

$$q_{max,z} = \frac{1}{2} \rho_z V_{z,p}^2 \quad (3.12)$$

where

- ρ air density at a relative height
- $V_{z,p}$ peak wind velocity at relevant height

The instantaneous peak wind velocity can be calculated from mean wind velocity by taking the peak factor and turbulence intensity account. The expression shows to the following equation.

$$V_{z,p} = V_{z,m} \times (1 + g_v I_v) \quad (3.13)$$

where

- g_v average peak factor (3) refer to Table 3.1
- I_v turbulence intensity = $\frac{1}{\ln \frac{z}{z_0}}$

The averaged peak factors depend on the extent of the area that can influence the load. The gust factor is three due to the larger impact areas and quasi-static behavior (Niemann and Höffer (2009)).

Air density

It is common that the variability of air density is neglectable with structure height. For an ultra high structure like SUT, the air density should be taken as a variable over height. Due to temperature and

pressure differences, the air density decreases with increasing height. A 10% reduction of air density leads to a 10% decrease of wind force. The calculation is the following.

The expression for air density

$$\rho = \frac{pM}{RT} \quad (3.14)$$

$$p = p_0 \left[1 + \frac{L \times h}{T_0} \right]^{-\frac{gM}{R}} \quad (3.15)$$

$$T = T_0 + Lh \quad (3.16)$$

where

M	molecular weight of dry air= 0.0289644kg/mol
p	the atmospheric pressure in relevant height
R	the universal gas constant = 8.31447J/(molK)
T	the temperature at relevant height
h	the height above the sea level. For the chosen location, the altitude is 300m
p_0	the sea level standard atmospheric pressure
T_0	the sea level standard temperature= 288.15K
L	the temperature lapse rate=-0.0065K/m
g	the gravitational acceleration

In Figure 3.4, on the left side it gives the free stream hourly mean velocity and peak wind velocity increase with height, and on the right-hand side, it provides the free stream wind pressure increase with height.

Pressure coefficient

The shell is sensitive to membrane tension in meridional direction. The external wind load and internal operation flow effect should be both taken into account. For internal condition, guideline VGB-R-610E2010 (2010) suggests an axisymmetric internal suction coefficient with the magnitude of 0.5 as a common practice. The external pressure coefficient distribution over the circumferential direction of the cylindrical cross section was defined in VGB-R-610E,2010. For external wind pressure coefficient, VGB Guideline divides the coefficient distribution into three parts. The section I is the windward side with angle θ from $0^\circ - 30^\circ$. Section II is the side suction ranging from around 30° to 100° and the maximum suction force locates at an angle around 70° . Section III is a constant back suction pressure acting on the leeward side. The circumferential distribution is shown in Figure 3.5.

Niemann and Höffer (2009) proposed a more comprehensive calculation method for determining the static wind pressure coefficient on solar updraft tower. The distribution of external pressure coefficients varies over height. The equation is derived according to experimental result from wind tunnel measurement of solar updraft tower and measurement in natural scale at cooling towers (Niemann and Höffer (2009)). For modeling such large structure in finite element modeling in engineering application, the method from Niemann and Höffer (2009) would be sophisticated and it would increase much more analysis effort and easy to cause errors in the model for nonlinear analysis. The comparison between these two methods will be discussed in the Appendix A.

The magnitude of pressure coefficient distribution highly depends on the surface roughness of solar tower. A large surface roughness yields greater total drag force acting on the tower while decreasing

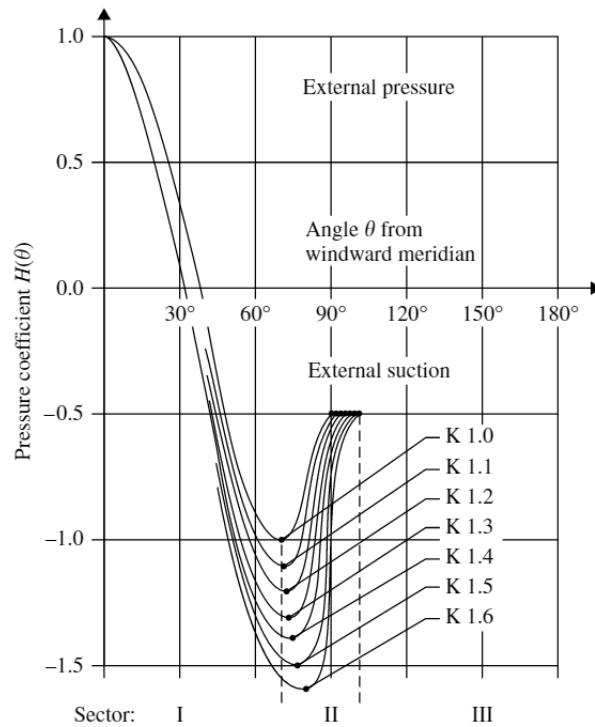


Figure 3.5: Types of circumferential pressure distribution (Phillip L. Gould; Wilfried B (2005)).

the maximum suction. It is a favorable effect on local deformation of tower shell such as of the circular cross-section. A roughness parameter can be decided by analyzing the stiffening ring layout at about one-third of the height of the tower. Laboratory and the experimental result determined this analyzing method, and the roughness parameter k/a_R is shown in Figure 3.6. As roughness parameter is known, according to Table 3.3, the specified pressure distribution can be determined. In this research project, the stiffening ring has the length around 7 meters with equal spacing 100 meters over the whole tower, which gives the roughness parameter of 0.07. Pressure distribution K1.0 is chosen for SUT coefficient distribution(Figure 3.5). The equation of each circumferential distribution curve is given in Table 3.4. The chosen pressure coefficient distribution over circumferential direction for the whole tower shows

Table 3.3: Roughness parameter and pressure distribution n curve with different types of ribs(Phillip L. Gould; Wilfried B (2005)).

Execution	Roughness parameter k/a_R	Pressure min c_{pa}	Pressure distribution
With ribs	0.025-0.100	-1.0	K 1.0
	0.016-0.025	-1.1	K 1.1
	0.010-0.016	-1.2	K 1.2
	0.006-0.010	-1.3	K 1.3
Without ribs	Smooth	-1.5	K 1.5
		-1.6	K 1.6

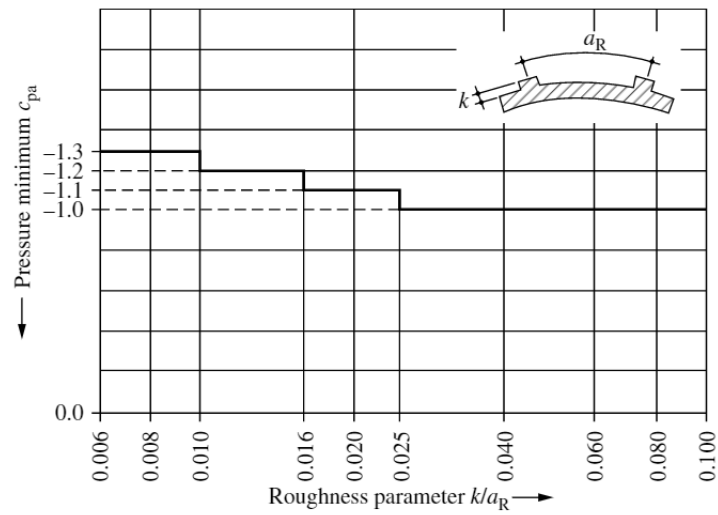


Figure 3.6: Surface roughness and types of pressure distribution (Phillip L. Gould; Wilfried B (2005)).

Table 3.4: Function of pressure coefficient over circumferential direction (Phillip L. Gould; Wilfried B (2005)).

Curve	p_{min}	Sector I	Sector II	Sector III	c_w
K 1.0	-1.0	$1 - 2.0(\sin(\frac{90}{71}\theta))^{2.267}$	$-1.0 + 0.5(\sin(\frac{90}{71}(\theta - 70)))^{2.395}$	-0.5	0.66
K 1.1	-1.1	$1 - 2.1(\sin(\frac{90}{71}\theta))^{2.239}$	$-1.1 + 0.6(\sin(\frac{90}{71}(\theta - 71)))^{2.395}$	-0.5	0.64
K 1.2	-1.2	$1 - 2.2(\sin(\frac{90}{71}\theta))^{2.205}$	$-1.2 + 0.7(\sin(\frac{90}{71}(\theta - 72)))^{2.395}$	-0.5	0.60
K 1.3	-1.3	$1 - 2.3(\sin(\frac{90}{71}\theta))^{2.166}$	$-1.3 + 0.8(\sin(\frac{90}{71}(\theta - 73)))^{2.395}$	-0.5	0.56
K 1.5	-1.5	$1 - 2.5(\sin(\frac{90}{71}\theta))^{2.395}$	$-1.5 + 1.0(\sin(\frac{90}{71}(\theta - 75)))^{2.395}$	-0.5	0.49
K 1.6	-1.6	$1 - 2.6(\sin(\frac{90}{71}\theta))^{2.085}$	$-1.6 + 1.1(\sin(\frac{90}{71}(\theta - 76)))^{2.395}$	-0.5	0.46

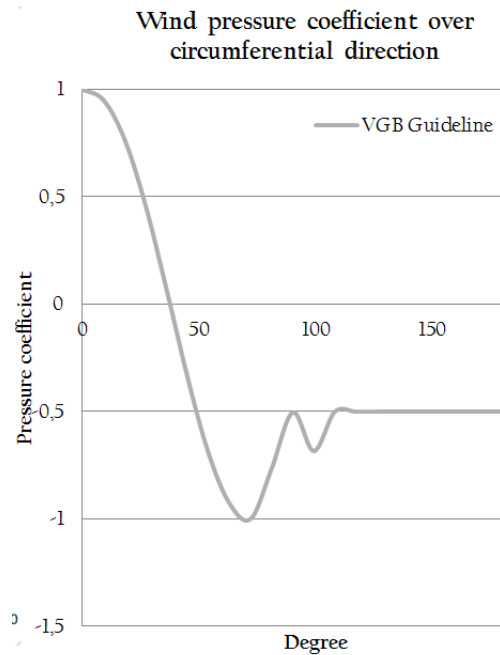


Figure 3.7: Pressure coefficient in the circumferential direction

in Figure 3.7.

3.3. Serviceability limit state

In serviceability limit state, the crack width and deflection of the structure should be within an acceptable limit. According to the Code of Practice for Structural use of Concrete Department (2013), the maximum allowable displacement at the top of the structure is 1/500th of the height. The Eurocode provides allowable maximum crack width for the reinforced concrete structure with the magnitude of 0.4mm. Depending on the environment of chosen location, the maximum crack strain might decrease to 0.2mm. The following loading combination are recommended (Phillip L. Gould; Wilfried B (2005)),

$$D + W \quad (3.17)$$

$$D + W + T \quad (3.18)$$

$$D + 0.70W + T \quad (3.19)$$

where

- D dead load for the shell wall and the stiffening rings
- W wind loading acting both on the external and the internal surface of the shell.
- T temperature loads.

The temperature load includes the collector temperature rising; operation temperature, asymmetrical due to the ambient air temperature, non-asymmetrical due to solar irradiation Lupi et al. (2015). Temperature effect is not considered in this research project, Equation 3.17 will be adopted.

3.4. Conclusions

In this chapter, the wind load calculation has been demonstrated. Given the hourly mean wind speed and surface roughness of the construction location, the vertical wind pressure profile based on Harris and Deaves (ISO4353 (2012)) equation coupled with Coriolis effect is calculated. From the calculation of the pressure coefficient of the natural draft cooling tower, it has been shown the surface roughness of the tower is the major factor for determining the wind load distribution. Once the wind load is determined, in the next chapter, a finite element model will be built with the defined geometry and the load acting on it.

4

Finite element modeling

In this chapter, the finite element modeling setup is discussed in detail. Here gives the modeling procedure and the mesh refinement. The element types for different structural components are introduced. The cross-sectional analysis of the stiffening rings is done for detailing the geometry. Material properties used in the linear analysis will be discussed.

4.1. Software Choice

The variety of FEM software in Civil Engineering application is large, and the most commonly used are ABAQUS, ADINA, ATENA, DIANA. For modeling reinforced concrete shell structure with nonlinear physical properties, their comparisons about modeling nonlinear reinforced concrete structures are discussed in Appendix A.

In this research, the pre-processing for modeling takes place in FX+ for DIANA, the analysis and the post processing takes place in DIANA 10.0. Using DIANA 10.0 is not only due to the license availability but also due to its capacity of modeling reinforced concrete. DIANA offers varieties of cracking models, tensile models, compressive models to simulate the complex mechanisms of reinforced concrete structure. Nonlinear models are chosen by the specific analysis type and the particular structural scale. To investigate crack behavior for a large-scale structure under complex loading conditions, DIANA provides the total strain rotating crack model which is rather robust and stable. DIANA is also available for dynamic analysis and geometrical non-linearity, which is helpful for future research.

4.2. Modeling methodology

The finite element modeling is the dominant discretization technique that subdivides the geometrical model into components called finite elements or integrators. Each element is connected to each other by nodal points. Each node has a finite number of degree of freedoms. Inside the integrators, there are a finite amount of integration points. In DIANA, a displacement based method is employed. The displacement on the node is the primary unknown. At the integration points, the strain and stress are calculated by the increment of displacement. After integrating of the stress field, the nodal forces are calculated, the final goal of the analysis is to make the nodal forces from different elements in equilibrium. Figure 4.1 shows the necessary steps for building up the solar updraft tower model in FX+ for DIANA. Before mesh, the material properties will be added and the element type is selected. The material is assigned to the element type, and the element type is assigned to each discrete elements on the model.

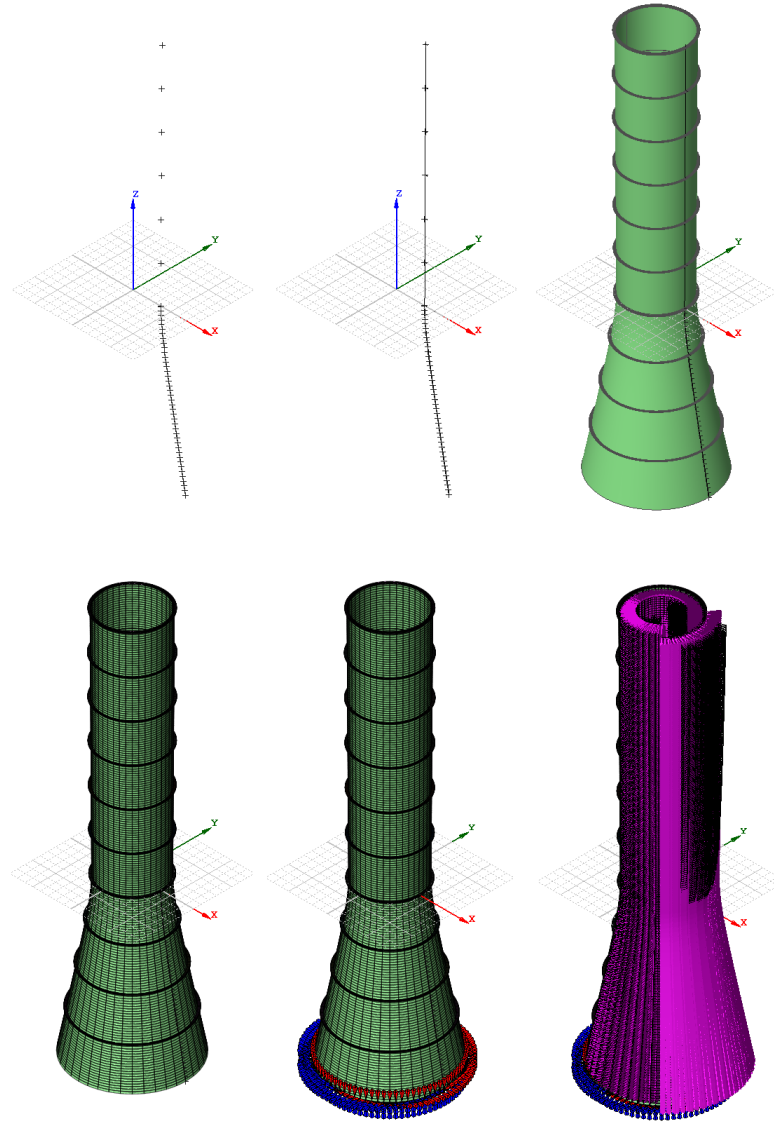


Figure 4.1: Procedures for building up the FEM, 1st Determine the compound points, 2nd Connect point by 3D lines, 3rd Revolution around central z axis, 4th Mesh the geometry, 5th Setting boundary conditions, 6th Adding loads.

4.3. Material properties

Before defining element type, the material properties are determined. Concrete and steel reinforcement are the two material types in the solar updraft tower. Their properties are defined according to Eurocode EN1992-1-1 (2011) which is the design regulation for reinforced concrete structure. These properties are the inputs for linear analysis and the primary inputs for nonlinear analysis. The non-linearity of the concrete and the steel reinforcement will be reported in detail in Chapter 6.

4.3.1. Concrete material

In the final structural design phase, the concrete class will vary with height, but for the sake of simplification, C50/60 concrete quality will be used for the entire structure (Niemann et al. (2009)). The following equations give the concrete strength and the concrete linear material properties.

$$f_{ck} = 50 \text{ MPa} \quad (4.1)$$

$$f_{cm} = f_{ck} + 8 = 58 \text{ MPa} \quad (4.2)$$

$$f_{ctm} = 0.3 f_{ck}^{2/3} = 4.1 \text{ MPa} \quad (4.3)$$

$$f_{ctk} = 0.7 f_{ctm} = 2.9 \text{ MPa} \quad (4.4)$$

$$f_{cd} = \frac{\alpha_{cc} f_{ck}}{\gamma_c} = \frac{f_{ck}}{1.5} = 33.3 \text{ MPa} \quad (4.5)$$

$$f_{ctd} = \frac{\alpha_{ct} f_{ctk,0.05}}{\gamma_c} = \frac{f_{ctk}}{1.5} = 1.93 \text{ MPa} \quad (4.6)$$

$$E_{cm} = 22 [f_{cm}/10]^{0.3} = 37 \text{ GPa} \quad (4.7)$$

$$\nu_c = 0.2 \quad (4.8)$$

$$\rho_c = 2500 \text{ kg/m}^3 \quad (4.9)$$

where

γ_c	partial factor for concrete
f_{ck}	characteristic compressive cylinder strength of concrete at 28 days
f_{cm}	mean value of concrete cylinder compressive strength
f_{ctm}	mean value of axial tensile strength of concrete
E_{cm}	secant modulus of elasticity of concrete
ν_c	concrete Poisson ratio
ρ_c	density of concrete
f_{ctk}	Characteristic axial tensile strength of concrete

According to Eurocode EN1992-1-1 (2011), the characteristic compressive strength used for structural design and analysis is defined such that only 5% of all possible strength that measured is lower than the value of f_{ck} . For serviceability limit design state which refer to the durability, overall stability, fire resistance and deflection, a mean compressive strength will be considered. The tensile strength of concrete highly depends on the curing condition and dimension of structural members, while EN1992-1-1 (2011) gives the tensile strength f_{ctm} as an approximation. The modulus of elasticity of concrete depends on the modulus of elasticity of its components. An approximate value is given called E_{cm} . The Poisson's ratio is taken to 0.2 concrete.

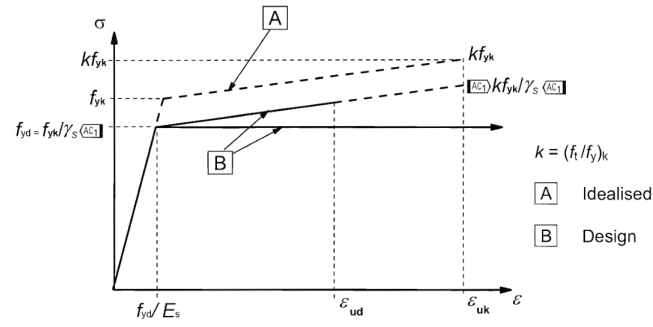


Figure 4.2: Stress-strain relation for reinforcement (EN1992-1-1 (2011))

4.3.2. Reinforcement

The reinforcement properties will be identical both for in the shell wall and the stiffening ring. The steel quality is B500A for this design. Figure 4.2 provides the material model according to EN1991-1-4 (2011). EN1992-1-1 (2011) Annex C provides the value of ultimate strain limit and maximum stress limit for defining the inclined top branch of the stress-strain curve. In this research, the k value is 1.08, and characteristic strain at maximum force is 5%.

$$f_{yk} = 500 \text{ MPa} \quad (4.10)$$

$$f_{yd} = \frac{f_{yk}}{\gamma_s} = \frac{500 \text{ MPa}}{1.15} = 435 \text{ MPa} \quad (4.11)$$

$$E_p = 200 \text{ GPa} \quad (4.12)$$

$$\rho_s = 7850 \text{ kg/m}^3 \quad (4.13)$$

$$\nu_s = 0.3 \quad (4.14)$$

where

- f_{yk} characteristic yield strength of reinforcement
- f_{yd} design yield strength of reinforcement
- E_s design value of modulus of elasticity of reinforcing steel
- ρ_s mean density of reinforcing steel
- ν_c Reinforcement Poisson ratio

4.4. Meshing

4.4.1. Shear locking

An important aspect to consider when modeling thin shell structure is the element size. The accuracy of finite element solution will decrease when the thickness of element length $\frac{t}{L}$ ratio falls (Bathe (2011)). Compared to the exact solution, the numerical solution has exceedingly stiff behavior. This is known as shear locking. A treatment such as increasing meshing densities to find the proper $\frac{t}{L}$ ratio is necessary so as for the element size.

An incorrect choice of the shape of the element also leads to locking. The use of triangular element makes the mesh easier compared to the use of quadrilateral elements for complex geometry. However, for the fully integrated linear triangular element with an incompressible material property or with solids with revolution or highly constraint boundary condition, their displacements on nodes

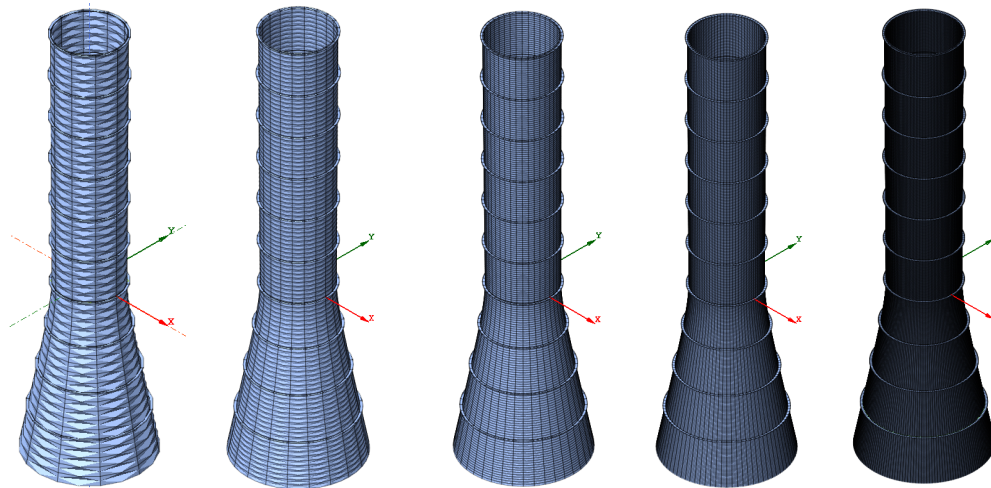


Figure 4.3: Mesh scale from very coarse(1st) coarse(2nd), intermediate(3rd), fine(4th), very fine(5th).

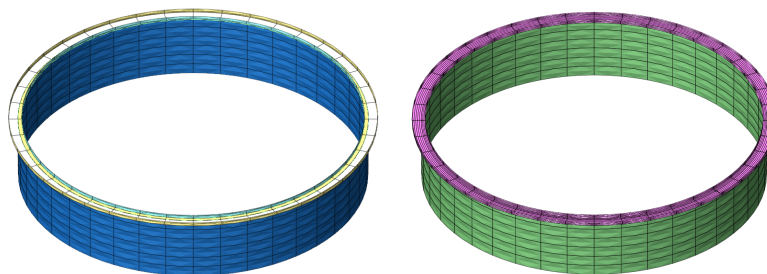


Figure 4.4: The mesh refinement of the top stiffening ring before(left) and after refinement(right)

are going to be fully locked. This phenomenon is also known as volumetric locking. This extreme case shows triangular elements are more prone to locking. The shear locking also occurs when the fully integrated linear element is applied under pure bending. Since the linear element has to deform linearly, an extra shear strain is generated which it should not exist.

The discussion above revealed that the choice of proper elements is vital. Firstly it is necessary to find the is element size according to the shell thickness. A quadrilateral element shape is chosen to avoiding volumetric locking. Also, for nonlinear analysis, all element types should be quadratic.

Meshing densities analysis For finite element modeling, one of the key concepts is mesh convergence. The model with finer mesh has more accurate solution and avoids shear locking. This is because a fine mesh also implies a longer calculation time, and coarse mesh results in a less accurate result. Therefore, models with different mesh densities are investigated. There are five models with increasing mesh densities. The very coarse model (810 elements), the coarse model (2620 elements), the intermediate model (9240 elements), the fine model (34480 elements) and the very fine model(132960 elements). The shell wall and the stiffening ring were modeled by using curved shell elements. The stiffening ring are modeled according to the original design of Krätzig & Partner. Figure4.5 shows the five models with increasing mesh densities from the left to the right.

Eck et al. (2015) performed a mesh-density analysis using ANSYS. Instead of using curved shell element, the beam element was adopted for modeling the stiffening rings. The beam element has a rectangular cross-section of $4.5 \times 1.5m$. The mesh densities analysis of van Eck(Eck et al., 2015) (Figure 4.5) shows a good consistency for first seven eigenfrequencies for all models. For this research model, due to the complexity of the geometry of the stiffening rings (see Figure 2.4), the model is

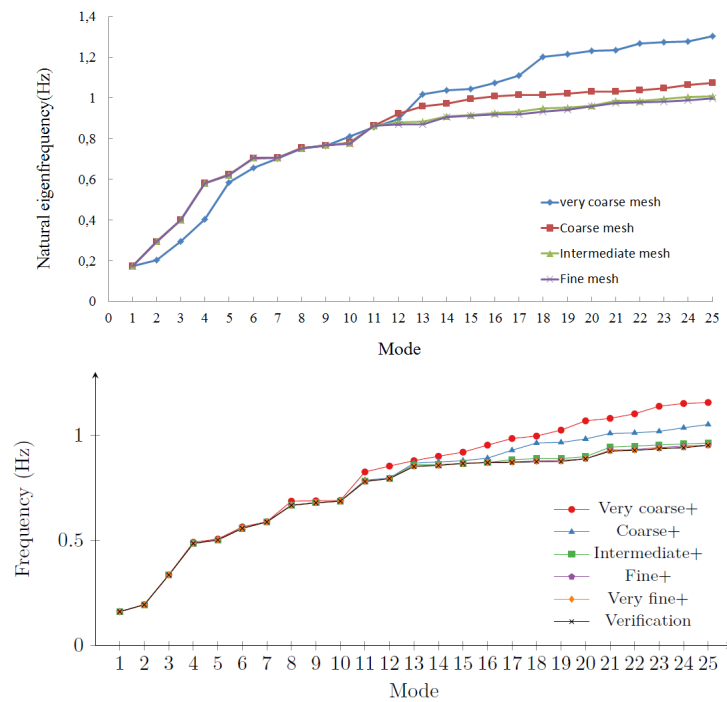


Figure 4.5: Natural frequencies with different mesh densities with curved shell element modeling the stiffness rings(top) and Natural frequencies with different mesh densities for beam element modeling the stiffening ring ((Eck et al., 2015))(bottom)

more sensitive to the mesh densities, which gives more scattered result between models. As can be seen in the figure, except for the first natural frequency, the very coarse mesh and coarse mesh gives a big difference in natural frequency compared to these of intermediate mesh and the fine mesh. Due to coarse mesh gives very low $\frac{t}{L}$ both at the rings and the shell wall which might give an over stiff behavior. The stiffer structure gives a higher natural frequency. This is also due to the shell vibration occur from the second eigenfrequency and it is more sensitive to the meshing size of the shell wall and the stiffening rings. However, the models of intermediate and fine mesh give consistent result even when the natural frequency is high. Furthermore, the intermediate mesh shows nearly the same result as eigenfrequencies the model with fine mesh. The intermediate mesh densities will be taken for this research project. For intermediate mesh, the tower is divided into 40 segments in the circumferential direction and is split into 20 sections every 100 meters in the vertical direction.

4.4.2. Mesh refinement

Mesh refinement is necessary for nonlinear analysis with complex geometry at the cost of increasing the computational time. Whereas mesh refinement also means more calculation time. Finding a proper mesh scale is required before proceeding nonlinear analysis. The stiffening rings are one of the key components in solar updraft tower design. The eigenfrequency varies considerably by slight changes in the ring shape. The sensitivity of rings on the complete structural response is high. Here, the mesh on the stiffening ring will be refined into smaller element sizes. Figure 4.4 gives the mesh of top stiffening ring before and after refinement. The same refinements were done for intermediate stiffening rings.

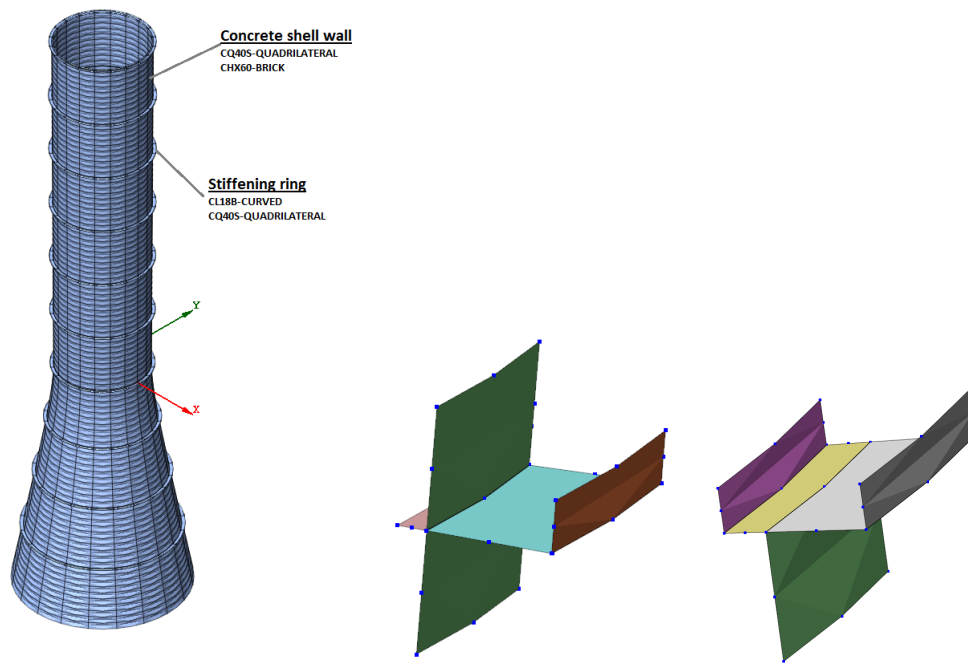


Figure 4.6: Finite element model of solar updraft tower(left) and finite element model of the connection between the shell wall with the intermediate ring(middle) and top stiffening ring(right)

4.5. Structural elements

4.5.1. Introduction

DIANA offers many different types of elements. Two questions need to be answered before having an accurate result of nonlinear analysis. One is the way to model such large-scale SUT, and the other is how much detail should be incorporated. Certain types of the element often serve a particular structural element or analysis. For example, 3D-solid element produces an extensive system of equations which increases analysis cost and time, particularly for nonlinear analysis. However, the 3D-solid element has to be applied to the model with the massive concrete block or the soil block. Choosing a proper element type can give a feasible result and a reasonable calculation time. The different types of element in DIANA that can be possibly used in this research project are listed below.

- CQ40S-QUADRILATERAL, 8 nodes. Curved shell element can be used for modeling the shell wall and the stiffening ring.
- CHX60-BRICK, 20 nodes. The solid element as an alternative for modeling the shell wall.
- CL18B-CURVED, 3nodes. Beam element can be used for modeling the stiffening ring.

4.5.2. The shell wall modeling

Two possibilities for modeling the shell wall are the curved shell element and the 3D solid element. The curved shell element produces a good approximate if the thickness of the element is thin compared to dimension b in the plane of the element. The 3D solid element normally is used only when there is no other option on the element types (DIANA (2016)).

The reason for using curved shell element instead of 3D solid element are many. First, complex modeling with long calculation time usually boosts the cost of the analysis. Second, instead of the discretizing problem in the thickness direction, using kinematical assumption in curved shell element

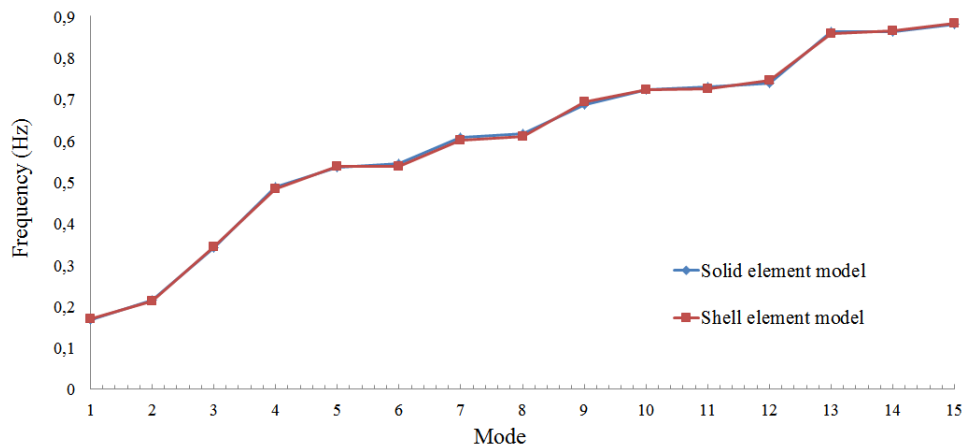


Figure 4.7: Natural frequencies of curved shell element model and 3D solid element model

to distribute displacement over the thickness reduces the complexity of analysis. To maximize the accuracy of nonlinear analysis, the shell wall will be modeled by curved shell element.

Two models were generated. Their shell wall was modeled by solid element and curved shell element respectively. Solid element CHX60 is 20 nodes solid brick element. It is based on quadratic interpolation. Curved shell element CQ40S has eight nodes and quadrilateral shape. The stiffening rings were modeled by 3D beam element with rectangular cross-section size of 4.8mx1.55m. For both models, eigenfrequency analysis was done. In Figure 4.7, the first 15 eigenfrequencies of solid element model as well as shell element model. With intermediate mesh density, two models give consistent first 15 natural frequencies and identical shapes. Due to solid element has a large system of equation, which increases the calculation time considerably for nonlinear analysis. Curved shell three will be adopted for this research project.

4.5.3. The stiffening rings modeling

The stiffening ring can be modeled by curved shell elements and 3D-beam elements. The cross-sectional area of the stiffening ring is small compared to the circumferential ring length, so it is possible to use beam elements to model the stiffening rings. To model nonlinear behavior of large-scale continuous concrete shell structure in DIANA, large quantities of elements are required. Therefore, a long computational time is expected. If simplifying stiffness ring modeling by using the beam element yields the similar result as that of using shell element, a simpler model, as well as less computation time, will be preferred. However, concerning the complex wind load pattern acting on the structure, the capability of 3D beam element to adequately demonstrate the real structural behavior might be insufficient. Therefore, a comparison between the stiffening rings modeled by the curved shell element and the 3D beam element is conducted in the Appendix C.

Modeling ring by curved shell element

The geometry of a top and mid stiffening ring influence the structural performance considerably. An exact geometry based on the technical drawings of the top and intermediate stiffening ring by Krätzig & Partner is modeled and they are connected to the shell wall. Figure 4.6 shows the connection of the shell wall and stiffening ring.

Modeling ring by beam element

Eck et al. (2015) performed the linear analysis by using the beam element to model stiffening rings.

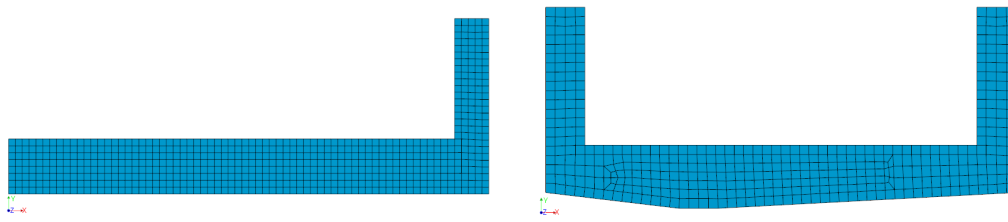


Figure 4.8: Mesh of cross-section of the top(right) and intermediate(left) stiffening ring

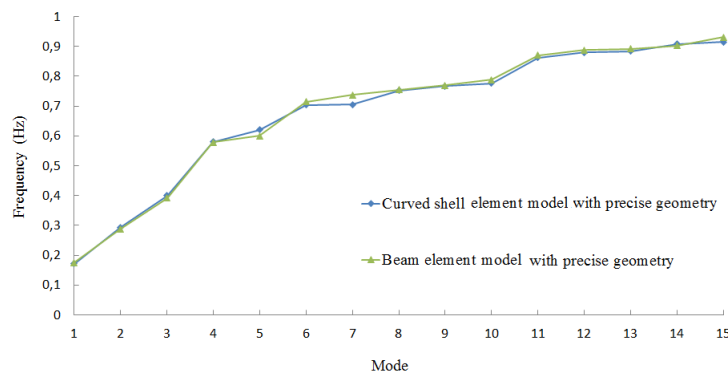


Figure 4.9: Eigenfrequencies of curved shell model with precise geometry and beam model with precise geometry

The beam has a rectangular shape with the size of 4.5x1.5m. The mass center of the cross-section of the ring is located at the mid-surface of curve shell wall. It is a simplified way of modeling the stiffening ring of Krätzig & Partner. However, the accuracy of the modeling stiffening ring becomes of importance to reveal real structural behavior for nonlinear analysis. A detailed comparison between model according to Eck et al. (2015), the model with curved shell element with exact ring geometry and model with 3D beam element with precise ring geometry are investigated.

Before the comparison, a cross-sectional analysis of the top and intermediate stiffening ring has to be conducted to get the cross-sectional properties of the stiffening rings which will be the input for 3D beam element. This section will analysis the properties of the top and the intermediate stiffening ring cross-section, whose geometry is based on the original design of Krätzig & Partner (Lupi et al. (2015)). These cross-sections are defined in the XY-system. The CQ8TO eight-node quadrilateral isoparametric element was adopted for this two-dimensional cross-section analysis. It is based on quadratic interpolation and Gauss integration with 2x2 integration scheme. Figure 4.8 displayed the mesh of top and intermediate stiffening ring cross section. The output of cross-sectional properties of the top and intermediate stiffening ring was shown in Table 4.1.

Two models were built with precise geometry according to the original design of Krätzig & Partner while one is modeled by curved shell element, the other is modeled by 3D class beam element. Eigenvalue analyses were conducted, and the first 15 eigenfrequency shows in 4.9. The curved shell model and beam model with precise geometry have similar results. Two models also have identical mode shapes. The results concluded that two types of elements give similar results in the linear analysis. Since in linear analysis, the results reveal no significant differences between using beam element and shell element, a comparison between these two model in physical nonlinear analysis will be con-

Table 4.1: Cross-sectional properties of stiffening ring

		Formula	Top ring	Intermediate ring
Moment of inertia (m^4)	I_y	$\int_A z^2 dA$	2.5120	1.4180
	I_z	$\int_A y^2 dA$	25.1800	31.2100
	I_t		0.8563	1.1940
Extreme fibers (m)	y_{max}		3.0540	3.2530
	y_{min}		-2.9640	-3.9780
	z_{max}		1.7700	1.6960
	z_{min}		-0.7966	-0.8931
Sections moduli (m^3)	W_{ymax}	I_y/z_{min}	8.2450	9.5950
	W_{ymin}	I_y/z_{max}	8.4970	7.847
	W_{zmax}	I_z/y_{min}	1.4190	0.8365
	W_{zmin}	I_z/y_{max}	3.1540	1.5880
Center (m)	X_c		1.2590	2.4890
	Y_c		0.4024	0.1723
Axis (rad)	α		0.0077	0.1060
Area (m^2)	A		6.0000	6.4750
Shear center (m)	e_y		-0.0584	2.048
	e_z		-1.0100	-0.4554

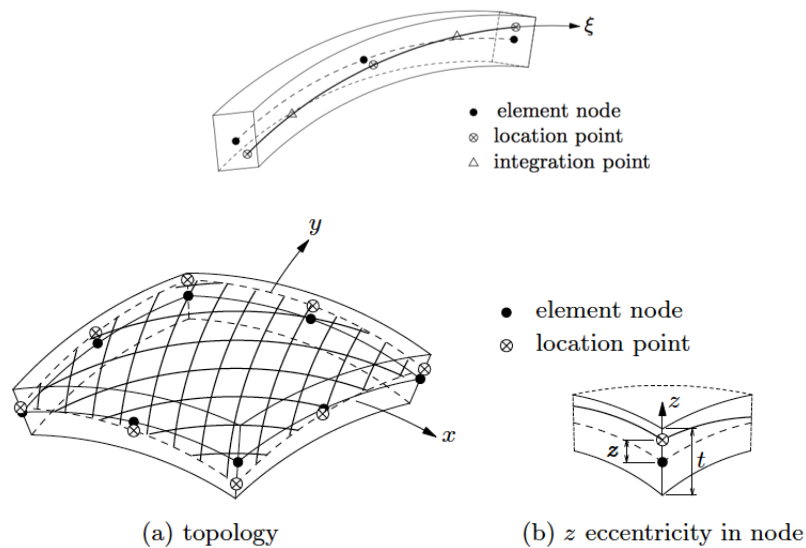


Figure 4.10: Bar particles in beam element (top) and grid reinforcement in curved shell element (bottom) (DIANA (2016))

ducted in the later chapter.

4.5.4. Reinforcement

Certain reinforcement ratios are required both for the shell wall and stiffening ring. In curved shell element, a layer of grid reinforcement is embedded at the mid-surface of the shell. In reality, two layers of reinforcement will be constructed with a concrete cover of 40mm. A sub research is performed in Appendix B for comparing the differences of nonlinear result between a one layer reinforcement layout and a two layers reinforcement layout. In beam element, the bar reinforcement is chosen and located at the exact location of the center line of the beam element. This section explains the background theory of embedded reinforcement and its working principal.

Working principals

Reinforcement is embedded in the mother element and embedded reinforcement element has the following characteristics:

- The the particles of the reinforcement are embedded in what is called the mother element.
- DIANA ignores the self-weight and volume of the embedded reinforcement element.
- The embedded reinforcement does not have degrees of freedom of its own. The displacement follows the mother element, which means that reinforcement is perfectly bonded to the mother element.
- The embedded reinforcement does not have to be located along a mesh line, but it has to be inside the cross-section of the mother element.

Bar reinforcement in beam element

Bar reinforcement has the shape of a line and is divided into particles by specifying location points. Some location points are in the intersection of bar and the mother elements; some are located in between to define curvature. The integration points are specified according to the integration scheme of the mother element. It has variable of strain $\epsilon_{xx}, \sigma_{xx}$ stress in direction tangential to the bar axis. Figure 4.10 shows an example of a quadratically curved bar reinforcement embedded in a curved beam.

Grid reinforcement in curved shell element

Grid reinforcement is a plane shape 2D element that can be embedded in some 2D and 3D mother element. Grid reinforcement is also considered to be subdivided into particles. The dimension of particles depends on the boundary of the mother element. DIANA numerically integrates these particles independently. The integration point on the particles depends on the integration scheme of the mother element. The variable of a grid reinforcement are strain $\epsilon_{xx}, \epsilon_{yy}$ and stress σ_{xx}, σ_{yy} in user-defined x-and y-direction. For grid reinforcement, the equivalent thickness should be specified, which should be in the thickness domain of the curved shell element. Figure 4.10 shows the grid reinforcement in curved shell element.

4.5.5. Integration schemes

The CQ40S-quadrilateral element with eight nodes is chosen for modeling shell wall of the SUT and the stiffening ring of SUT. It is based on quadratic interpolation and Gauss integration. For linear analysis, 2x2 Gauss integration scheme was chosen over the surface area, and 3 points Simpson integration scheme is chosen in the thickness direction.

Due to compatibility between the shell wall and stiffening ring, the 3 nodes 3 dimensional Class III beam element CL18B is chosen. For linear analysis, two point Gauss integration scheme is chosen along the bar axis. In cross-sectional direction, the 3-point Composite Simpson integration scheme was chosen. Figure 7.2 specifies the Gauss and Simpson integration scheme. However, for nonlinear analysis, the complex reinforcement bar layout requires more integration points both in bar axis and cross section. A high integration scheme was chosen.

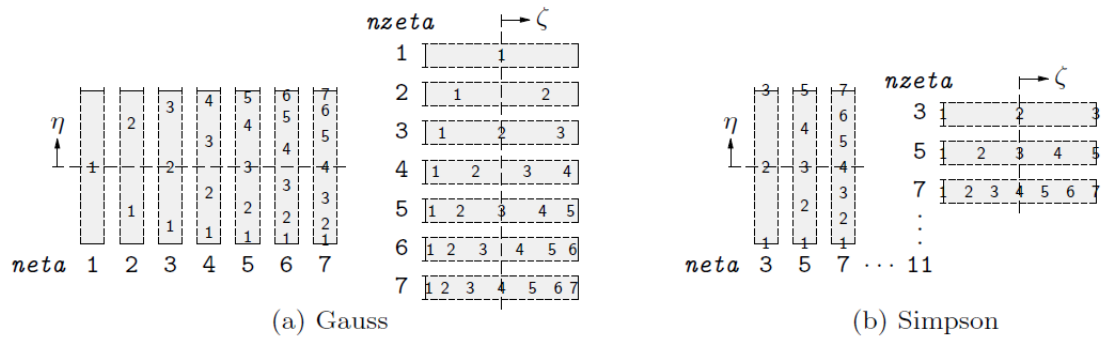


Figure 4.11: Integration schemes in quadrilateral zone (DIANA (2016))

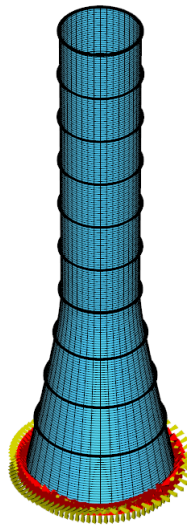


Figure 4.12: Boundary conditions of the solar updraft tower

4.6. Boundary conditions

For a 1000m tall SUT, the foundation consists of a reinforced concrete circular ring beam with the width of 22m, 6m in thickness and 28m in diameter (Lupi et al. (2015)). The large self-weight of the RC solar updraft tower requires a good soil condition. It is assumed that the soil stiffness of the selected location exceeds 10GPa. The eigenfrequency analyses with different soil stiffness were conducted in the original research project of Eck et al. (2015). The behavior of the SUT with soil stiffness of 10GPa behave almost exactly to the SUT with the fixed boundary condition at the bottom Eck et al. (2015). It is concluded, the soil effect on the structure can be ignored with the stiffness equal or over 10GPa and the fixed boundary condition will be added at the bottom of the tower shell wall. Figure 4.12 gives the FE model with fixed nodal constraint at the base of the tower and the boundary condition setting will be used for both linear and nonlinear analysis.

4.7. Conclusions

The following conclusions are drawn concerning the modeling procedure of a solar updraft tower.

- The purpose of research lead to a correct selection of the software. DIANA has fulfilled the re-

quirements on concrete nonlinear modeling.

- Concrete C50/60 is chosen for both the shell wall and stiffening ring. Reinforcement B500A was chosen. Their properties were calculated based on EN1992-1-1 (2011). For linear analysis, only Young's modulus, Poisson ratio and mass density were considered. Other properties will be applied in material nonlinearity analysis, see Chapter 6.
- Several models with different mesh density were compared by eigenvalue analysis. First, the mesh densities have the vital influence on the accuracy of eigenvalue analysis. Second, the intermediate mesh density with mesh refinement on the stiffening rings shows sufficient accuracy.
- Two types of the elements were discussed in detail. Models with different element types were compared. Their stiffening rings were modeled by the curved shell elements and 3D beam elements respectively. Their structural behaviors are similar to the linear analysis.
- Two ways of modeling reinforcement were mentioned. One is the reinforcement grid applied to the curved shell element, and the other is reinforcement bars applied to the 3D beam element.

The verification of the model and accompanying discussion is presented in the next chapter. The accuracy of the finite element model is essential before performing a nonlinear analysis. The model complexity of the linear model proposed by literature might not be sufficient for nonlinear analysis. This observation will be further elaborated in the next chapter.

5

Linear analysis

After the detailed explanation about the FEM setup, this chapter firstly gives results of the eigenvalue analysis and the linear static analysis to verify the accuracy of the model and later, shows the analysis results of another model who has more precise detail on geometry of the stiffening rings.

5.1. Introduction

For model verification, the comparisons of analysis results between a linear model and the two models from the literature are done. The both analysis results can show the accuracy of the geometry input, the boundary conditions, the sufficiency on meshing density as well as the stiffness of the model. With static analysis result verification, the accuracy of the complex wind load input can be ensured. The material nonlinear analysis will be performed later in this research project, and because the geometry of the stiffening ring is simplified, this linear model might not sufficient to show the real structural behavior. Thus, it is of interest to understand how much influence on linear analysis if the structure is modeled further in detail. In this chapter, two models were built, they are:

- *Simple Linear Model (SLM)* is identical to the base model from the original research project of Eck et al. (2015).
- *Detailed Linear Model (DLM)* is a model that has detailed geometry on modelling the stiffening rings using 3D calss-III beam element.

5.2. Model setup

The summaries of the model setup of these two models is shown in this section. It will be introduced through explaining their similarities and differences.

5.2.1. Similarities

Two models have an almost identical geometry except for the stiffening rings. They have same choices on the element types, the meshing density, the material properties, the loading and the boundary conditions.

Geometry

The similarities on geometries listed below:

Tower Height: 1000.00m

Tower Throat Height: 400.00m

Tower Transition Height: 401.81m

Bottom Radius: 140.00m
 Throat Radius: 75.00m
 Top Radius: 77.97
 Tilt Angle: 14°

Both models have the same wall thickness. In Chapter 2, the thickness function over height is shown in Figure 2.1.

Material properties

The normal concrete with class C30/37 is used. Its linear properties are the following:
 Concrete Young's modulus: 37GPa
 Concrete Poisson ratio: 0.2
 Concrete density: 2500kg/m³

Meshing and element type

For the intermediate meshing density, the tower is divided into 40 segments in the circumferential direction, and into 20 segments in every 100 meter in the vertical direction.

For the element types, two models use the curved shell element CQ40S-QUADRILATERAL with eight nodes for modeling the shell walls and use 3D class III beam element CL18B with three nodes for modeling the stiffening rings.

Loading and boundary condition

The eigenvalue analysis considers the self-weight of the SUT, and later for the linear static analysis, the static wind load is modeled. The wind load will be calculated based on the averaged hourly design wind speed with the magnitude of 24.5m/s at the height of 10m. The free stream wind pressure profile over height is given in Figure 3.4. The pressure coefficient distribution over the circumferential direction is shown in Figure 3.7. In this chapter, the ultimate limit state analysis is considered. The load factor for the self-weight and the wind load are 1 and 1.5 respectively.

For the boundary conditions, the nodes at the base will be fixed. No translations and rotations are allowed.

5.2.2. Differences

The only difference between Simple Linear Model(SLM) and Detailed Linear Model(DLM) is the stiffening rings geometry. For SLM, the stiffening rings have a rectangular cross-section with a dimension of 4.5x1.5m located at the mid-surface of the shell wall. For DLM, the stiffening rings are identical to the original design of Krätzig & Partner (Lupi et al. (2015)), their technical design drawing and ring cross-section analysis can be found in Figure 2.4 and Table 4.1. The cross-sectional mass center of the stiffening rings are located outside the middle surface of shell wall according to the original design from Krätzig & Partner (Lupi et al. (2015)).

5.3. Model Verification

In this section, the structural response of Simple Linear Model will be compared to the analysis result from the original research of Eck et al. (2015).

5.3.1. Eigenvalue analysis

This research takes prime attention to static response with material non-linearity. The dynamic response in this research is used for model verification, a detailed dynamic analysis under wind action can be found in the original research of Eck et al. (2015). SLM model setup is identical to the base model of Eck et al. (2015), and is comparable to the model from Harte and Krätzig (2011). As presented in Figure 5.1, the first six eigenfrequencies of SLM are almost identical to the result from Eck et al. (2015), the errors margins in table 5.1 shows that the maximum difference is 6% at the fourth frequency. The result shows that the accuracy of the model regarding the stiffness, the geometry, the

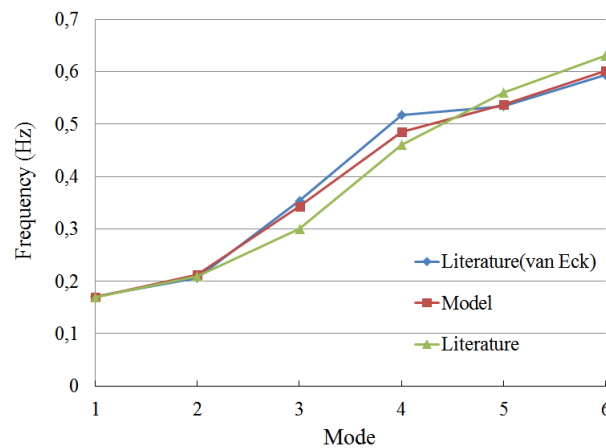


Figure 5.1: Comparison among the calculated eigenfrequencies of Simple Linear Model, results from Eck et al. (2015) and results from the literature Harte and Krätzig (2011)

element type, the meshing density and the boundary conditions are sufficient. Compared to result from Harte and Krätzig (2011), the results are not completely similar, while they both have identical mode shapes.

The free vibration response shows the dynamic deformation capability of a structure. Figure 5.2 gives the first 6 mode shapes of SLM and they are identical to the base model from the original research project of Eck et al. (2015). The first vibration mode is a beam-like dynamic behavior, which shows a global deformation on the structure without local deformation of the cross-section of the tower. The other five vibration modes are more shell-like dynamic behavior.

5.3.2. Linear static analysis

Up to this point, the eigenvalue analysis shows a good similarity between Simple Linear Model and models from the literature. In the static analysis, the comparison of the displacements and in-plane forces will be shown.

Displacement

The displacement in the SUT can be divided into three directions: 1) the along wind direction; 2) the cross wind direction; 3) the vertical direction. Obviously, the wind load tries to push over the tower which indicates the dominating displacement would be in the along wind direction. Furthermore, the deformation in the cross wind direction depicts the local shell deformation of the upper cone. Figure 5.3 shows the deformed shape of the tower with the along-wind displacement contour (left) and the cross wind displacement contour (right) over the tower. The maximum displacement the along-wind direction is 2.18m and 2.27m at the top of the SUT for SLM and the base model from Eck et al. (2015) respectively. A marginal difference of 4% is found. The deformation of the upper cone causes a displacement in crosswind direction about 1.15m in both sides symmetrically. From the deformed shape, it can be concluded that the tower deforms globally like a cantilever beam, and also deforms locally at the upper cone by ovalizing.

In plane forces

Thin shell structure can resist the forces both parallel and perpendicular to the shell surface. The stress resultants are calculated by integrating the stress in the thickness direction, which based on the middle surface of the shell. The stress resultants line diagram in meridional direction N22 will be considered.

Figure 5.4 shows the comparison of stress resultant (N22) in line diagram over the height of the

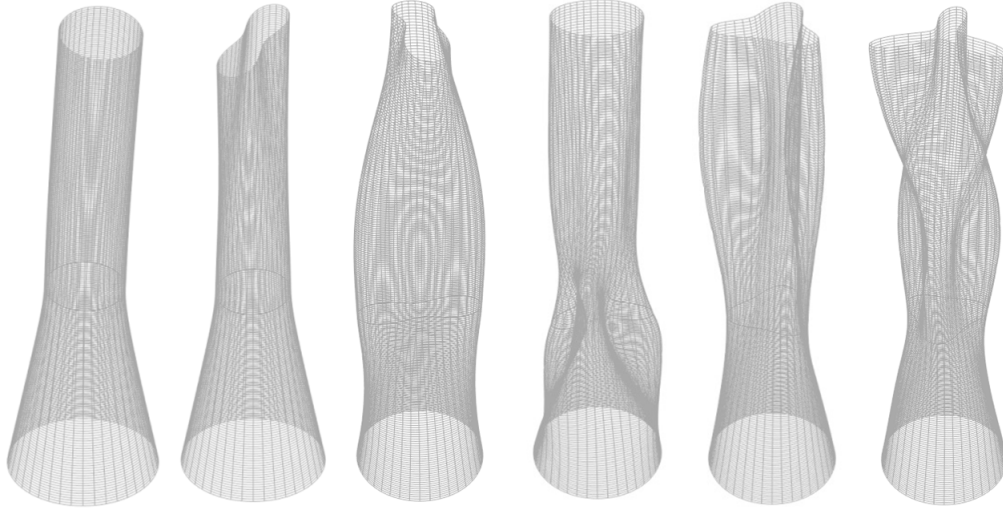


Figure 5.2: The first 6 free vibration mode shapes for Simple Linear Model the 1st (most left) and the 6th (most right)

Table 5.1: Verification of eigenfrequency and their error margin among Simple Linear Model and result from Eck et al. (2015) and from Harte and Krätzig (2011)

Mode	Frequencies				
	Eck 2015	Literature	SLM	Error %	
		Harte2011		Eck 2015	Harte 2011
1	0.1715	0.17	0.1690	1.44%	0.57%
2	0.2068	0.21	0.2129	2.95%	1.38%
3	0.3537	0.30	0.3428	3.08%	14.26%
4	0.5170	0.46	0.4844	6.30%	5.30%
5	0.5345	0.56	0.5376	0.57%	4.007%
6	0.5936	0.63	0.6018	1.38%	4.480%

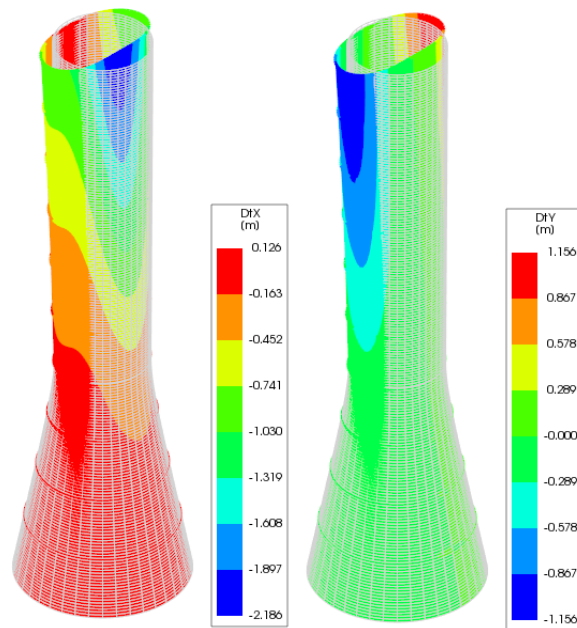


Figure 5.3: Deformed chimney (factor 30) with displacement distribution in the windward direction(left) and the cross-wind direction(right) under D+1.5W -Simple Linear Model

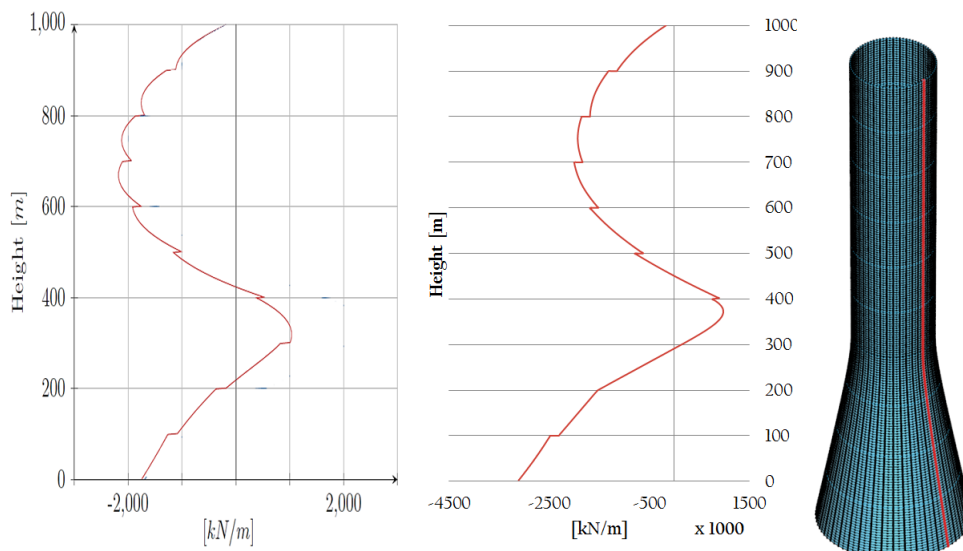


Figure 5.4: Comparison of in-plane meridional stress resultant distribution over height between literature Eck et al. (2015)(left) and Simple Linear Model(middle), the location that stress resultant distribution is calculated (right)

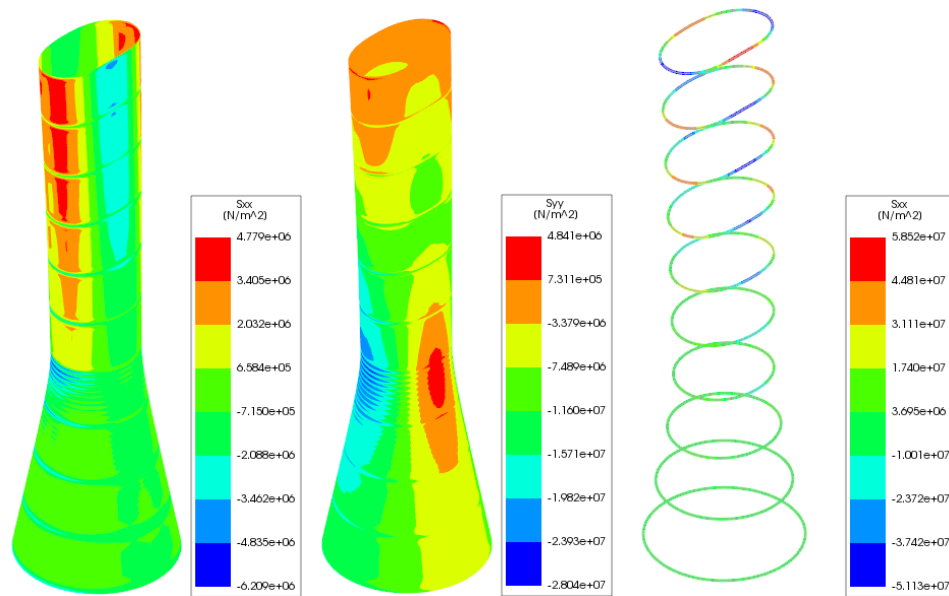


Figure 5.5: Circumferential stress distribution on the shell walls (left) meridional stress distribution on the shell walls (middle) and circumferential stress distribution on the stiffening rings (right) for Simple Linear Model (1D+1.5W)

tower between Simple Linear Model and the base model from Eck et al. (2015). These two curves are rather similar except for the stress resultant near the base of the tower. It is because the wind pressure varies every 5m in the vertical direction in SLM, while it varies every 100m in the base model of Eck et al. (2015). Since the wind speed was varying largely at a height near the ground level due to earth surface roughness, the result near the base with wind load will be different between those two models. Additionally, it is observed that the tower at throat height is under tension in both models with similar magnitudes.

Stress distribution

Figure 5.5 gives the circumferential stress distribution (S_{xx}) and the meridional stress distribution (S_{yy}) on the shell walls, as well as the longitudinal stress distribution on the stiffening rings. The maximum tensile stress in the shell walls is 4.8MPa in both directions, which exceeds the design tensile strength (2.9MPa). In the meridional direction, the tensile stress on the shell walls is concentrated both at the top tip and at the throat height of the tower. In the circumferential direction, the tensile stress is mainly concentrated at the upper cone since the circular cross-section deforms into an ellipsoid shape. For the stiffening rings, the maximum tensile stress is 58MPa. It gives a hint that the reinforcement both at the shell walls and the stiffening rings is needed. Furthermore, since the large tensile stress and compressive stress are concentrated at the stiffening rings, the stiffening rings should be more intensively reinforced compared to the reinforcement in the shell walls.

5.4. Detailed Linear model

Given the question that whether the detailed modelling of the stiffening is different in structural response compared to the simplified one, a comparison of eigenvalue analysis and static analysis between Detailed Linear Model (DLM) and Simple Linear Model (SLM) was done.

5.4.1. Eigenvalue analysis

In Figure 5.6, the first 15 eigenfrequencies of DLM and SLM are depicted. As can be seen, the first eigenfrequency are identical for both models. For the rest 14 eigenfrequencies, the eigenvalues of DLM are all higher than SLM. The changing in geometries of the stiffening rings show a bigger impact

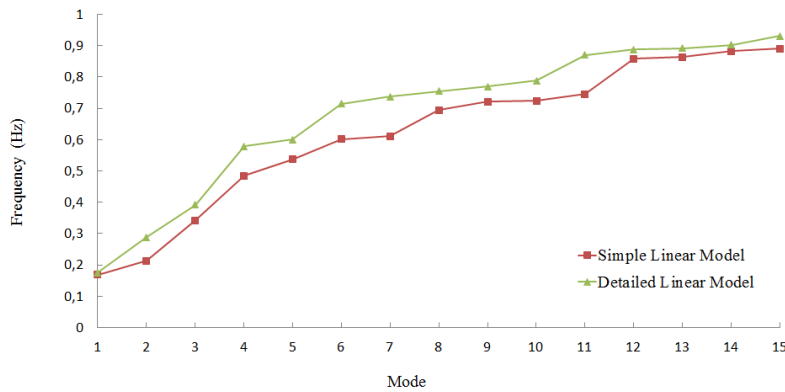


Figure 5.6: The first 15 natural frequencies of Simple Linear Model and Detailed Linear Model

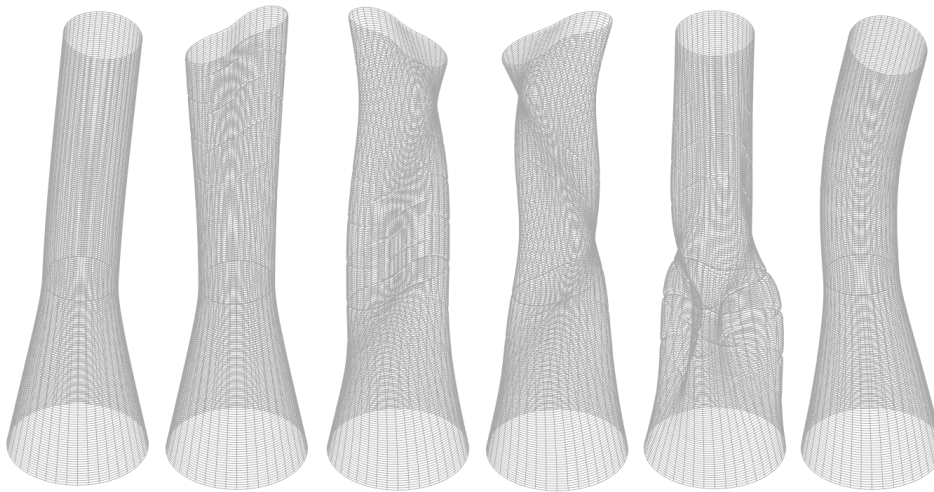


Figure 5.7: First 6 free vibration mode shapes for Detailed Linear Model (1st (most left) -6th (most right))

on the higher vibration mode.

To have a deeper understanding of the differences, the first six free vibration modes are given for DLM (Figure 5.7), and these modes can be compared with the mode shapes of SLM (Figure 5.2). The first eigenfrequency and the first mode shape are identical for both models. The second and third vibration modes have same mode shapes, while DLM has higher eigenfrequencies than SLM. After the third eigenfrequency, their eigenvalues and mode shapes are not synchronous. For SLM, except the first mode shape, other five mode shapes are shell-like vibration, which means the cross-section changes its shape. For DLM, the first and sixth both has a global vibration behavior without deformation on the cross-section of the shell structure. In conclusion, eigenvalue analysis gives a different result of these two models, and DLM shows a stiffer behavior. The shell-like vibration is sensitive to the modification of the geometry of the stiffening rings because the stiffness of the stiffening rings gives a direct impact on deformation capacity of the tower cross-section.

5.4.2. Linear static analysis

The linear static analysis will be conducted for the comparison between DLM and SLM.

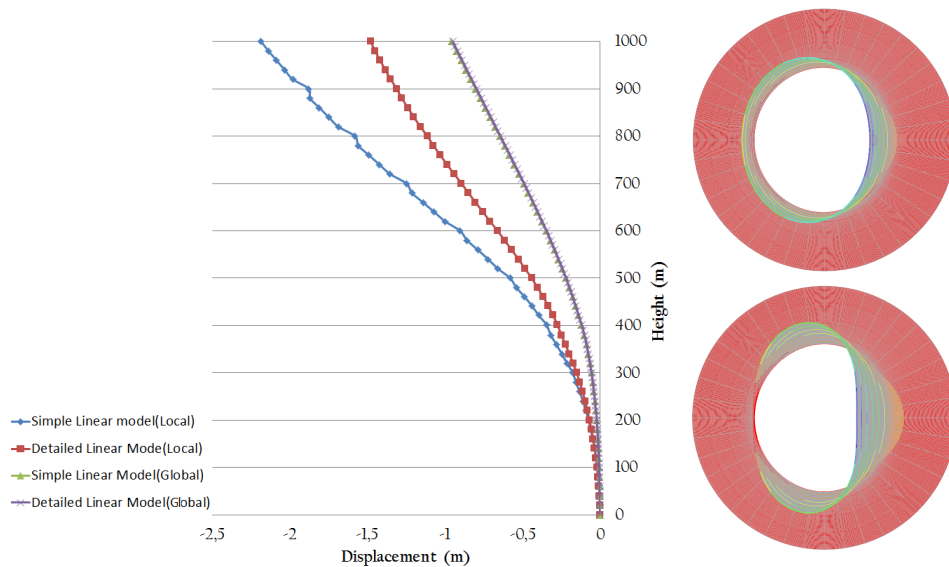


Figure 5.8: Global and local displacement of Simple Linear Model and Detailed Linear Model (left) and top view of deformed tower for Simple Linear Model and Detailed Linear Model (right) (1D+1,5W)

Displacement

Figure 5.8 shows the global displacement and the local displacement on the windward direction of the SUT. The global displacement was calculated by averaging the displacement of every node on the same level. It shows the deformation of the center line of the tower. The local displacement is the displacement on the shell walls located at the center of the tower in the windward side. Comparing the global displacement of these two models, it is observed that two structures deformed almost identical, both in shape of the curve and magnitude. The maximum displacements at the top are 0.958m and 0.95m for DLM and SLM respectively. Therefore, the changing of the configuration of the stiffening rings has a small influence on global behavior.

It is not the case for the local displacement. These two models have similar local displacement up to the height of 300m. However, SLM starts to deform more when it is higher than 300m. The maximum displacement at the top of the tower for SLM and DLM is 2.18m and 1.47m respectively, and a 40% of difference is observed. Simple Linear Model has slight deformation fluctuations at the location near the stiffening rings because the eccentricity of the stiffening rings gives a bending moment on the wall.

The right-hand-side of the Figure 5.8 shows the top view of a deformed tower for both models. The deformed shape of the top cone changed from circular shape to an ellipsoid shape. The stiffness of the cross-section is lower which leads to a larger ovalizing deformation of the upper cone and it might cause large cracks and decreased material strengths and a weak the global structural stiffness in the physical nonlinear analysis.

In-plane forces

This section shows the distribution of meridional stress-resultant both over the height of the tower on the windward side (left) and over the circumference direction(right) (Figure 5.9). It can be seen that in Detailed Linear Model, the in-plane forces is under compression, while for Simple Linear Model, the large ovalization leads to the tensile force occurred at the throat height. It is because the weak stiffness of the stiffening ring at the top cone in SLM. The right-hand side of Figure 5.9 gives the meridional stress resultant distribution at the throat height. DLM has a more linear distribution compared to

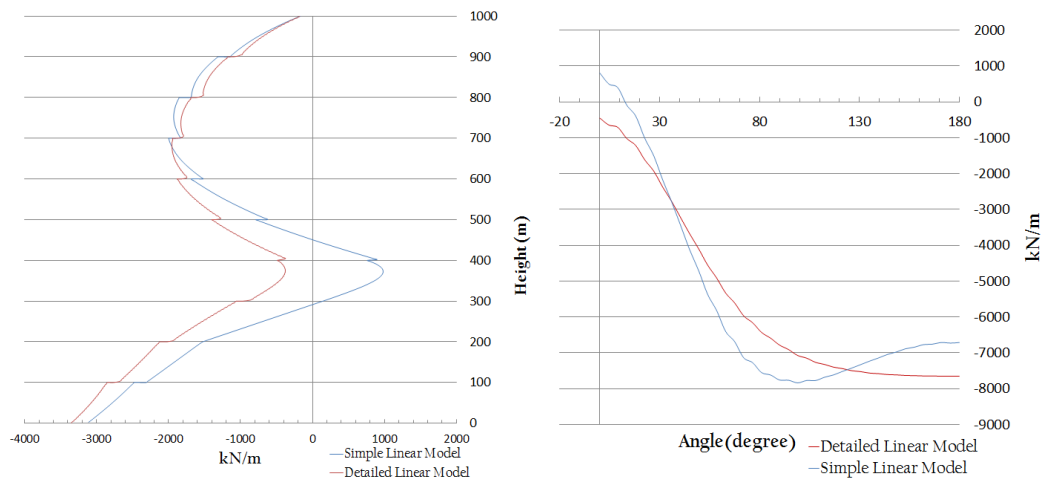


Figure 5.9: In-plane meridional stress resultant distribution over height of Simple Linear Model and Detailed Linear Model (left) and In-plane meridional stress resultant distribution at throat height over the circumference (right) (1D+1.5W)

SLM, which is a beam-like distribution shape. SLM has a more shell-like distribution shape with large variations. Furthermore, the stress-resultant for DLM is under compression over the entire circumference but SLM gives tensile forces on the windward side.

Conclusion

Detailed Linear Model and Simple Linear Model have rather big differences in structural response both in the dynamic analysis and the static analysis. If the nonlinear analysis is performed, due to the cracking of concrete and yielding of the reinforcement, these differences will be enlarged. If Simple Linear Model is used, the structure will be underestimated, and unnecessary amount of reinforcement will be used. As a conclusion, for the following research, Detailed Linear Model is chosen to yield a real structural behavior.

5.5. Conclusions

As a result, the eigenvalue analysis and static analysis show sufficient accuracy on model setup. The necessity of a more detailed model has been demonstrated. Between DLM and SLM, it is shown that the detailed model has stiffer behavior than SLM in general. The configuration of the stiffening rings has the impact on the local deformation of the upper cone and has a less impact on the global behavior. Finally, another vital advantage of choosing DLM for material nonlinear analysis is that the reinforcement layout can be modeled in detail. The material non-linearity will be presented and discussed in the next chapter. Material models and crack mechanisms adopted in this research will be explained.

6

Nonlinear Material Models

This chapter demonstrates the material models that have been used for the nonlinear analysis along with their basic background theory. The Concrete cracking, tensile, and compressive behavior will be discussed and then the reinforcement model and its stress-strain curve will also be defined.

6.1. Introduction

Physical non-linear analysis is capable of representing the real behavior of a large-scale SUT under the complicated wind action. However, the material models assigned to each element of finite element model can be tricky, particularly for reinforced concrete. For concrete, DIANA offers a broad range of physical models for both the tensile cracking and the compressive plasticity behavior. For the reinforcement, the material can be modeled by an elastoplastic model with hardening behavior. The interaction between concrete and reinforcement is a crucial aspect for determining the ductility of the reinforced concrete. Additionally, the physical behavior also highly depends on the stress state and cracking state. Lateral confinement and lateral cracking can both alter concrete compressive performance, which will also be included.

6.2. Concrete model

This section is organized as follows. Firstly, a brief theoretical explanation of the total strain rotating smeared crack concept will be given. The same is done for the fixed and the multi-directional fixed crack model in the Appendix A. The syntax of the input for the rotating smeared crack model will be explained. Next, the concrete tensile and compressive behavior will be illustrated.

- **Concrete cracking behavior** relates to the cracking and the failure mechanism of concrete in tension.
- **Tensile behavior** refers to the physical response to tension, mainly about the tensile cracking.
- **Compressive behavior** describes the compressive behavior of concrete. The effects of lateral confinement and the lateral cracking will be attached to the compression model.

6.2.1. Concrete cracking behavior

Smeared crack and Discrete crack

There are many numerical ways of modeling concrete cracking behavior. Typically they can be divided into two categories, the smeared and the discrete crack models. This research intends to analyze the

structural behavior of a large-scale shell structure under a complex loading conditions, the distribution of crack is concealed. However, in the discrete crack model, the location and the number of cracks are predefined by interface elements, which does not suit for the research purpose. For the smeared crack models, the crack solid is a continuum material defined by stress-strain relations. As a result, the geometrical discontinuity in FEM vanishes. In some cases, the crack can rotate according to the principal stress state.

Fixed, multi-directional, rotating smeared crack

Of the several smeared crack models available, a choice has to be made. Three models are available in DIANA: the fixed, the multi-directional and the rotating smeared crack model. Their differences depend on the orientation of the crack: fixed, stepwise and updated continuously respectively (J.G (1988)). Particular attention should be given if the structure under the multi-stress state. For example, in a tension and shear loading condition, the principal stress tends to rotate, or new crack tends to occur at the same sample point. In a fixed crack model, and an over stiff behavior will be observed (Willam et al. 1987, Kolleger and Mehlhorn 1987, Rots and de Borst 1987, Crisfield and Wills 1989). A fixed crack model would not be the proper choice for modeling structural under multi-direction loading conditions.

In the multi-directional fixed crack model, the total strain is decomposed into the strain of the solid material and the strain of the crack. This decomposition allows the plastic behavior and other nonlinear material properties such as concrete aging, creep, and shrinkage to be assigned to the solid material. The crack strain is decomposed into the separate contributions from a number of multi-directional cracks. When the angle of inclination of existing cracks and the current direction of principal stress exceeds a certain threshold, a new crack will be initiated (J.G Rots (1989)). The initiation of new crack and existing crack interact with each other, for instance, a new crack might cause closure of an existing crack. Since the cracks are fixed, the shear retention function to interpreting shear softening behavior resulting from aggregate interlock should be assigned. Even with shear retention function, an over stiff structural behavior can still be found (J.G Rots (1989)). The multi-directional fixed crack model has mechanisms that are capable of modeling concrete time-dependent behavior which unnecessarily complicates the analysis. Convergence issue arises when the rotation of the principal stress is large (J.G Rots (1989)).

Another model is the total strain rotating crack model for which the crack is rotating continuously with the direction of the principal stresses. It has a averaged stress-averaged strain relation without strain decomposition. The co-axially of the principal stress and strain makes the system more stable. The working principle is straightforward because no threshold angle is defined. Shear retention function is unnecessary to be defined manually because the shear softening behavior is introduced implicitly by co-axially theory.

This research project conducts the static analysis of a large-scale curved reinforced concrete shell structure under the complex wind action. Time-dependent material behavior is not of interest. Therefore, the strain decomposition is not necessary. Instead, a robust model with simple working principle such as the total strain rotating smeared model is most appropriate for this research by considering that the model has a complex loading condition, a large structural size, a complex geometry. Since the crack is always with the same direction as the principal stress, the uncontrollable principal stress direction is no longer a concern for the rotating model. The over-stiff behavior is minimized because the shear softening behavior is one of the attributes of the rotating model. Based on this overview of the current valid smeared crack models, the total strain rotating crack model will be applied in this research.

Theory of smeared rotating crack

Consider a concrete solid under tension. When the tensile stress exceeds the tensile strength, the crack is initiated. The isotropic elastic law turns to the orthotropic law, and the principal axis of orthotropy is referred to the direction of the crack. The key concept of the rotating smeared crack is the

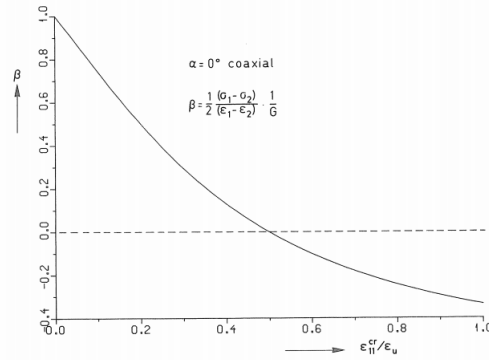


Figure 6.1: Development of equivalent shear retention factor for coaxial rotating crack result (J.G (1988))

co-rotating among material orthotropy, the axis of principal strain and the axis of principal stress. The strain in the global coordinate system is converted into the crack direction by the strain matrix N . The matrix depends on the current strain vector.

Assume a 2D configuration, a small increment of strain causes a slight rotation of the axis of the principal strain. The angle is $\Delta\theta_\epsilon$. From Mohr's circle, the following equation can be obtained.

$$\tan 2\Delta\theta_\epsilon = \frac{\Delta\gamma_{12}}{2(\epsilon_{11} - \epsilon_{22})}$$

The Same theory works for principal stress, a small increment of stress gives a rotation of the axis of principal stress. The angle is $\Delta\theta_\sigma$. From Mohr's circle, the following equation can be found.

$$\tan 2\Delta\theta_\sigma = \frac{\Delta\sigma_{12}}{2(\sigma_{11} - \sigma_{22})}$$

In order to achieve the coaxiality of the principal strain and the principal stress, these two angles have to equal to each other. This condition is satisfied only if the tangential shear modulus equal to the following:

$$G_{12} = \frac{(\sigma_{11} - \sigma_{22})}{2(\epsilon_{11} - \epsilon_{22})}$$

For a linearized tangential stress-strain law, the rotating smeared crack concept is

$$\begin{bmatrix} \Delta\sigma_{11} \\ \Delta\sigma_{22} \\ \Delta\sigma_{33} \\ \Delta\sigma_{12} \\ \Delta\sigma_{23} \\ \Delta\sigma_{31} \end{bmatrix} = \begin{bmatrix} \frac{\partial\sigma_{11}}{\partial\epsilon_{11}} & \frac{\partial\sigma_{11}}{\partial\epsilon_{22}} & \frac{\partial\sigma_{11}}{\partial\epsilon_{33}} & 0 & 0 & 0 \\ \frac{\partial\sigma_{22}}{\partial\epsilon_{11}} & \frac{\partial\sigma_{22}}{\partial\epsilon_{22}} & \frac{\partial\sigma_{22}}{\partial\epsilon_{33}} & 0 & 0 & 0 \\ \frac{\partial\sigma_{33}}{\partial\epsilon_{11}} & \frac{\partial\sigma_{33}}{\partial\epsilon_{22}} & \frac{\partial\sigma_{33}}{\partial\epsilon_{33}} & 0 & 0 & 0 \\ 0 & 0 & 0 & \frac{(\sigma_{11} - \sigma_{22})}{2(\epsilon_{11} - \epsilon_{22})} & 0 & 0 \\ 0 & 0 & 0 & 0 & \frac{(\sigma_{22} - \sigma_{33})}{2(\epsilon_{22} - \epsilon_{33})} & 0 \\ 0 & 0 & 0 & 0 & 0 & \frac{(\sigma_{33} - \sigma_{11})}{2(\epsilon_{33} - \epsilon_{11})} \end{bmatrix} \begin{bmatrix} \Delta\epsilon_{11} \\ \Delta\epsilon_{22} \\ \Delta\epsilon_{33} \\ \Delta\epsilon_{12} \\ \Delta\epsilon_{23} \\ \Delta\epsilon_{31} \end{bmatrix}$$

Multiple rotating cracks are possible if the material is in multi-axial tension, which is mutually orthogonal since they all follow with the principal strain.

Figure 6.1 shows the equivalent shear retention factor. After the crack initiation, the shear retention factor decreases gradually to zero, which gives a more flexible and robust structure response.

$$\beta G = \frac{(\sigma_{11} - \sigma_{22})}{2(\varepsilon_{11} - \varepsilon_{22})} \quad (6.1)$$

where

βG	overall shear stiffness
β	equivalent shear retention factor
G	elastic shear modulus

6.2.2. Tension behavior

Uni-axial Tension

Concrete is usually not designed for resisting the direct tension. The tension capacity is only 10% of its compression capacity. However, concrete in tension can occur when concrete is under bending, shrinkage and temperature differences. It was found that concrete behave brittle under tension with failure strain around 0.0001-0.0002. The stress-strain relation of concrete in tension is usually based on the tensile strength and fracture energy. DIANA offers different types of the tension softening diagrams. These diagrams illustrate a single concrete cracking behavior within a certain crack bandwidth. The crack bandwidth is a material attribute, and it is also a function of element size. For this research, with reinforced concrete element size of 5m, it would be difficult to define a particular crack bandwidth.

Tension stiffening

For reinforced concrete behavior under bending, the cracks reduce its bending stiffness, because the tensile contribution of concrete below neutral axis vanished. However, the solid concrete between cracks can still carry tensile stress due to the bond between reinforcing bar and surrounding concrete. If the tension stiffening effect is omitted, the deflection of the structure, as well as the crack width, will be overestimated. Bonding behavior plays an important role on tension stiffening effect. The bond consists of three main components: the chemical adhesion, the friction, and the mechanical interlock. The chemical adhesion has a small effect, and it vanishes when slip occurs. The friction force can counteract the slip. Ribs on the bar create the mechanical interlock, and it generates the main pullout resistance. Figure 6.2 gives the formation of the secondary internal cracks due to the bonding between primary cracks. The bonding capacity decided the stress state of concrete just after crack initiation. A stronger bonding yields a highly stressed surrounding concrete which gives a faster crack developing and less tension stiffening effect.

In reality, the tension stiffening is limited at a particular area that closes to reinforcing bar, which is named as the tension stiffening zone. The area outside tension stiffening zone is called the tension softening zone. For the numerical modeling, the softening and the tension stiffening are combined into one stress-strain relationship, which is called *tension-stiffening*. The averaged stress-averaged strain method to predict the cracking and the deformation is used in this research project. Concrete has one stress-strain relationship over the whole area that is under tension. The tension stiffening effect will be incorporated by modeling the concrete tensile behavior.

The tension-stiffening curve is driven by the experimental data, and it was observed that it highly depends on the concrete tensile strength and the reinforcement ratio. Figure 6.3 gives the load-deformation behavior of a tension member. As shown in Figure 6.3, the cracking behavior of the tensile member can be divided into three stages. Upon loading, the first stage is the uncracked stage. The reinforcing bars fully bond with concrete and behave linearly. With the increase of tensile load, the first primary crack is initiated at the weak point of the material, then, the element steps into a multiple cracking

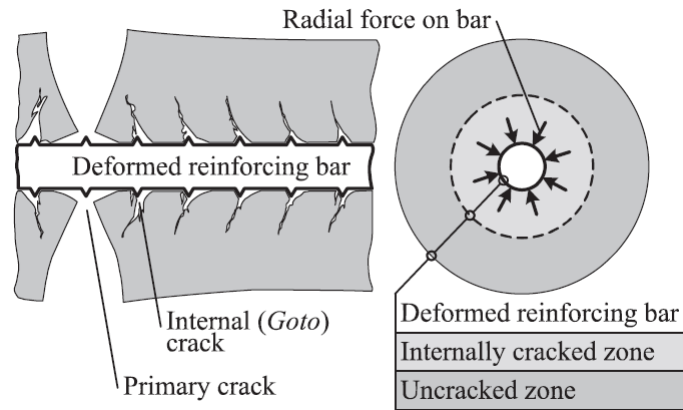


Figure 6.2: The formation of secondary crack (Goto.Y. (1971))

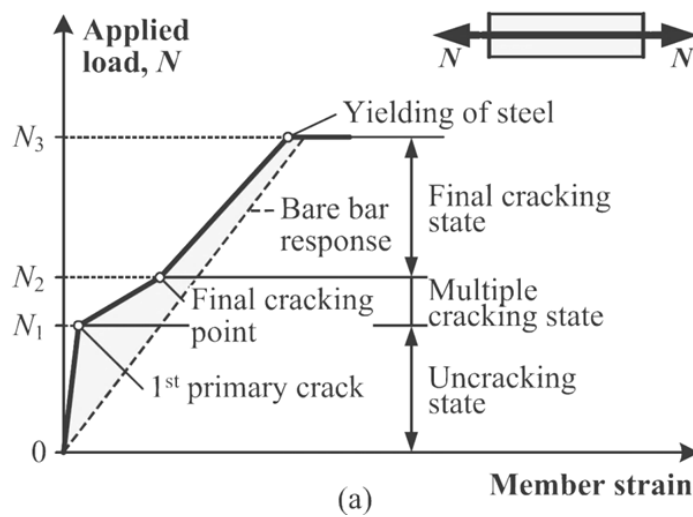


Figure 6.3: Stages of load-deformation behavior of a reinforced concrete tensile member (Goto.Y. (1971))

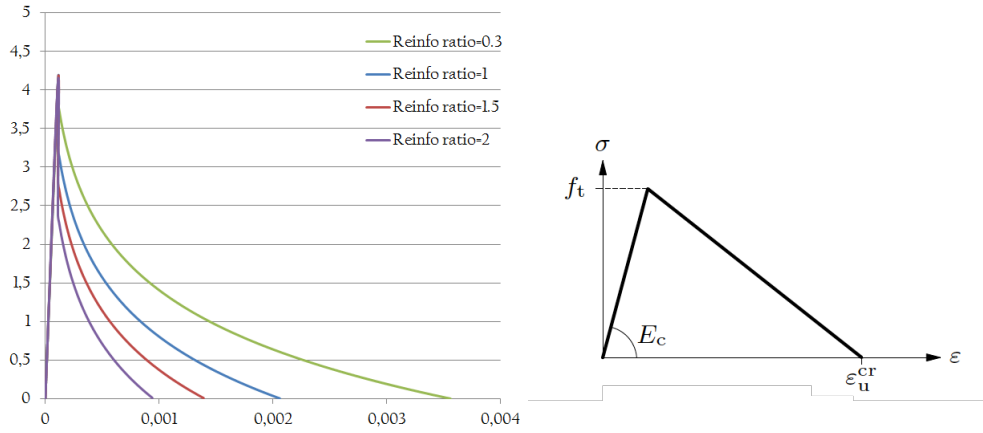


Figure 6.4: The tension stiffening curve with varying reinforcement ratios(left) Stress-strain relationship of concrete in tension(right)

stage. Without further increasing of the crack width, more cracks are initiated until the last one. Ultimately, in the final cracking stage, without new crack formation, the cracks width keeps increasing until the member failed. In Figure 6.3, the gray area shows the contribution of concrete to the tensile member including the tension stiffening effect.

Sokolov (2010) derived the tension-stiffening law using free-of shrinkage tension stiffening relationship. The tension stiffening model has the form: For $\varepsilon_{ct} \leq \varepsilon_{ct,EC2}$

$$\sigma_{ct} = E_c \varepsilon_{ct} \quad (6.2)$$

For $\varepsilon_{ct} \geq \varepsilon_{ct,EC2}$

$$\sigma_{ct} = f_{t,EC2} \left(1 - 0.27 \ln \left(\frac{\varepsilon_{ct}}{\varepsilon_{ct,EC} - 0.21p} \right) \right) \quad (6.3)$$

where

E_c	modulus of elasticity of concrete
$f_{t,EC2}$	tensile strength of concrete according to EN1992-1-1 (2011)
$\varepsilon_{ct,EC2}$	concrete cracking strain
p	reinforcement ratio

The graph on the left in Figure 7.16 shows the tension-stiffening curve with increasing reinforcement ratios. In comparison, the tension-stiffening effect decreases with the increase of reinforcement ratios, as the larger reinforcement ratio means more reinforcement with larger steel bars and rib size. This gives a larger contact area with surrounding concrete and stronger bonding. A relatively higher bond force is expected which leads to a faster cracking in concrete. While for the RC member with a smaller reinforcement ratio, a larger area of pure concrete less stressed is contributing to bear tensile force after crack initiation. However, it gives a lower tensile capacity and a lower bond force. With lower bond forces, the reinforcement might be pulled out before crack initiation.

For finite element modeling, an ultimate strain tension stiffening model will be utilized. It has a linear descending branch after the tension strength is reached. The tensile strength and the ultimate strain are the nonlinear material inputs. The ultimate strain is computed by integrating the equation 6.1 and 6.2 and the area under the ultimate strain curve will be the same as the tension-stiffening curve. The right-hand-side of Figure 7.16 is the ultimate strain curve of concrete in tension.

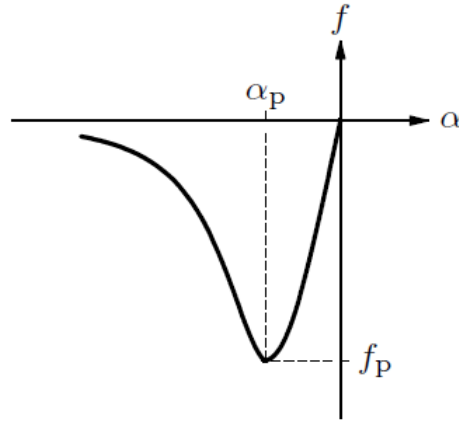


Figure 6.5: Thorenfeldt curve for concrete compressive behavior (DIANA (2016))

$$\epsilon_u^{cr} = \frac{\int f_{t,EC2} (1 - 0.27 \ln(\frac{\epsilon_{ct}}{\epsilon_{ct,EC} - 0.21p})) d\epsilon_{ct}}{2 * f_{t,EC2}} + \frac{f_{t,EC2}}{E_c} \quad (6.4)$$

6.2.3. Compressive behavior

Concrete in compression gives a pressure-dependent behavior. The effect of concrete compressive behavior on whole structural performance should be taken into account when the structure is under the multi-stressed stage. Owing to the circular hollow cross-section of the tower, lateral confinement should be taken into account. For the solar updraft tower under the static self-weight and the wind action, the cracking is presumed, which might reduce the concrete compressive strength and the ductility. In this section, a concrete compressive curve will be defined. The lateral confinement and lateral cracking will be considered.

Concrete compressive curve

For the smeared rotational crack model, DIANA provides four nonlinear compressive curves. One is a parabola determined by the compressive strength and the concrete compressive fracture energy. With concrete models related to fracture energy, the compressive behavior highly depends on the element size. According to the model function, it was observed that the larger the element size is, the more brittle the compressive behavior becomes, which would be unrealistic without experimental data. The compressive behavior will be underestimated. This model is not recommended for this research. The Hognestad Parabola and the curve according to Eurocode 2 EN 1992 are not capable of taking lateral confinement into consideration. These two models will not be adopted. The Thorenfeldt curve is a function of compressive strength only. It gives best correlations from low to a high strength concrete. Additionally, the lateral confinement can be taken into account in this model. The Thorenfeldt model should be utilized in this research. The formula of the Thorenfeldt curve is shown below:

$$f = -f_p \frac{n(\frac{-\epsilon}{\epsilon_p})}{(n-1) + (\frac{-\epsilon}{\epsilon_p})^{nk}} \quad (6.5)$$

$$n = 0.80 + \frac{f_p (MPa)}{17} \quad (6.6)$$

For $-\varepsilon_p < \varepsilon < 0$

$$k = 1.0; \quad (6.7)$$

For $\varepsilon_2 < -\varepsilon_p$

$$k = 0.67 + \frac{f_p(MPa)}{62}; \quad (6.8)$$

where

- f compressive stress
- f_p concrete compressive peak stress
- ε concrete compressive strain
- ε_p concrete compressive strain at peak stress

The stress-strain relationship is shown in Figure 6.5

Lateral cracking

It was observed that the lateral cracking of reinforced concrete could significantly decrease concrete strength and ductility. The degree of the reduction is essential for accurately modeling cracked reinforced concrete. Vecchio and M.P. Collins (1994) did a comprehensive study on the impact of lateral cracking on compressive behavior at different loading conditions. The strength softening model is presented on the right-hand-side of Figure 6.6. DIANA provides the softening function proposed by Vecchio and M.P. Collins (1994). The reduction factor of compressive stress is a function of average lateral damage variables. The curve of lateral cracking reduction factor is shown in the left-hand-side of Figure 6.6 The formula is shown below,

$$\beta = \frac{1}{1 + K_c} \quad (6.9)$$

$$K_c = 0.27 \left(-\frac{\alpha_{lat}}{\varepsilon_0} - 0.37 \right) \quad (6.10)$$

$$\alpha_{lat} = \sqrt{\alpha_{l,1}^2 + \alpha_{l,2}^2} \quad (6.11)$$

where

$\alpha_{l,1}$ and $\alpha_{l,2}$ tensile damage in the lateral direction

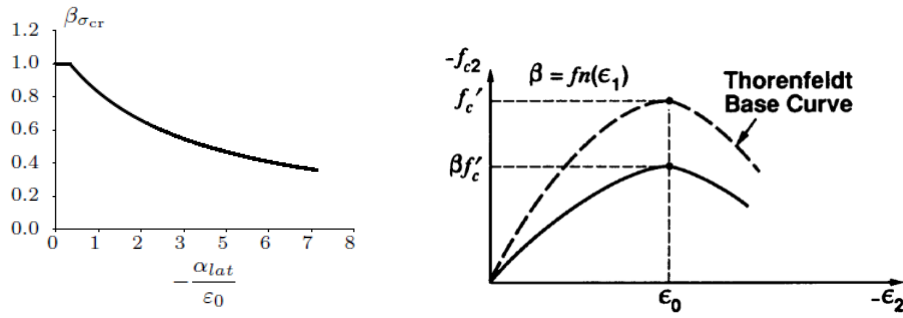


Figure 6.6: The reduction factor by lateral crack(left) The stress-strain compressive curve for concrete after the lateral crack is taken into account(right) (DIANA (2016))

Lateral confinement

The tower has a circular hollow cross-section, this creates the confining pressure in the circumferential direction by the self-weight. This lateral pressure can increase the concrete ductility and strength in compression. The left one in Figure 6.7 shows the influence of lateral confinement on the compressive stress-strain curve. To take lateral confinement into account, DIANA gives the peak strain factor to determine the compressive stress-strain function. It is based on the Hsieh-Ting-Chen four parameter criterion which is defined as following:

$$f = 2.0108 \frac{J_2}{f_{cc}^2} + 0.9714 \frac{\sqrt{J_2}}{f_{cc}} + 9.1412 \frac{f_{c1}}{f_{cc}} + 0.2312 \frac{I_1}{f_{cc}} - 1 = 0 \quad (6.12)$$

where J_2 is the second deviatoric stress invariant

$$J_2 = \frac{1}{6} ((\sigma_{c1} - \sigma_{c2})^2 + (\sigma_{c2} - \sigma_{c3})^2 + (\sigma_{c3} - \sigma_{c1})^2) \quad (6.13)$$

I_1 is the hydrostatic stress invariant

$$I_1 = \sigma_{c1} + \sigma_{c2} + \sigma_{c3} \quad (6.14)$$

f_{c1} is the maximum concrete principal stress.

$$f_{c1} = \max(\sigma_{c1}; \sigma_{c2}; \sigma_{c3}) \quad (6.15)$$

The four parameter is empirically determined by analyzing uni-axial tensile and compressive strength, bi-axial compressive and tri-axial tests on concrete (DIANA (2016)).

Then the failure criteria are determined by stress f_{c3} which is a function of scale factor s . The scale factor is computed from the linear elastic principal stress vector that holds in equation 6.11.

$$s = \frac{\sigma_c}{E \epsilon_{nst}} \quad (6.16)$$

Then the f_{c3} can be determined

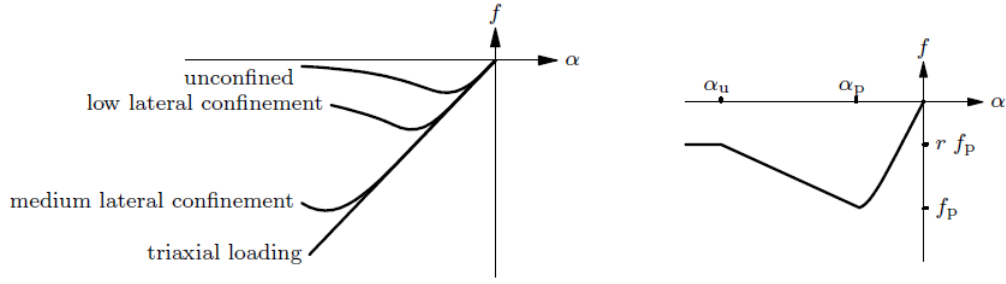


Figure 6.7: Influence of lateral confinement on compressive stress-strain curve(left); Compressive behavior under lateral confinement (right) (DIANA (2016))

$$f_{c3} = s \cdot \min(\sigma_{c1}; \sigma_{c2}; \sigma_{c3}) \quad (6.17)$$

The failure criteria is

$$f_{cf} = -f_{c3} \quad (6.18)$$

The peak stress factor can be determined. DIANA assumes that the peak strain factor is equal to peak stress factor.

$$K_\sigma = \frac{f_{cf}}{f_{cc}} \geq 1 \quad (6.19)$$

For the Thorenfeldt curve, the strain at the peak stress is defined by the following

$$\varepsilon_p = K_\sigma \varepsilon_0 \quad (6.20)$$

where the initial strain at the peak stress is given by

$$\varepsilon_0 = -\frac{n}{n-1} \times \frac{f_{cc}}{E} \quad (6.21)$$

For the descending branch of the Thorenfeldt curve, it is assumed that the ductility increases with the increase of lateral confinement. DIANA adopts a linear descending branch:

$$f_j = -f_p \left(1 - (1-r) \frac{\alpha_j - \alpha_p}{\alpha_u - \alpha_p}\right) \quad (6.22)$$

where the strain at peak is defined by

$$\alpha = \left(\frac{f_p}{f_{cc}}\right)^\gamma \alpha_p \quad (6.23)$$

with γ is equal to 3

With the residual strength $r f_p$ defined by

$$r = \left(\frac{f_p}{f_{cc}}\right)^\gamma r_0 \quad (6.24)$$

with r_0 is equal to 0.1.

The compressive behavior under lateral confinement in DIANA for the Thorenfeldt curve is shown in Figure 6.7 (right). In DIANA, if the ratio $\frac{f_p}{f_{cc}} > 1.05$, the linear compression-softening relation will be taken into account, and if $\frac{f_p}{f_{cc}} < 1.05$, the increase of ductility will not be considered.

6.3. Reinforcing steel

DIANA offers two main categories for modeling the reinforcement. One is the embedded reinforcement that the reinforcement is fully bonded to concrete; the other is bond-slip reinforcement that a reinforcement, a concrete and a bond-slip iteration between bar and concrete are modeled. The bond-slip reinforcement is more used in analysis the concrete and reinforcement interactions in a small structure size. Bond-slip reinforcement is only available for using line elements in regular plane stress, curved shell, or solid element with linear or quadratic interpolation function (DIANA (2016)). For a model with 1000 meter high with reinforcement in two directions on the whole structure, a significant amount of modeling effort is demanded. A lengthy calculation time is needed because of the complex nonlinear models for concrete, the reinforcement, and the bond-slip interaction. For embedded reinforcement, a plane-shaped reinforcement grid can be embedded in the curved shell element. There is no relative movement between concrete and reinforcement, which indicate no the bond-slip model need to be assigned. Instead of modeling bond-slip interaction, the bonding is considered in the concrete tensile model by tension stiffening.

For embedded element, DIANA offers three types of material model, linear elasticity, uni-axial nonlinear elasticity and Von Mises plasticity. Nonlinear structural analysis requires a realistic steel material behavior. Wind action on the SUT might result in the yielding of reinforcing bar. The von Mises is applicable for reinforcement response beyond yielding. A plastic deformation of reinforcing bar can be achieved by using von Mises criteria.

The reinforcement grid is modeled in two directions separately, and their stress state is independent of each other. The directions of stress σ_{xx} and σ_{yy} are considered. For axial tension or compression, the von Mises criterion simply reduced to

$$\sigma_{xx} = \sigma_y \quad (6.25)$$

$$\sigma_{yy} = \sigma_y \quad (6.26)$$

The stress-strain relation for reinforcing bar is shown in Figure 6.8

6.4. Conclusions

In this chapter, the background theory of the material non-linearities has been explained. The concrete cracking model has been presented. A total strain rotating smeared crack model is chosen. Next, tensile behavior including tension stiffening effect of concrete has been displayed. The tension stiffening behavior is a function of tensile strength and reinforcement ratio. Furthermore, a concrete compressive behavior is realized using a Thorenfeldt curve. The lateral cracking and the lateral confine-

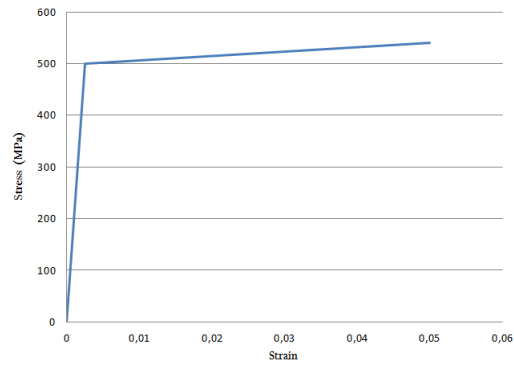


Figure 6.8: Stress-strain relation for reinforcement bar

ment are considered. Lastly, the steel isotropic plasticity with a hardening behavior has been introduced by using von Mises yielding criterion. With the explanations of different material nonlinear models, a firm foundation for the following physical nonlinear analysis has been obtained.

In the next chapter, a nonlinear analysis is executed. Several analysis results are shown. Having gained inside in various material nonlinear properties, an analysis of structural response will be given.

7

Material nonlinear analysis

The linear analysis from Chapter 5 has been extended to the physical nonlinear analysis in this chapter. It starts with the nonlinear model setup together with its iteration method. Later, three models are built. The nonlinear analysis is done for evaluating the realistic structural behavior under the static wind load. Three nonlinear models are compared and a comparison between linear and nonlinear structural responses is also given.

7.1. Introduction

The aim of the detailed material nonlinear analysis is to understand how this unbuilt tower behaves under the wind action in reality. The biggest challenge is to conduct this nonlinear analysis with the inclusion of details that would generate a reasonable result. The reinforcement in the concrete wall and the stiffening rings are modeled. The choices of the reinforcement element types highly depend on the types of its mother elements. Three models are built with different element types for modeling the stiffening rings and its reinforcement. Their definitions show below.

- *Beam Nonlinear Model (BNM)*. Beam Nonlinear Model has a geometry similar to Detailed Linear Model. The only difference is that the reinforcement is added. The reinforcement grid element is embedded in the shell element and the reinforcing bar is embedded in the beam element.
- *Shell no Transverse Nonlinear Model (STNM)*. Shell no Transverse Nonlinear Model is similar to BNM. However, in STNM, the stiffening rings are built by the curved shell element and the reinforcement grid is embedded in the rings only in circumferential direction.
- *Shell Nonlinear Model (SNM)* Shell Nonlinear Model is almost the same as STNM. However, its reinforcement in the stiffening rings is modeled both in the circumferential and the transverse directions.

7.2. Model setup

In this section, the detailed model setup and design choices will be described briefly. For all models, their geometry, the element types of the shell walls, meshing density, and boundary conditions are identical to the Detailed Linear model. Their concrete properties are shown in Table 7.1 and the reinforcement properties are shown in Table 7.2.

For BNM and SNM, the reinforcement grid used for the concrete shell wall is the minimum percentage of reinforcement according to VGB Guideline (VGB-R-610E2010 (2010)). The reinforcement ratios for shell wall in two directions are shown in Table 7.3

Table 7.1: Concrete material properties for nonlinear analysis

Linear properties	Material type	Concrete
	Smearred crack model	Total strain based crack
	Young's modulus	$37000N/mm^2$
	Poisson's ratio	0.2
	Mass density	$2500kg/m^3/g$
Crack model	Crack rotaton	Rotation
	Crack bandwidth	
Tensile behavior	Tensile model	Linear-ultimate crack strain
	Tensile strength	$4.1N/mm^2$
	Ultimate strain	Undetermined
	Residual tensile strength	$0N/mm^2$
	Reduction by lateral cracking	Vecchio and Collins 1993
	Poisson's ratio reduction	No reduction
Compressive behavior	Compressive curve	Thorenfeldt Curve
	Compressive strength	$58N/mm^2$
	Lateral confinement	Selby and Vecchio

Table 7.2: Reinforcement material properties for nonlinear analysis

Material	Steel
Material model	Von Mises plasticity
Young's modulus	$200000N/mm^2$
Yield stress	$500N/mm^2$

Table 7.3: Reinforcement ratio setup for the shell walls

Reinforcement ratio for the shell wall		
	Meridional direction	Cricumferential direction
Lower half	0.3%	0.3%
Upper half	0.3%	0.4%

Table 7.4: Reinforcement setup for stiffening rings

Reinforcement ratio of stiffening ring			
Model type	Physical Nonlinear model		
Stiffening ring	Beam model	Shell without transverse	Shell model
Mother Element	3D Beam element	Curved shell element	Curved shell element
Reinforcement	Bar	Grid	Grid
Longitudinal ρ	1%	1%	1%
Transverse ρ	0%	0%	1%

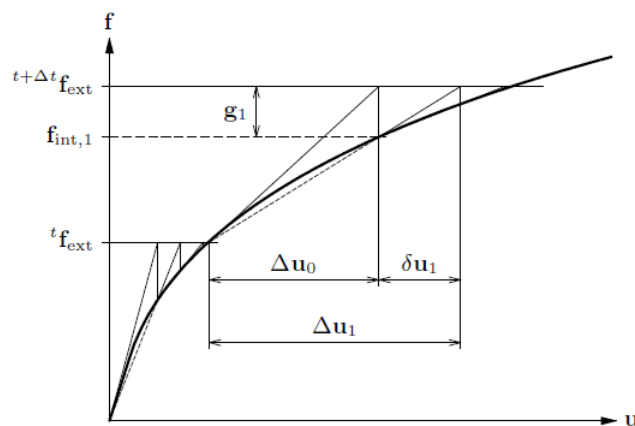


Figure 7.1: Modified Newton-Raphson iteration (DIANA (2016))

7.3. Nonlinear analysis

This section specifies the nonlinear analysis setup. A solver and an iteration method will be chosen for this specific nonlinear analysis.

7.3.1. Solution method

The Parallel Direct Sparse solver is adopted in this research project. The model is mainly built by the curved shell element. According to DIANA guideline, the Parallel Direct Sparse is the proper solver and it can handle the different order of contributions from rotations and translations to the stiffness matrix efficiently (DIANA (2016)).

7.3.2. Iteration method

In linear analysis, the equilibrium between internal and external forces can be calculated directly. However, considering a nonlinear analysis, the balance depending on previous constitutive properties is calculated at every displacement increment. To achieve this equilibrium, an iterative method is prescribed. The total displacement is equal to the sum of the iterative displacement increments. Different iterative methods are given in DIANA.

In Regular Newton-Raphson iterative method, the stiffness matrix is calculated at every iteration. The governing parameters are the displacement, the internal force vectors and the stiffness matrix. In this are, divergence can easily happen if the accuracy of stiffness matrix is not guaranteed. Modified Newton-Raphson calculates the stiffness matrix only at the start of the increment, so it is more stable compared to Regular Newton-Raphson. However, it requires more iterations which mean a longer time to achieve convergence. DIANA also gives Quasi-Newton-Raphson iteration method. Figure 7.1 shows the force-displacement diagram for this method. As can be seen from the figure, the stiffness is determined by the previously known position at its equilibrium path. Since this method is not completely stiffness-dependent, the accuracy of stiffness matrix plays a minor role in convergence. By this method, the stiffness matrix is always positive so that no snap-back occurs in the load-displacement curve. Thus the Quasi-New-Raphson method is more stable compared to Regular Newton-Raphson Method. Additionally, because the stiffness matrix is changing and is close to secant stiffness at next equilibrium point, it has a relatively faster convergence time and fewer iterations to converge compared to Modified Newton-Raphson. In conclusion, the Quasi-Newton-Raphson iteration method will be adopted for all nonlinear models.

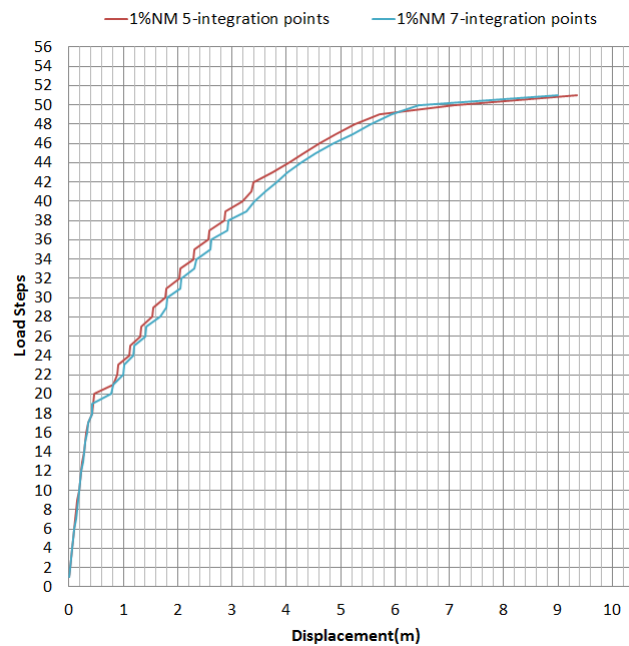


Figure 7.2: Load steps-displacement curve for 1%NM integration scheme of 5-points Simpson and 7-points Simpson in thickness direction

7.3.3. Integration scheme for nonlinear analysis

In the nonlinear analysis, over the shell surface area, the integration scheme keeps 2x2 Gauss scheme, while in the thickness direction, 5 points Simpson integration scheme is adopted. In shell thickness direction, a higher integration scheme reveals a more precise nonlinear result. However, it takes a longer calculation time. The structure experiences divergence when the 3-point Simpson integration scheme is used in nonlinear analysis. A 5 points integration scheme gives an easy convergence until the last load step for all nonlinear models. When the structure is experiencing extensive material nonlinearity, an integration scheme higher than 5-points should be used. Models with Simpson 5-point and 7-point integration scheme were built and their nonlinear analysis was made. Figure 7.2 shows the load steps-displacement curve of these two models. Two curves are similar, with average differences of 6% in displacements, but 5-points gives a much less calculation time. The 5-points integration scheme will be used for all nonlinear analysis.

Convergence Criteria

Convergence Criteria specifies the time that the iteration should stop. The iteration process will stop in the following three conditions:

- The convergence criteria is reached.
- The iteration reached the maximum number.
- The divergence occurs during iteration.

DIANA provides several convergence criteria.

- **Force norm criteria** is to check the force norm after the current iteration against the force norm of the initial unbalances(DIANA (2016)).
- **Displacement norm criteria** is to check the current iterative displacement increment against displacement increments in the first prediction. (DIANA (2016)).

- **Energy norm criteria** The energy norm consists of both internal forces and relative displacement. The energy ratio is the ratio between the energy norm in the current iteration and the initial energy norm (DIANA (2016))

The energy norm may be a good choice if the following analysis type is used by:

- The displacement is prescribed in the model which makes the displacement norm less useful.
- The material can expand freely and as a consequence, the material has barely any internal forces which make the force norm less useful.

DIANA also suggests that two convergence criteria should be used to perform an accurate analysis. The displacement norm and the force norm are used in this research project since the model is neither displacement prescribed nor easy to expand.

7.4. Result and Discussion

In this research project, the objective is to understand structure response under the static wind action. FEM can yield a significant amount of results. Only the key problem at specific load steps will be addressed in this section. More results will be shown in Appendix D. This section will start with investigating load steps-deflection curve. Some critical load steps are of interest to study.

7.4.1. Load steps-Deflection Curve

Load steps-deflection curves obtained in the nonlinear static analysis gives the structural response with every wind load increment. This load steps-deflection curve is the displacement of a local point at the windward side at the top of the shell wall. Hence the displacement is a combination of global displacement and local displacement. The discontinuities in the curve are important as the failure mechanism of this complex model is unknown. The slope of the curve gives averaged stiffness of the structure. The load steps-deflection curve shows in Figure 7.3 for these three models.

Several points on the curves marked in the figure are noteworthy. Once the marked points so as the structural behavior are understood, a further model improvement can be made. Five points are mentioned and they are marked on Figure 7.3 by capital letters.

- **Point A** At the first load step. the structure is under the self-weight only.
- **Point B** The point that the Shell No Transverse Nonlinear Model starts to diverge.
- **Point C** At this point, a significant deformation occurs.
- **Point D** The point at which the curve between Beam Nonlinear Model and Shell Nonlinear Model start to separate from each other.
- **Point E** The point is the last load step for Shell Nonlinear Mode.

7.4.2. Point A

At load step 1, only self-weight is loaded. Figure 7.4 shows the in-plane meridional stress resultant distribution over the tower height. The curves show a linear force distribution and the maximum compressive stress at the base is 9.33MPa. However, local bending is found at the stiffening rings which causes cracks.

The crack strain distribution on concrete shell wall shows on the left of Figure 7.5. As can be seen, the crack emerges at the upper cone. The largest crack strain is 0.000095 at 900m where the first intermediate ring is located. Furthermore, cracks are found in the first top 5 intermediate stiffening rings from the height of 500m-900m. The cracks all locate at the vertical section of the intermediate rings (Figure 7.5).

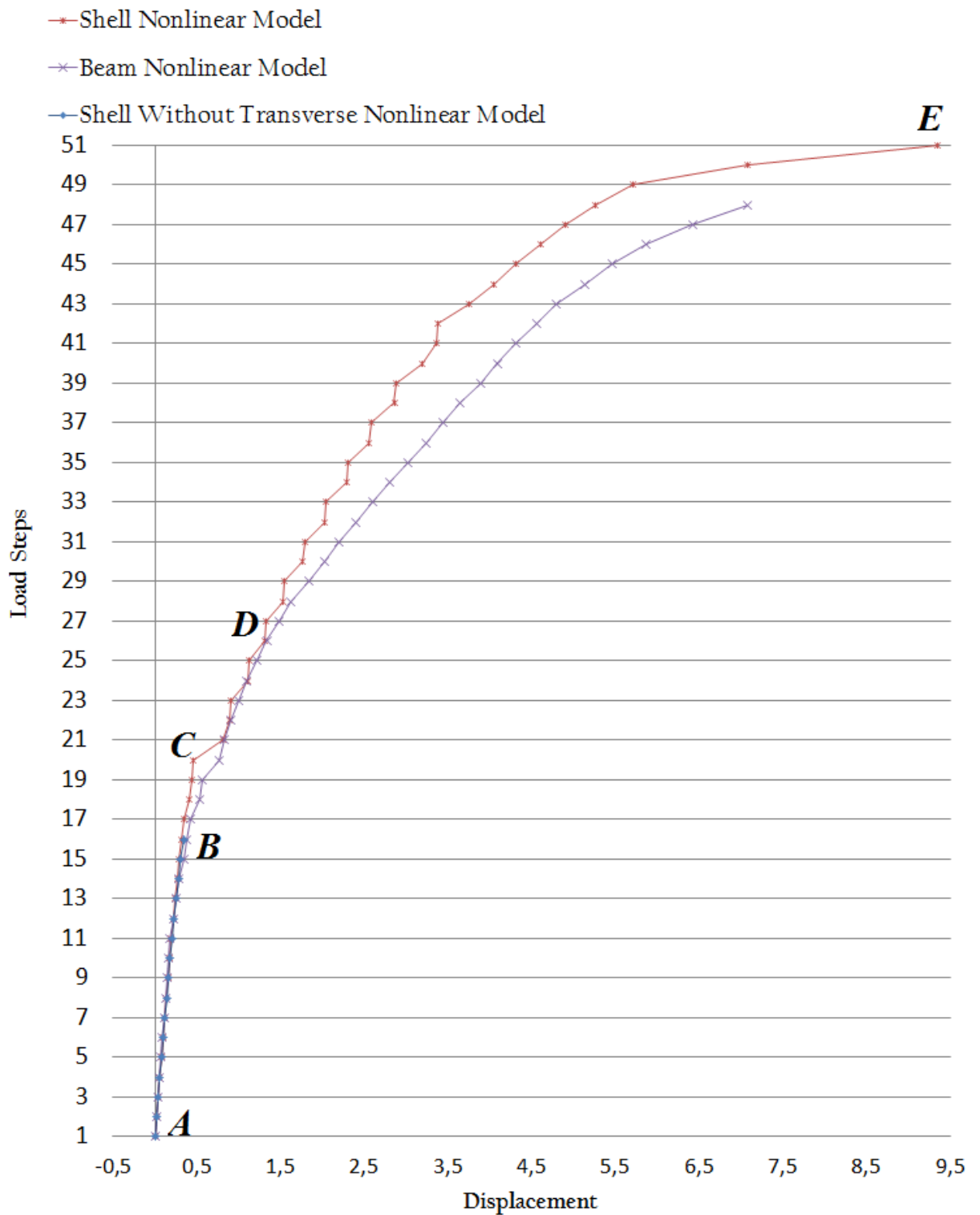


Figure 7.3: Load steps-deflection curve for nonlinear analysis for Shell Nonlinear Model, Beam Nonlinear Model, Shell no Transverse Nonlinear Model

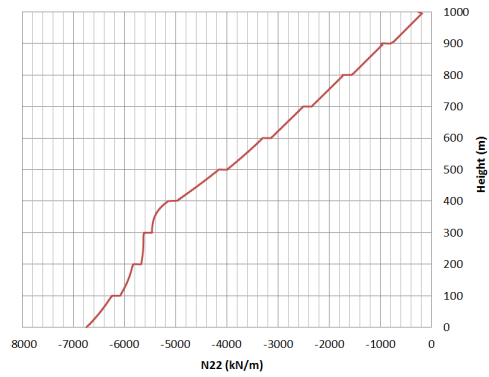


Figure 7.4: The meridional stress resultant for shell walls at windward side of the tower of SNM under self-weight

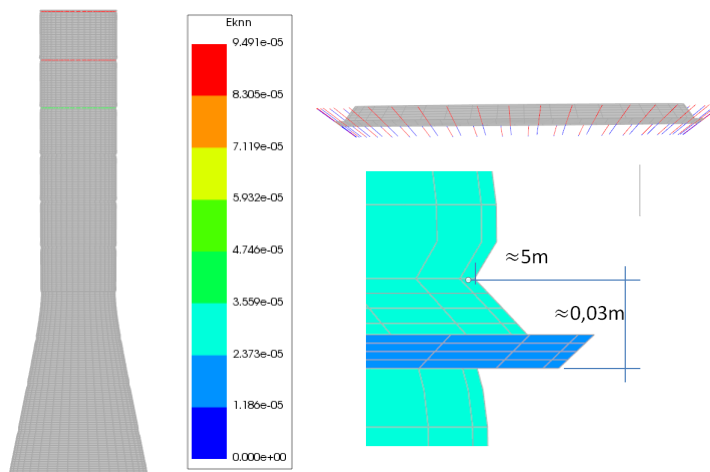


Figure 7.5: The crack strain distribution on the shell wall under self-weight(left); the crack distribution on the stiffening rings (right up); the deflected shape of stiffening rings under self-weight(right-down) (SNM)

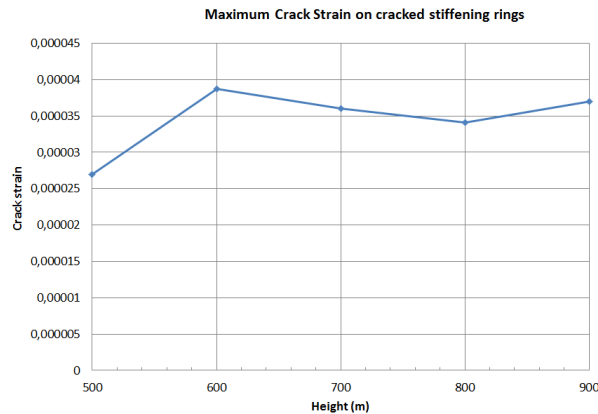


Figure 7.6: The maximum crack strain at the stiffening rings under self-weight (SNM)

In Chapter 5, it was concluded that the self-weight has a positive effect on preventing overturning of the tower caused by the wind load. But the mass center line of all stiffening rings located at outside of the mid-surface of the shell walls with a cantilever of 5m long, and the self-weight of reinforced concrete stiffening ring leads to a large bending moment at the ring-wall connection. Figure 7.5 also shows the deformation of intermediate stiffening ring. The deflection is around 0.03m for top 4 intermediate rings.

The maximum crack strain at each stiffening ring is shown Figure 7.6. From 800m-600m, with the decrease of the tower diameter, the crack increases. It was observed that the largest crack strain located at 900m both the shell walls and the stiffening rings. The reasons are the following

- The shape and location of the intermediate ring give larger bending moment compared to the top U-shape ring.
- The wall thickness of 0.25m is the thinnest over the tower.
- The location is rather close to the free end of the tower which has less constraint.

The distribution internal forces over the tower proves the structural behavior linearly. Locally, at upper cone, cracks are already initiated in the stiffening rings and the ring-wall connection. Large crack strain and local failure might occur if the wind load is added. After the wind action is loaded, 900m might give large local failure. It can, therefore, be stated that the structure behavior might be improved by eliminating the bending moment caused by self-weight.

In Beam Nonlinear Model, no cracks are found on the stiffening rings. The ring deforms in transverse direction due to the eccentricity. This behavior can be explained by the fact that the structural response in beam transverse direction is not taken into account in Class III 3D beam element.

7.4.3. Point B

Before analyzing point B, it is of interest to show the crack development from point A to point B in SNM (Figure 7.7). The load increases from 1D+0.04W to 1D+0.32W. All top six stiffening rings crack once the load once the wind load is added. As shown in Figure 7.7, only the vertical segment of the ring cracked at the beginning, while from step 9 with wind load factor of 0.16W the horizontal segment of stiffening ring starts to crack. At step 11, the second stiffening ring begins to extend the cracks to the shell walls. The ring at throat height(400m) starts to crack at step 15.

At point B, the structure experienced a discontinuity in SNM and the model failed to converge in STNM. As can be seen in Figure 7.3, the structure behaves linearly from point A to point B. Starting from point B, the stiffness of the structure decreases. Figure 7.8 gives the deformed shape of the first

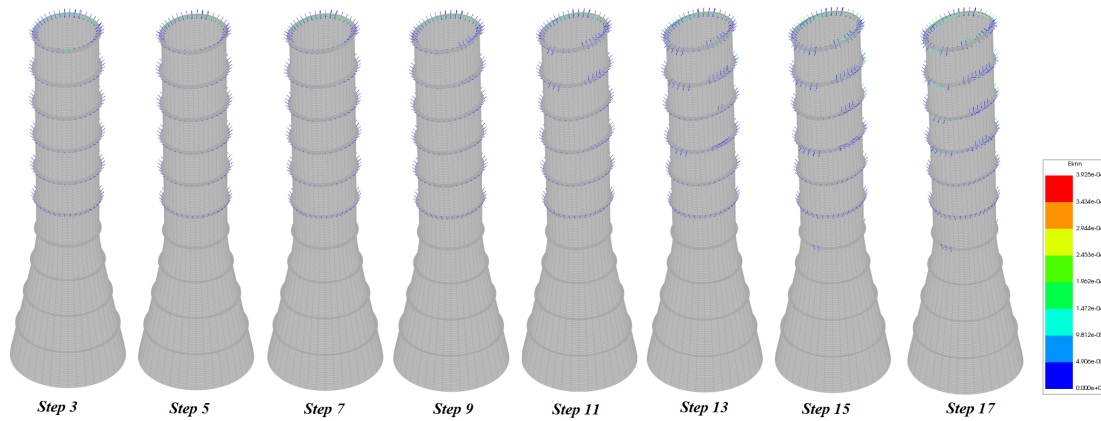


Figure 7.7: The crack distribution of SNM from load step 3 to 17

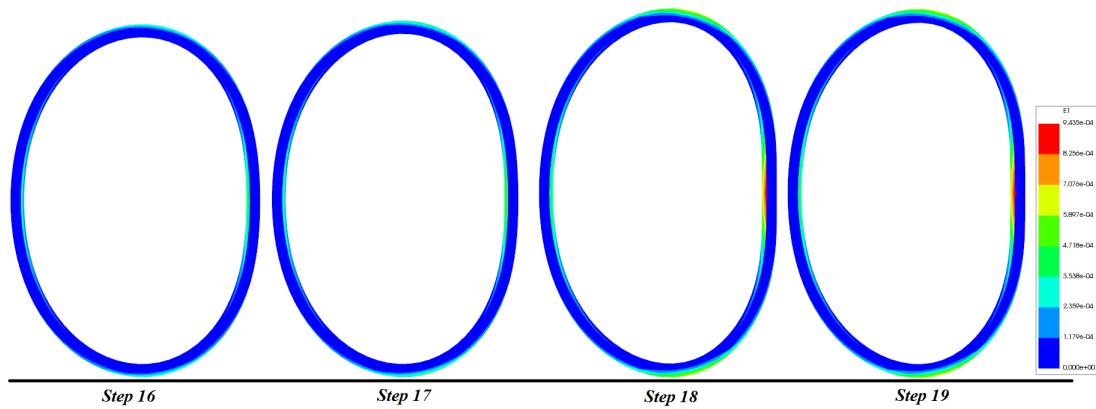


Figure 7.8: Principal strain distribution of the intermediate ring (900m) for SNM

intermediate ring from step 16-19 with the first principal stress distribution of SNM. As can be seen, after step 17, the shape of the ring changed to a larger ovalizing deformation and the stress concentrated on the windward side of the ring and 90° from the windward side (cross-sides).

Figure 7.9 shows the comparison of the concrete tensile model of the stiffening rings with the development of the first principal strain until the load step 20 (SNM). At point B, the principal strain violates the ultimate tensile strain of concrete of stiffening rings (0.001115). With the increasing of the tensile force, when the concrete tensile stress exceeds the tensile strength, the crack is initiated and the stress starts to drop. Then the tensile stress keeps dropping due to the gain of crack strain and more load is transferred to the reinforcement. Between load step 17-18, concrete tensile stress dropped to zero and moved all tensile forces to reinforce grid, which means the tension stiffening effect vanishes. For STNM, divergence occurred once the tensile stress of concrete on the stiffening ring dropped to zero. Tensile force in concrete has no reinforcement to carry in the transverse direction and the force unbalance causes the divergence of the system.

Last but not least, in Beam Nonlinear Model, the cross-section of the tower experiences one kink at the windward side of the tower between load steps 17-18. Figure 7.12 gives the deformed shape from load step 16-23. The kink is marked in the red circle on the tower at load step 18. Same as Shell Nonlinear Model, this is due to part of structure material violates the ultimate strain of the stiffening rings (0.001115).

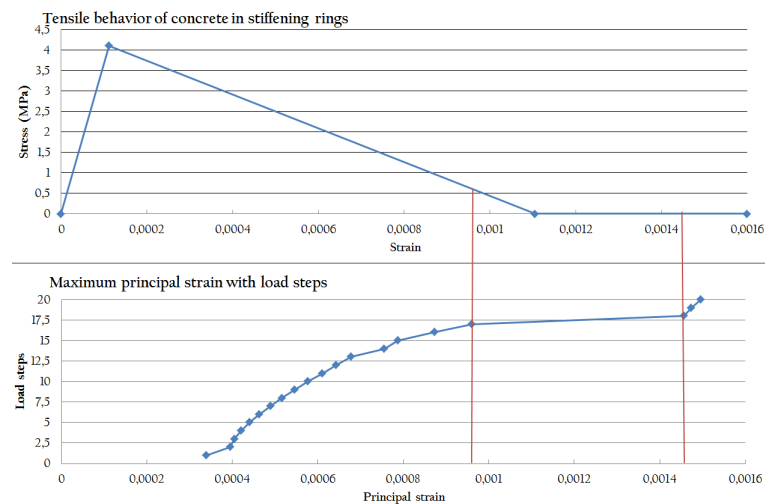


Figure 7.9: The comparison between concrete cracking model of the stiffening rings with maximum crack growth until load step 20 for SNM

7.4.4. Point C

At load step 18, the material in tension violates the concrete ultimate strain of the stiffening rings. At point C, with wind load factor of 0.4, structural sections in tension has violated the ultimate crack strain of concrete of shell wall (0.00177). A curve discontinuity is found between load steps 20 to 21 with a large displacement and a decreased stiffness. Figure 7.10 shows the comparison of the concrete tensile models and the development of the principal strain until load step 23. The principal strain increases suddenly two times larger than that of load step 21. It is because the reinforcement is elongated by the tensile force once the concrete has lost all tensile bearing capacity.

Figure 7.11 gives the crack distribution over the whole tower from load steps 19 to 22 and the top view of deformed top rings with the strain distribution. The cross-section of the cone changes to non-ellipsoid shape. The shape of the wind-ward side of the tower is flattened and the two cross-sides is under large bending. Three kinks appear at the cross-section of the cone. They located on the windward side of the tower and two cross-sides. Instead of a smooth stress distribution, at load step 21, the large strains concentrate at three kinks.

Similar to Shell Nonlinear Model (SNM), a large deformation occurred at load step 20 for Beam Nonlinear Model (BNM) whose maximum strain exceeds the ultimate tensile strain of concrete shell wall. While, instead of three kinks in SNM, BNM has four kinks at the upper cone. Except for the kink at windward side occurred at load step 18(7.12), three other kinks occur at load step 20.

7.4.5. Point D

Point D is neither a specific discontinuity nor a divergence. However, around point D, the load steps-deflection curve for BNM starts to separate from the curve of SNM. For SNM, horizontal cracks on the rings violate the ultimate tensile strain results in a zero tensile stress and then the transverse reinforcement is taken over. For BNM, beam elements in all stiffening rings do not take transverse direction into consideration as well as the transverse reinforcement. The beam theory only considers stress and strain in the beam axis. The cross-section of the beam remains planer but not necessarily perpendicular to the deformed beam axis. It gives a certain constraint on mechanical properties in the transverse direction. It is of interest to know the degree of constraints in the transverse direction is given by beam theory.

The STNM and BNM have only the longitudinal reinforcement modeled in the stiffening rings. The only difference is that the stiffening ring is modeled by curved shell elements in STNM and it is

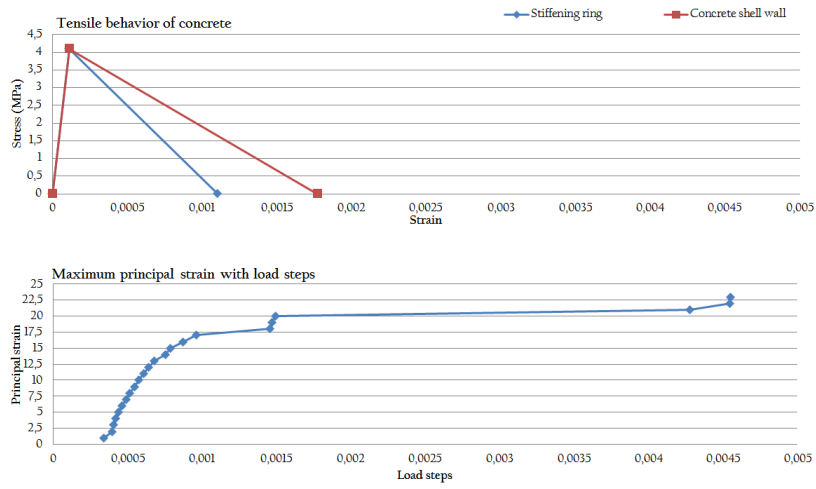


Figure 7.10: The comparison between concrete cracking model of stiffening ring with maximum crack growth until load step 23 for SNM

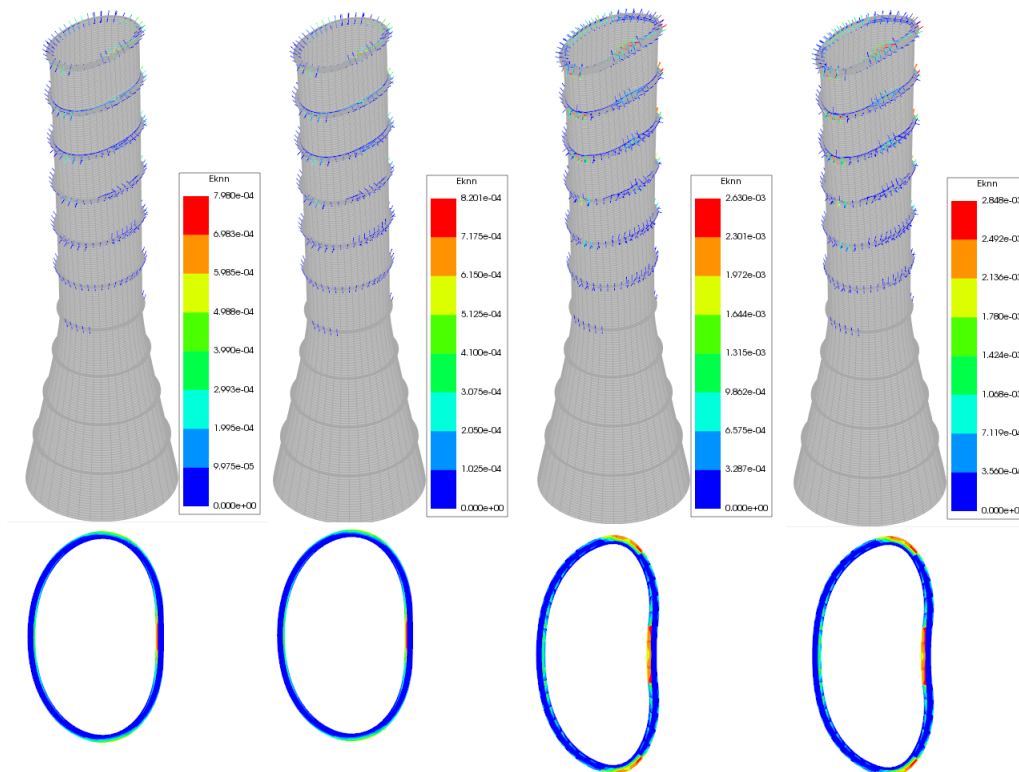


Figure 7.11: The crack distribution of SNW of step 19 (1st), step 20 (2nd), step 21 (3rd), step 22 (4th) and their deformed shape of the top stiffening ring

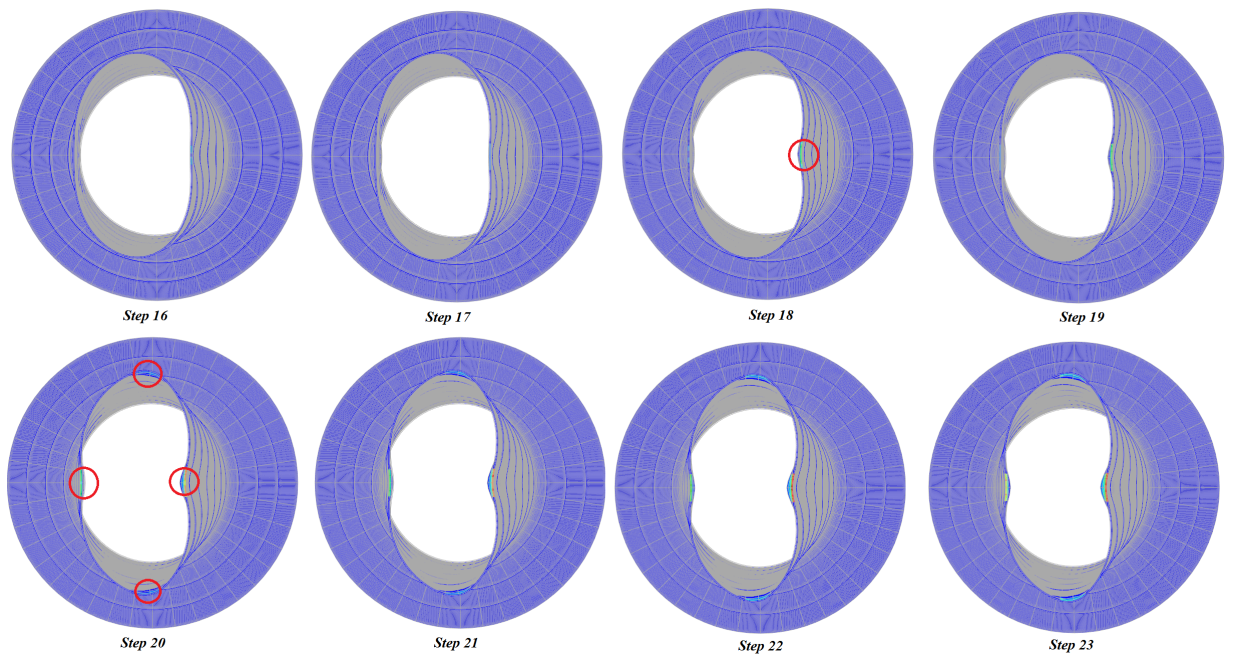


Figure 7.12: The deformation of Beam Nonlinear Model from load step 16 to 23 with normalized deformation

beam elements in BNM. The STNM divergences at early load step 17 while, BNM divergences at load steps 48. It can be concluded that with no transverse reinforcement, the beam element gives a more stiff behavior than the shell element due to the theoretical constraint.

SNM has a transverse reinforcement ratio of 1% on the stiffening rings. Thus by adding the reinforcement, a certain stiffness is defined. The curve shows that after the discontinuity, the model BNM has less stiff behavior than SNM. It means that the given certain stiffness in SNM is higher than the theoretical constraint of beam elements. If the nonlinear analysis is modeled by BNM, the structural response will be underestimated. With the increase of the reinforcement ratio, the SNM is able to give an increasing structure stiffness which will not occur if BNM is used. The SNM should be adopted in the further research project instead of BNM.

7.4.6. Point E

Only Shell Nonlinear Model converged at the last load step. The deflection, the crack distribution, the stress resultant and the reinforcement stress distribution will be shown in this section. As can be seen from the load steps-deflection curve of SNM, the structure behaves non-linearly. At last two load steps, the structure gives very large deformations and their stiffness decreases near to zero. It means a structural failure occur at the last load step. The curve reached a plateau. A more detailed investigation is given in the following.

Deflection

The deflection and deformation help with visualizing the failure mechanism of the structure and its critical areas. A comparable study is made between Linear Detailed Model and Shell Nonlinear Model. The deformed shape with the windward displacement contour plot shows in Figure 7.13 for both LDM and SNM. For SNM, the upper cone is entirely distorted. The greatest deformation is positioned at the shell walls just below the top ring with the magnitude of 9.4m because the top shell wall is under the biggest wind load and has the thinnest wall thickness. The ring is deformed out of the wall

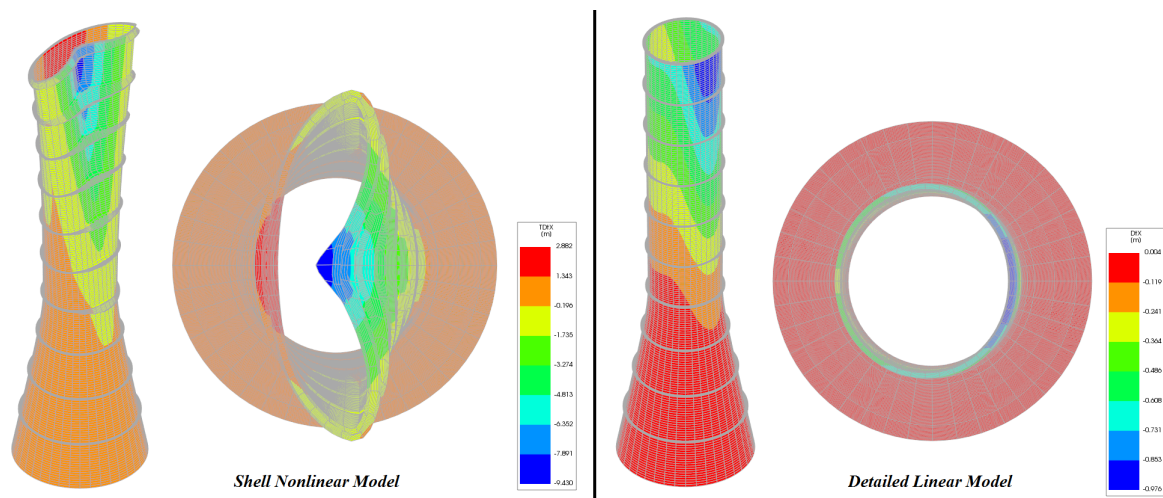


Figure 7.13: deformed shape for SNM and DLM with factor of 10 and the contour plot is the displacement in windward direction

considerably. For DLM, the upper cone remains almost circular without large ovalization or kinks.

Figure 7.14 gives the global deformation(left) over the height of the tower for both SNM and DLM as well as the picked location(right). Their maximum global displacement at the top of the tower is 1.14m and 0.636 for SNM and DLM respectively which gives an 82% difference. In DLM, the nonlinear material properties gives a weaker structural response. The displacement of two models at lower 400m for SNM and DLM are overlapped. However, starting from the throat height, the SNM deforms more and more. We can say that the lower part of the tower is still in the linear region, while the non-linearity of the upper cone is fully activated. The throat height at which DLM and SLM start to separate in the Global displacement curve can be viewed as a kink in the vertical direction. The eccentricity of the stiffening rings results in a protrusion on every ring location in SNM. At beginning, the 5m cantilever of the stiffening rings causes a downward deformation of the ring under its self-weight. With the increasing wind load, this deformation becomes larger until the whole ring is pushed out of the wall. For DLM, the displacement is a smooth curve, which indicates the stiffening rings deform following the adjacent concrete wall without being pushed out of the wall.

Figure 7.15 shows the local displacement of the tower for both SNM and DLM. The location at which experiences the largest displacement shows on the right-hand-side of the figure. Unlike the global displacement with only 83% increment, the SNM is ten times larger than the DLM in local deformation. Large protrusions are discovered in SNM with the length of 2.6m located at the first intermediate ring(900m), which is also the most critical location when the tower is under the self-weight only. From 900m, the protrusion length decreases with decreasing tower height. There are no significant differences between local and global behavior for DLM. In the nonlinear analysis, the structure might present a minute global deformation with massive local failure.

Crack strain

The crack strains are calculated automatically by DIANA. For the total strain rotatind crack models, the crack strain ϵ^{CT} is defined as

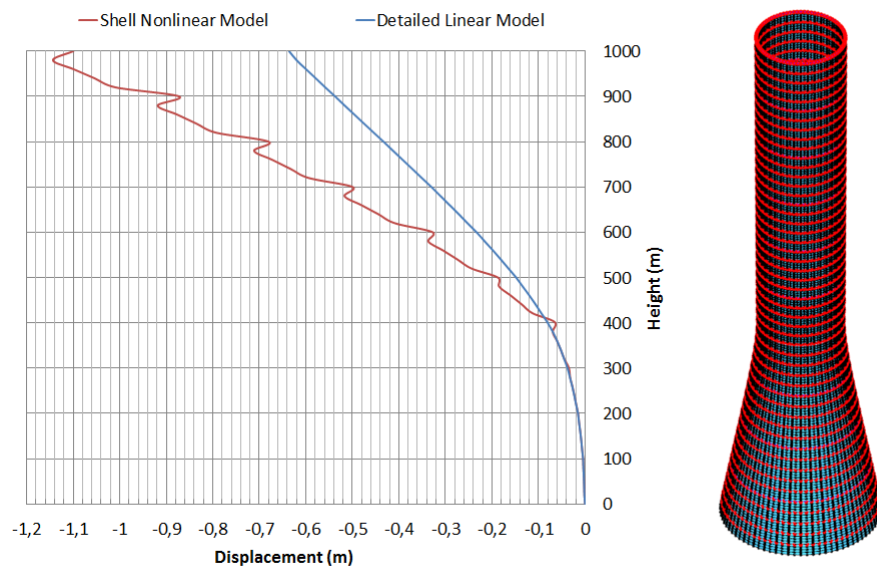


Figure 7.14: Global displacement of Shell Nonlinear Model and Detailed Linear Model at last load step(1D+1W)

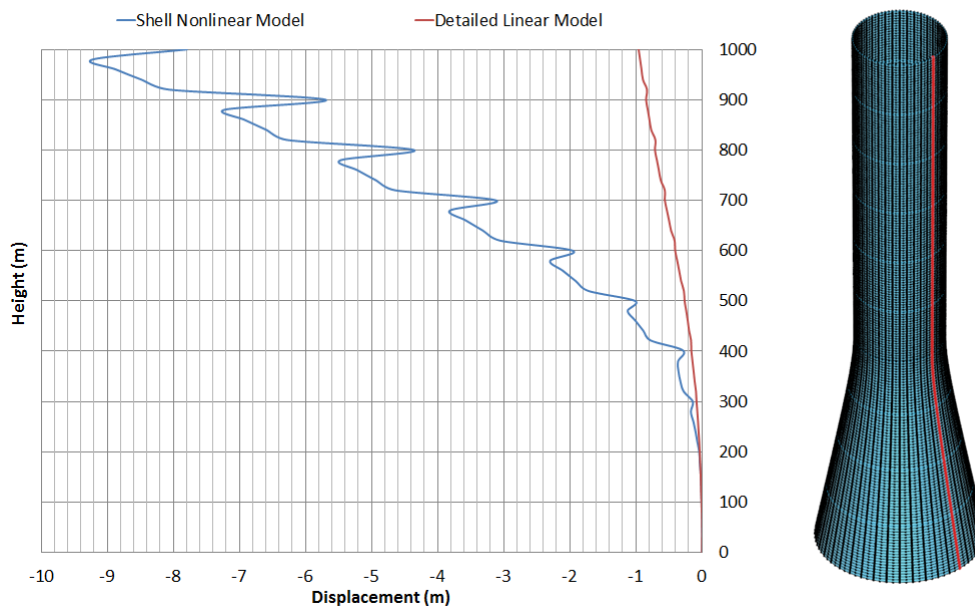


Figure 7.15: Local displacement of SNM and DLM at the last load step(1D+1W)

$$\epsilon^{cr} = \epsilon^{nst} - \frac{\sigma}{E} \quad (7.1)$$

Where

- n, s, t crack strain in I II III crack modes
- σ material stress
- E Young's modulus of the material

Once the crack strain is known, the crack width can be calculated. According to EN 1992-1-1, the serviceability limit state design gives the requirement for crack control. The Eurocode provides allowable maximum crack width for the reinforced concrete structure with the magnitude of 0.4mm. Depending on the environment of chosen location, the maximum crack strain might decrease to 0.2mm. To calculate the crack width, the maximum crack spacing should be known. In the situation where bonded reinforcement is applied, the maximum crack spacing is calculated by the following expression according to NEN-EN 1992-1-1:

$$S_{r,max} = k_3 c + k_1 k_2 k_4 \phi / \rho_{p,eff} \quad (7.2)$$

Where

- ϕ bar diameter. VGB guidelines recommend a bar diameter of 8mm.
- c cover of the longitudinal reinforcement
- k_1 takes account the bond properties for the bonded reinforcement (0.8 for high bond bars)
- k_2 takes account of the distribution of strain (0.5 for bending; 1.0 for pure tension)
- k_3 and k_4 the recommended value is 3.4 and 0.425 respectively.

For this research, the concrete cover is assumed to be 40mm, and the calculation of concrete cover can be found in Appendix B. The reinforcement is bonded to the concrete. It is assumed that the shell walls are under bending. The maximum crack spacing according to the equations above would be 476mm. The maximum crack width can be calculated by multiplying crack spacing with the crack strain. If the maximum allowable crack width is 0.4mm, the maximum crack strain would be 0.0008.

Figure 7.16 (lower five plots) shows the crack strain distribution. These five plots show the crack distributions on the five layers in the thickness direction. The upper part of concrete shell wall is filled with crack, both at the windward side, the leeward side and two cross-sides. The distributions of crack strain that exceeds the maximum allowable value (0.0008) are shown in Figure 7.16 (top five plots). Those layers were located at different depths of the shell walls, while every layer is heavily cracked at the top seven stiffening rings. Even though there is a large area of cracking generated at the upper shell wall, only two non-allowable cracks vertically go through the first three segments of the concrete wall.

The maximum crack strain is 0.059 located at the two cross sides of the second stiffening ring (900m) and by multiplying the crack spacing, the crack width is 17mm. This indicates a complete failure of the stiffening rings where the concrete cracking and the steel yielding occurred. The areas that have the largest crack strain are marked in Figure 7.16 with the black circle.

Concrete in compression

The concrete functionality in an RC structure is to carry the compressive force. It is not a desirable structural design if the material failed in compression because concrete is rather brittle. Visualizing

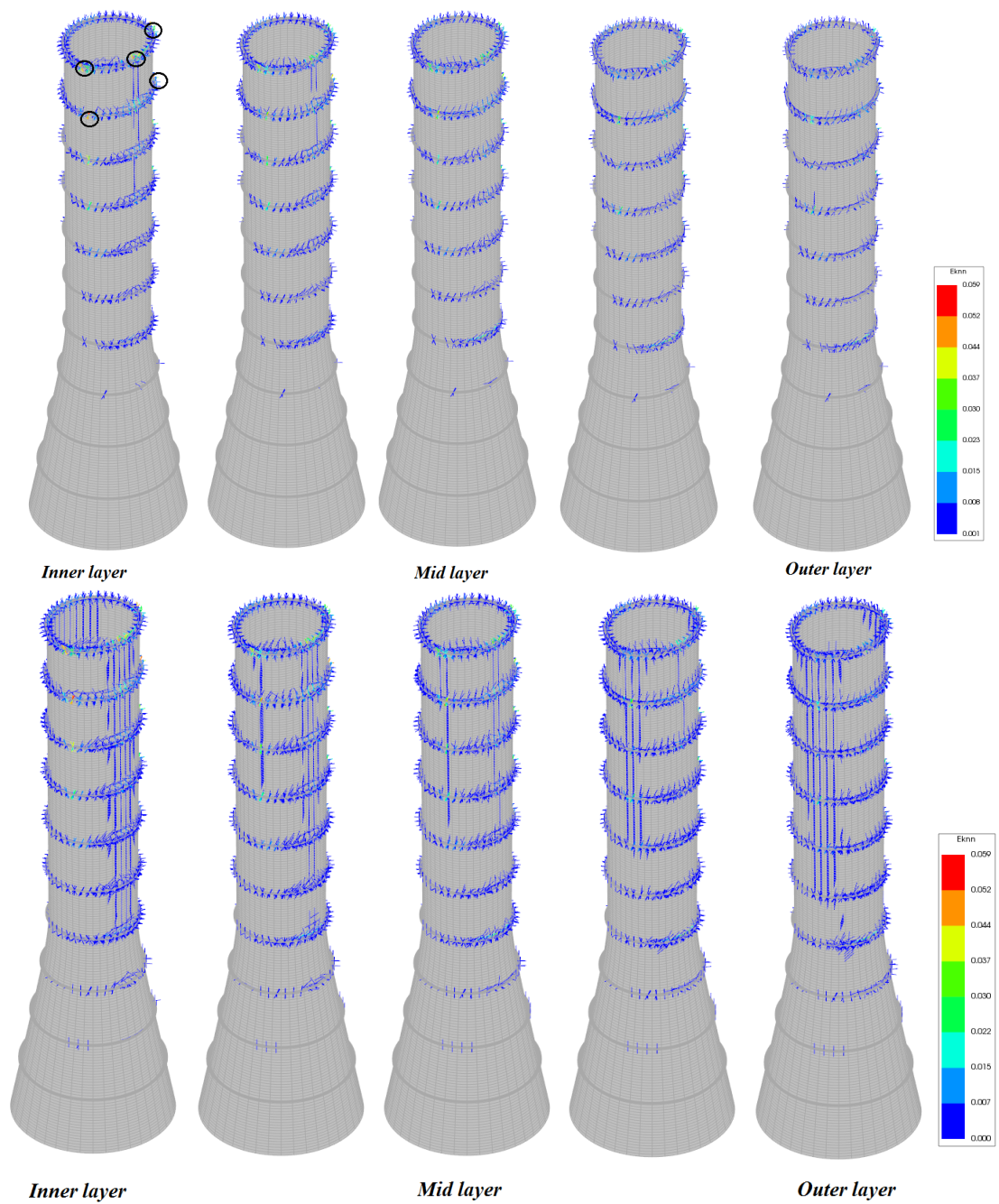


Figure 7.16: Crack strain distribution that exceeds the maximum allowable value for the 5 layer from inner to outer (top) Crack strain distribution for 5 layers from inner to outer of SNM(bottom)

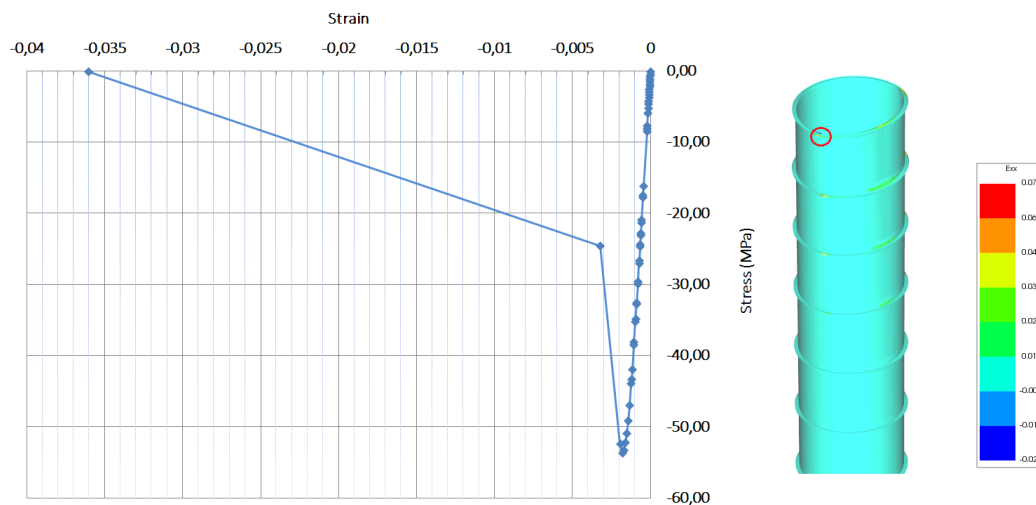


Figure 7.17: Concrete stress-strain curve at a critical point(left); the strain distribution in the circumferential direction(right)

the structure in compression can find if there is a brittle failure in the structure. In this research, the lateral cracking and the lateral confinement effect will be taken into account (see Chapter 6). The large area of lateral cracking distributed over the upper cone might decrease the compressive strength of the concrete. Furthermore, due to the self-weight, the circular hollow cross-section of the tower provides the lateral constraint, which gives a higher compressive strength and ductility.

According to the formula of Thorenfeldt described in Chapter 6, without considering multi-directional stress state and lateral cracking, the maximum compressive stress is 58MPa. The strain at peak stress is -0.0021. After adding the effects of lateral confinement and lateral cracking, both values might change and they depend on the loading condition at every node. A point having the largest compressive strain is chosen for a stress-strain plot (Figure 7.17). The location of this point is marked at the figure in the right-hand-side with a red circle. As shown in the curve, the point has a relatively high stiffness until the peak value. The peak value reached at the load step 48 and then the sudden drop on the stress occurs in last two load steps. It shows a brittle concrete behavior. The figure at right-hand-side shows the strain distribution of SNM in the circumferential direction. As can be seen, the stress is not uniformly distributed over the whole tower. A high strain concentrates at the kinks. By comparing the concrete cracking and concrete crushing, the location where for concrete crushing is also the places gives the largest concrete cracking at the top cone. Figure 7.18 indicates the region of the concrete crushing. In the circumferential direction, the wind load pushes the circular shape of the tower into ovaling and then the thin shell failed by the out of plane bending, which causes the crushing in the circumferential direction. In meridional direction, the crushing is mainly caused by the wind action which gives a large deformation of the stiffening rings. The ring is pushed out of the shell walls that leading to a large bending moment at the connection.

In conclusion, the concrete crushing did not occur over the whole structure but mainly concentrates at the connection between the shell walls and the stiffening rings. The crushing is not caused by pure concrete in compression but by bending mechanism, which means the shell walls have large cracks on one side of the shell and concrete crushing on the other side.

Stress resultant It is hard to avoid tensile force in the circumferential direction due to the ovalization deformation. However, investigating the differences in stress resultant in meridional direction gives the potential on structural optimization since its distribution and magnitude is sensitive to the design of the stiffening rings.

Figure 7.19 shows the meridional stress resultant at the windward side for DLM and SNM. The

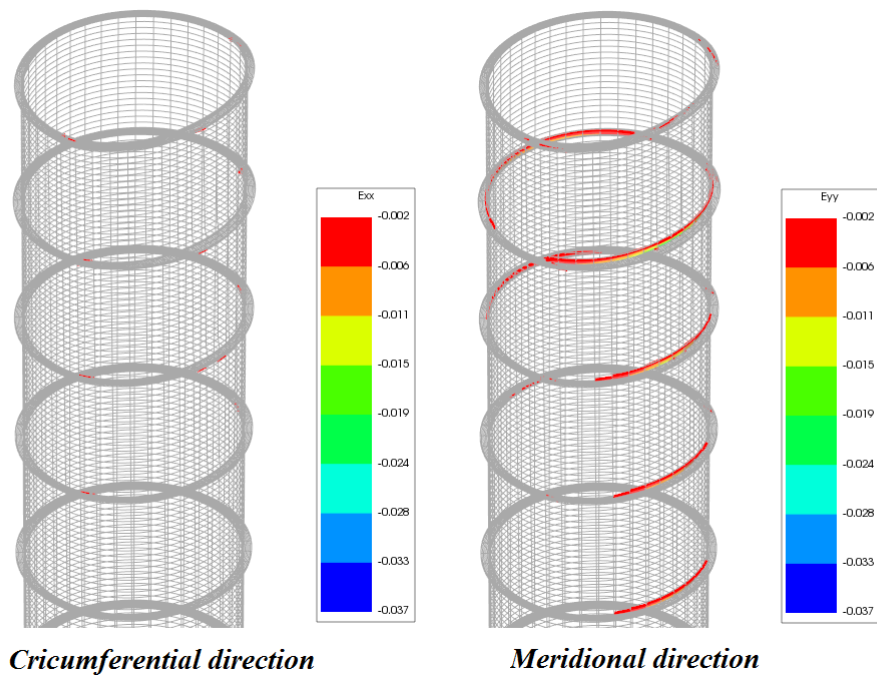


Figure 7.18: The distribution of concrete crushing in the circumferential direction(left) and the meridional direction(right) for SNM at 1D+1W

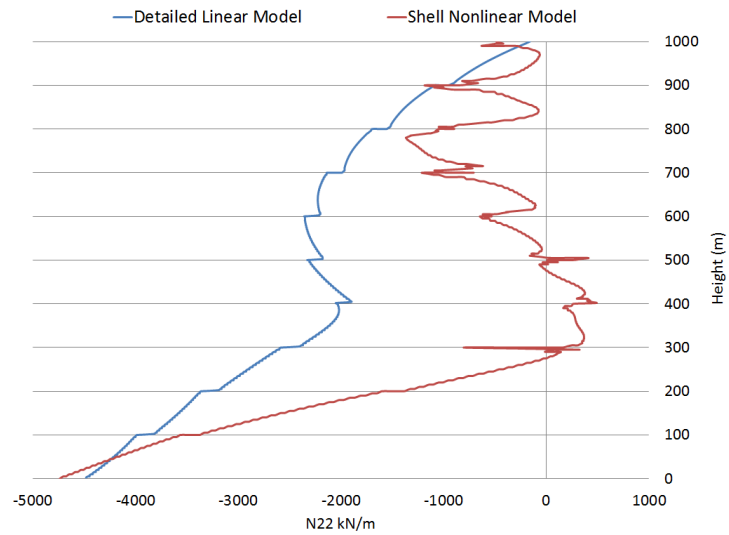


Figure 7.19: N22 stress resultant distribution over height for Shell Nonlinear Model and Detailed Linear Model at 1D+1W

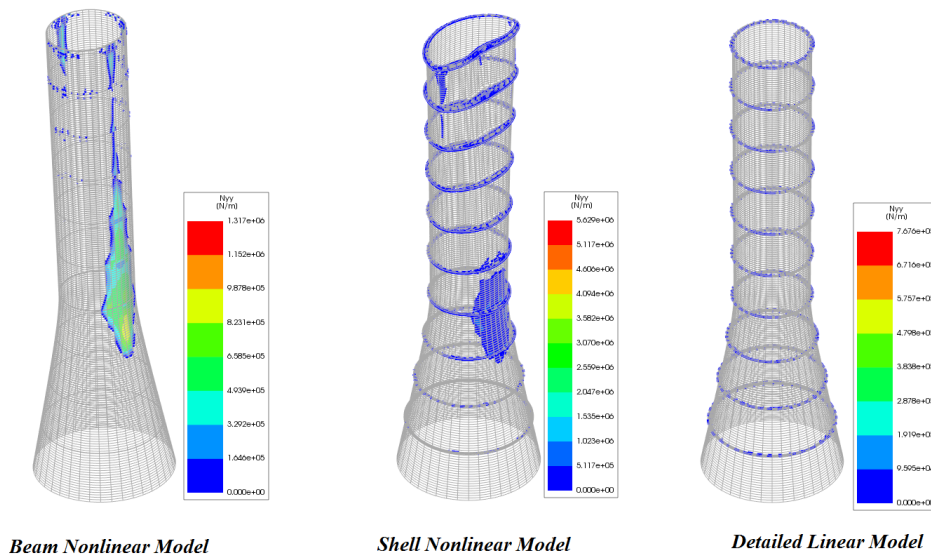


Figure 7.20: Tensile stress distribution in the meridional direction for Beam Nonlinear Model(left) Shell Nonlinear Model(middle) and Linear Model(right)

stress resultant is under compression in DLM. With adding nonlinear material properties, the vulnerability of the tower to wind action was found to be much higher. Due to the bending moment acting at the connection between the shell walls and stiffening rings, the curve for SNM has a distorted shape and large force variation. In SNM, at the windward side of the tower from 300-500m, the shell walls are under direct tension. The large differences between linear and nonlinear analysis reveal that the structure is relatively weak and material non-linearity arises in a high degree.

Figure 7.20 refers to the tensile meridional stress resultant distribution for BNM, SNM and DLM. For the stiffening ring modeling, since the beam element has a weaker stiffness in the transverse direction compared to the curved shell element who has the transverse reinforcement ratio of 1%, a long and large area of concrete shell wall is under direct tension in BNM compared to SNM.

In SNM, the tensile resultant mainly located at top six stiffening rings and throat height. The area that under direction tension at throat height is smaller than that of BNM. Large tensile forces also concentrated on stiffening ring due to the ovalization deformation failure of the upper cone. Only small amount of tensile resultant located at stiffening ring in SLM. No tensile resultant is observed at the shell walls.

Figure 7.21 presents the circumferential distribution of the meridional stress resultant on the shell wall at the height (390m). A tension zone is observed on the windward side and large compressive forces at about two cross sides. In a perfect beam-like behavior, the meridional force in the circumferential direction should be a straight line, and it will be tension on the windward side and compression on the leeward side in this case. As can be seen the curve for SNM, the stress distribution is neither smooth nor linear and with the high peaks in tension zone and the low ebbs for the compression zone for SNM. The DLM shows a much linear-like forces distribution.

The structural design with 1% reinforcement ratio for the stiffening rings and averaged 0.35% of reinforcement ratio for the shell walls are not sufficient to avoid tensile stress on the shell walls. The stiffness of the stiffening rings should be increased by adding more reinforcement.

7.4.7. Reinforcement

From the previous analysis, given cracking and crushing of the concrete, the reinforcement yielding occurs in the structure. Figure 7.22 present the yielding reinforcement distribution in the circum-

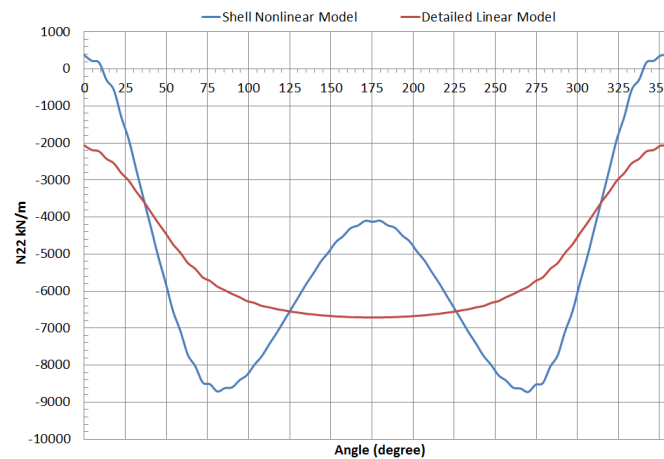


Figure 7.21: N22 in the circumferential direction at throat height for Shell nonlinear Model and Beam Nonlinear Model

ferential direction and the meridional direction.

The yielding of the reinforcement is mainly located at the ring-wall connection. The stiffening ring has a larger thickness(0.8m) and a higher reinforcement ratio(1%), and thus few yielding of reinforcement is found at the rings. Most of the cases, the area of the yielding of reinforcement is the shell walls who has a thinner thickness and low reinforcement ratio.

7.5. Conclusions

Different from most of the analytical models, by analyzing a relatively weak structure, the possible structural failure mechanism can be shown. The reinforcement can be added only to the problem area instead of the whole tower once the problem area is known. Some conclusions are described,

- Due to the lack of the transverse direction degree of freedom, the beam element is not sufficient for nonlinear material analysis.
- The initial crack caused by the self-weight gives the adverse effect on structural behavior, particularly for the shell walls.
- The significant deformation of the stiffening rings provide an enormous amount of concrete crushing and reinforcement yielding.
- Locally, the cross-section of the cone experience three kinks in Shell Nonlinear Model. Globally, a kink is located at the throat height.

For the current model with the 1% reinforcement ratio, the large concrete cracking and crushing occur due to out of plane bending at the upper cone. It can be concluded that the proposed model does not have enough stiffness and strength to resisting static wind load. In the next chapter, some improvements are adopted to optimize the structural behavior.

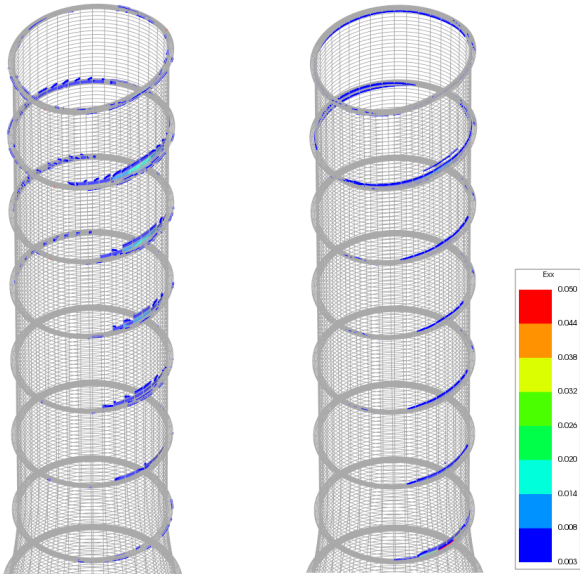
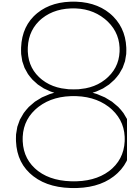


Figure 7.22: Yielding reinforcement distribution in the meridional direction(left) and the circumferential direction(right)



Model Optimisation

From the conclusion of Chapter 7 it was known that the structure could be optimized by increasing the reinforcement ratio and minimizing the eccentricity of the stiffening rings. This chapter makes a few attempts, firstly by increasing the reinforcement ratio of stiffening rings and secondly by moving the stiffening rings so that the eccentricity of rings vanish. Eventually these two attempts are combined to improve the structural response.

8.1. The structural model with increasing reinforcement ratios

This section deals with the influence of the reinforcement ratio of the stiffening ring on the structural behavior. The nonlinear analysis model setup was already mentioned in detail in the previous chapter. Each model presented in this section is based on the Shell Nonlinear Model with modification on the reinforcement ratio. Three models are considered, their definitions are shown below:

- **1% Nonlinear Model(1%NM)** This model is identical to Shell Nonlinear Model while a new name is used to highlight the usage of the reinforcement ratio.
- **2% Nonlinear Model(2%NM)** Based on the 1% Nonlinear Model, this model has increased the reinforcement ratio of the 10 stiffening rings to 2% in both directions.
- **3% Nonlinear Model(3%NM)** Same as the 2% Nonlinear Model, the reinforcement ratio of the stiffening rings has increased to 3% in both directions.

8.1.1. Model setup

It was known from Chapter 5 that an increase of the reinforcement ratio decreases the effect of tension stiffening of reinforced concrete. Before the tension stiffening effect can be added in FEM, the tension stiffening diagram needs to be calculated and finally integrated in order to get the ultimate strain. Table 8.1 gives the calculated ultimate strain with different reinforcement ratios.

Table 8.1: The calculated ultimate strain with different reinforcement ratios

Model	Reinforcement Ratio	Ultimate limit strain
1% Nonlinear Model	1%	0.00115
2% Nonlinear Model	2%	0.00043
3% Nonlinear Model	3%	0.00021

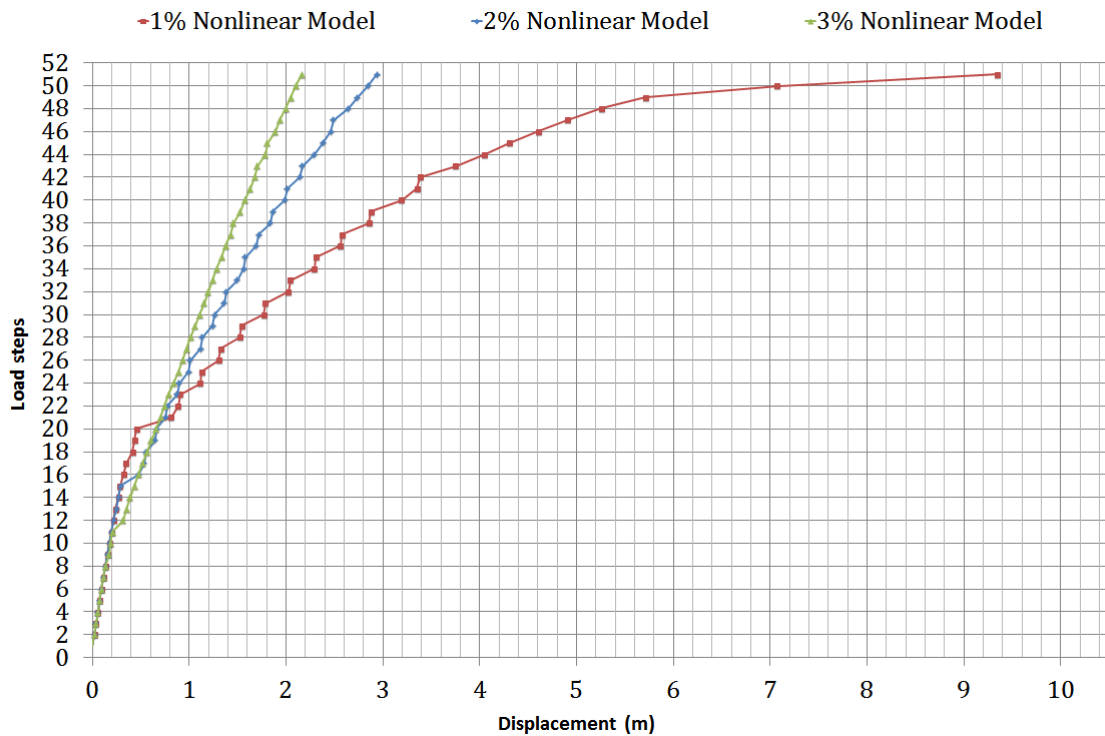


Figure 8.1: The load steps-deflection curve for model 1%NM, 2%NM, 3%NM

8.1.2. Load steps-deflection curve

The load steps-deflection curve (Figure 8.1) provides the direct visualization on the structural response. In the beginning, the three models generate an identical slope and from this it can be concluded that an increase of the reinforcement ratio has few influence on the overall stiffness of the structure in the early elastic stage. However, it does have influence when the structure steps into the nonlinear stage. As can be seen in the Figure 8.1, just after the elastic stage, all models experienced a discontinuity but at different load levels. The discontinuity occurs earlier for the model with a higher reinforcement ratio. The model with 1% reinforcement ratio gives the discontinuities at the load step 21, while it occurs at load step 16 and 12 for the models with reinforcement ratio of 2% and 3% respectively. The load level at which discontinuity occurred is related to the tension stiffening behavior of the stiffening rings. The low tension stiffening effect yield a early failure mechanism in 3NM.

All discontinuities are characterized by a sudden large displacement. 3%NM gives the smallest displacement among all three models. It depends on the reinforcement ratio on the rings. At the same loading level, the greater amount of reinforcement yields lower strain which gives smaller displacement. It also depends on the loading stage. The discontinuity occurs at a lower loading level for 3%NM. 1%NM gives the largest displacement at load step 21 with the lowest amount of reinforcement and largest loading level.

After the discontinuity, all models show a lower structural stiffness but the stiffness of the structure increases with the growth of the reinforcement ratio. 1%NM experienced structural failure who gives almost zero stiffness at the last few load steps. Compared to 1%NM, 2%NM had a large increase in the stiffness and a large decrease on the displacement, while there is less progress both on the stiffness and the displacement when the reinforcement ratio increase from 2% to 3%.

Table 8.2: The reinforcement ratio and ultimate strain of different models

Model	A1	A2	A3	B1	B2
Reinforcement ratio	2%	2%	2%	3%	3%
Ultimate strain	0.001	0.0065	0.004	0.001	0.0002

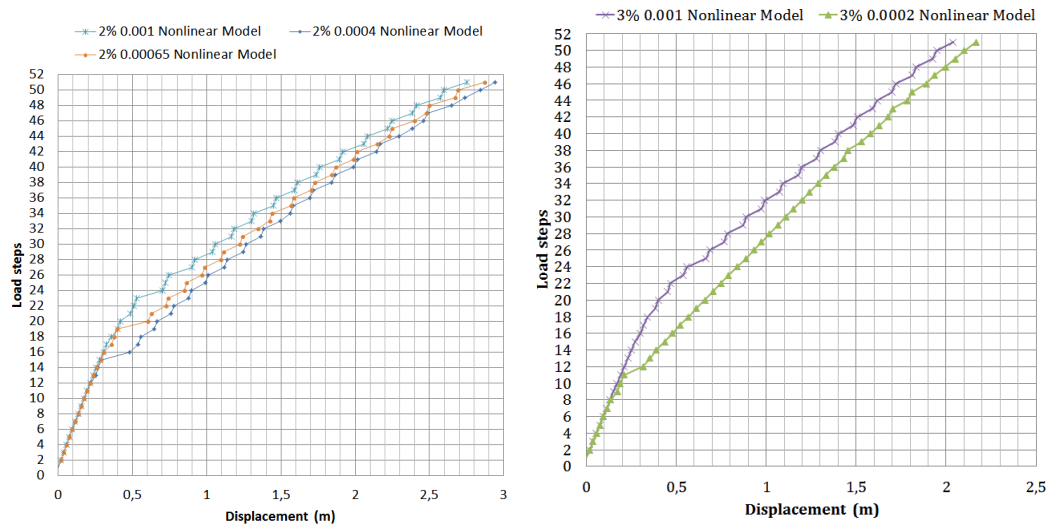


Figure 8.2: The load steps-displacement curve for A1, A2, A3 (left); The load steps-displacement curve for B1, B2 (right).

8.1.3. Influence of ultimate strain

Concrete cracking behavior plays a significant role in structural performance because it is related to the reinforcement activation and the stress redistribution. The last section has shown that the ultimate strain changes the load level at which the discontinuity occur. The experimental result builds the tension stiffening model, and it should be noticed that when the reinforcement ratio is high, the experimental results on the tension stiffening become scattered. It is of interest to understand the influence of the tension stiffening on the structural response. In this section, for the same reinforcement ratio, the models have increasing tension stiffening effect achieved by altering the ultimate strain. Two groups of models are listed in table 8.2.

Models who has same reinforcement ratio with increasing ultimate strain are compared in Figure 8.2. The left-hand side figure gives the comparison with models which have the reinforcement ratio of 2% and the 3% models are being depicted at the right-hand side. The three curves give the same slope at the beginning while the discontinuity occurred at a lower load stage for concrete with a lower ultimate strain. Moreover, the paths of the curves after the discontinuity are much similar compared to the curves in Figure 8.1 whose models have different reinforcement ratios.

Just after the discontinuity, the three curves are rather distant from each other. The model with the lowest ultimate strain (A3) gives the greatest displacement. With the increase of the loading, the three curves are starting to come closer to each other. There are no large differences on displacement at the last few load steps. The large separation and the following tightening of the gap between the curves can be explained as follows: 1) tension stiffening is the bonding behavior between the concrete and the reinforcement and this effect gives larger contribution when the tensile stress stays low. 2) after concrete exceeds the ultimate strength, with the increase of the strain, the contribution of tension stiffening decreases. 3) When steel is under high tensile stress, the structural response depends more on reinforcement ratio instead of concrete brittle tensile behavior. The similar tendency is found for model B1 and B2. Their differences on the displacement at the last load step are around 10%. To summarize, the influence of ultimate strain on the structure is high at low loading level and becomes

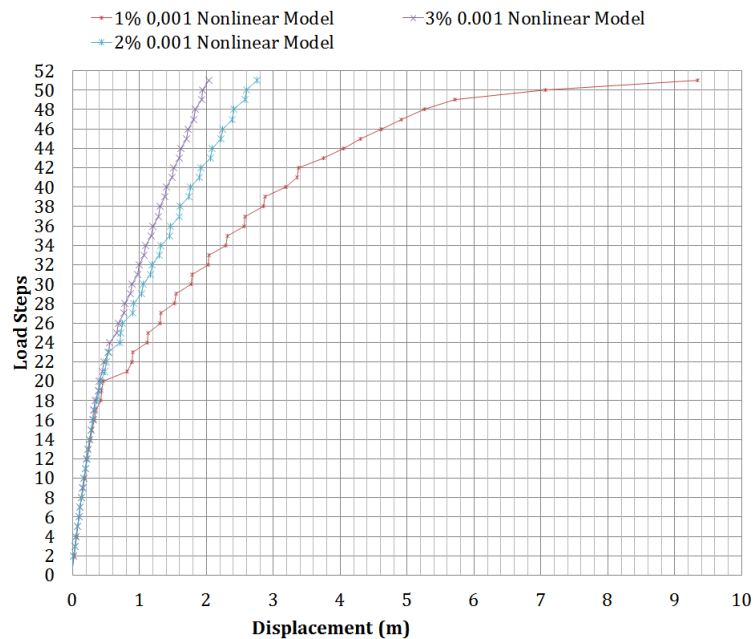


Figure 8.3: The load steps-displacement curve for model 1%NM(red), A1(blue), B1(purple)

lower at high loading level. The reinforcement plays a significant role in structural behavior after structural non-linearity rises.

Different reinforcement ratios used in the model might also relate to the discontinuity loading level. A comparison of models having a constant ultimate strain with increasing reinforcement ratio is displayed in Figure 8.3. With the same ultimate strain, the discontinuity occurred at a higher loading stage with the increase of the reinforcement ratio. It is because the higher amount of reinforcement also contributes to postponing the concrete cracking and reduces the cracking developing speed by the slower tensile strain development.

8.1.4. Maximum principal strain

Figure 8.4 gives the development of the maximum principal strain. Some discontinuities can also be found in the principal strain curves. All models occurred all at a similar strain region but at different load steps. These discontinuities cross the ultimate tensile strain of the shell wall. The speed of growth of the maximum principal strain depends on the reinforcement ratio in the structure. 1%NM has the fastest growth compared to other models and at the end few load steps. The fast strain development indicates that the reinforcement is yielding at the critical area. The cracks open without any increment on load bearing capacity. The model with 2% and 3% reinforcement ratio gives better structural performance. The strain growth is stable even until the last few load steps.

8.1.5. Deformation

This section gives the deformed shape of 1%NM, 2%NM and 3%NM. Figure 8.5 is the top view of the deformed shape of the three models. The deformed shapes of 3%NM and 2%NM is rather similar but 2%NM gives a larger deformation on the cross-section than 3%NM. All models have their largest displacements at the windward side at top of the cone with magnitude 9.43m, 2.96m, 2.19m for 1%NM, 2%NM, 3%NM respectively. For 1%NM, the cross section of the top cone has a large distorted deformation while 2%NM and 3%NM give smooth ellipsoid cross-sections without any kinks or discontinuities on their shape.

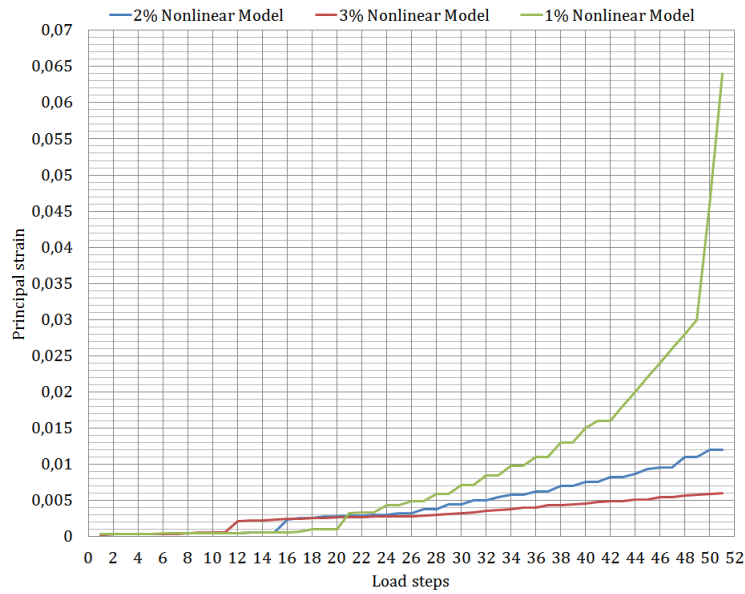


Figure 8.4: The maximum tensile principal strain development at inner shell layer for model 1% Nonlinear Model, 2% Nonlinear Model, 3% Nonlinear Model

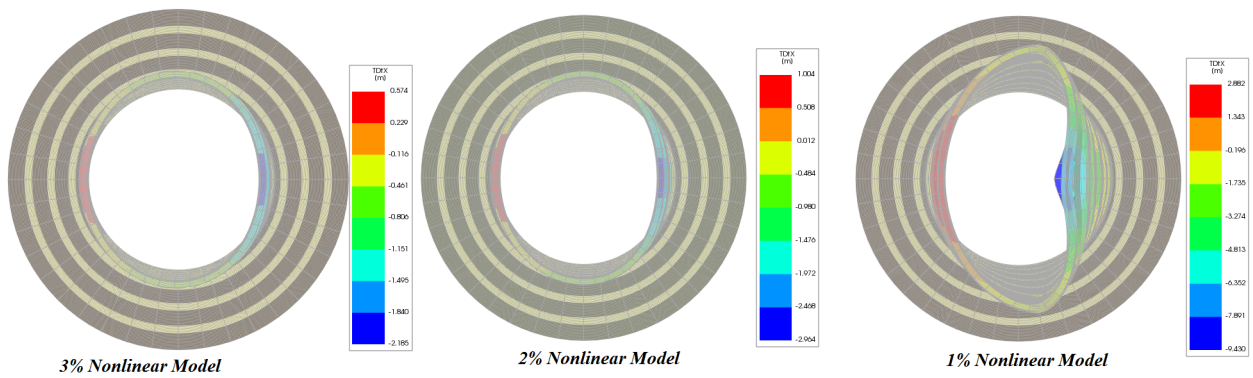


Figure 8.5: The deformed shape for 3%NM(left), 2%NM(middle), 1\$NM(right)

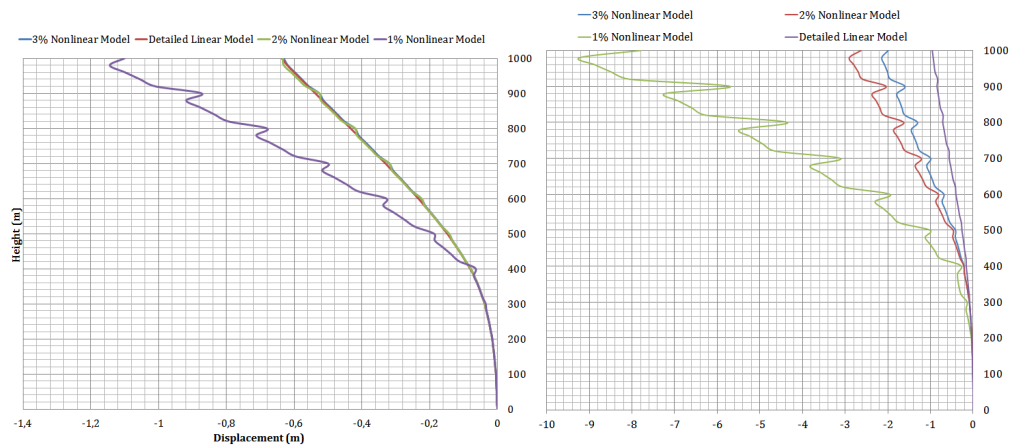


Figure 8.6: the global displacement in the windward direction over height (1D+1W) for model 1% Nonlinear Model, 2% Nonlinear Model, 3% Nonlinear Model (left), The local displacement in the windward direction over height (1D+1W) for model 1% Nonlinear Model, 2% Nonlinear Model, 3% Nonlinear Model (right)

Now concerning the displacement over the height of the tower, the global displacement (left) and local displacement (right) for the three models will be compared with the Detailed Linear Model at the last load step in Figure 8.6. For the global response, large displacement over height is present in 1%NM. The curves for 2%NM and 3%NM coincide with the curve of the Detailed Linear Model. When the model increases its reinforcement ratio to 2%, the structure behaves linearly. Given the bending moment caused by the eccentricity of the stiffening rings and the large horizontal wind load at the top, large protrusions start to appear in 1%NM. A sharp decrease in protrusion size is found for model 2%NM and 3%NM. Furthermore, in the displacement over height, there is one kink found at 1% NM at the throat height. Even though the geometrical matching was done between the lower hyperbolic structure and the upper cone, this geometrical connection will still be a critical area for structural bearing of the wind load. Thanks to the high amount of reinforcement ratio, there is no kink found for 2%NM and 3%NM.

For the local displacement the curves for all three models do not coincide. The displacement and the size of the protrusions decrease with the increase of the reinforcement ratio. The largest displacement of 2%NM model is one-third of that of 1%NM. All models have protrusions on the location of the stiffening rings. There are no huge differences in the size of the protrusions between model 2%NM and 3%NM. The displacement of 3%NM is twice the displacement of DLM. This can be explained in the following. For DLM, the bending moment due to the eccentricity of the stiffening rings only gives a deformation and a certain stress without decreasing the material stiffness. On the contrary, the concrete crack decrease the material stiffness and gives a larger deformation. The local displacement results reveal that 2%NM and 3%NM give a linear global displacement but a large local displacement is observed due to ovalization.

8.1.6. Crack strain distribution

Figure 8.7 gives the crack strain distribution over the whole tower at the extreme inner and outer layer of the shell thickness where the maximum cracks are expected to occur at the last load step. As can be seen, with the increasing reinforcement ratio, the crack distribution on the shell walls decreased dramatically. For 1%NM, the cracks are found over the whole shell wall at the top 600m. For 2%NM, cracks are found at the top 300m at the windward side and the two cross sides due to the ovalization deformation and no crack is found at leeward side. The stiffening rings divided the shell wall into segments. With the reinforcement ratio increasing from 1% to 2%, the maximum crack strain has decreased from 0.059 to 0.011. For 3%NM, the shell walls cracked along the first 100m. The maximum

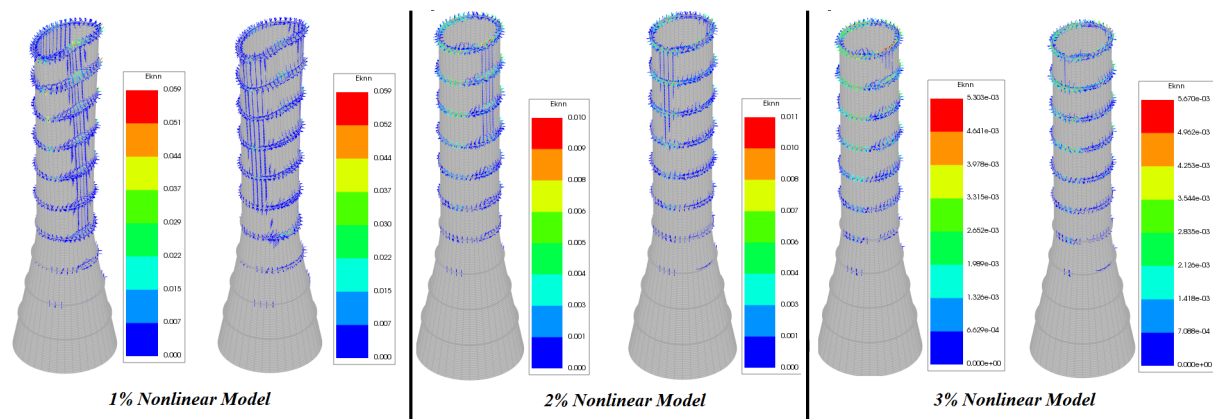


Figure 8.7: The crack strain distribution of the model 1% Nonlinear Model; 2% Nonlinear Model; 3% Nonlinear Model

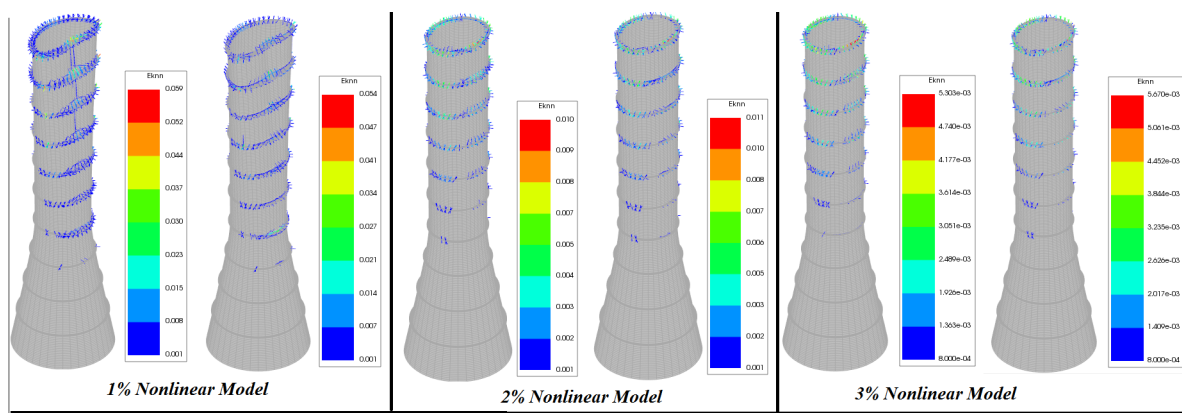


Figure 8.8: The crack strain distribution exceeds the allowable value of the model 1% Nonlinear Model; 2% Nonlinear Model; 3% Nonlinear Model

crack strain is half of that corresponding to 2%NM. The stiffness of the stiffening rings is higher which gives the boundary conditions of each segment a stiffer constraint. The stiffness constraints the deformation of the shell walls and ultimately hinder the ultimate strain development. Even though there is a significant decrease in the crack distribution on the shell walls with increase of the reinforcement, the top eight stiffening rings cracked for all models.

Figure 8.8 gives the crack distribution that exceeds the maximum allowable crack width according to Eurocode at the last load step. Except for 1%NM, all other models have non-allowable cracks located only at the stiffening rings. However, even the shell walls are within the allowable range, the crack control on the stiffening rings should be done since all top seven rings have non-allowable cracks distributed over the whole perimeter. The crack of shell wall segment depends on the stiffness of the constraint by the rings. Note that the crack near the stiffening ring is caused not only by ovalization deformation of the cone shape but also due to the eccentricity of the stiffening ring.

8.1.7. Compression

As mentioned before, the concrete crushing should be avoided in the structure design. If it occurs, a higher concrete class should be used instead of C50/60 or more reinforcement should be added. In the circumferential direction, there is no concrete crushing for 2%NM and 3%NM while all models experienced concrete crushing in meridional direction. Figure 8.9 gives the concrete crushing distribution

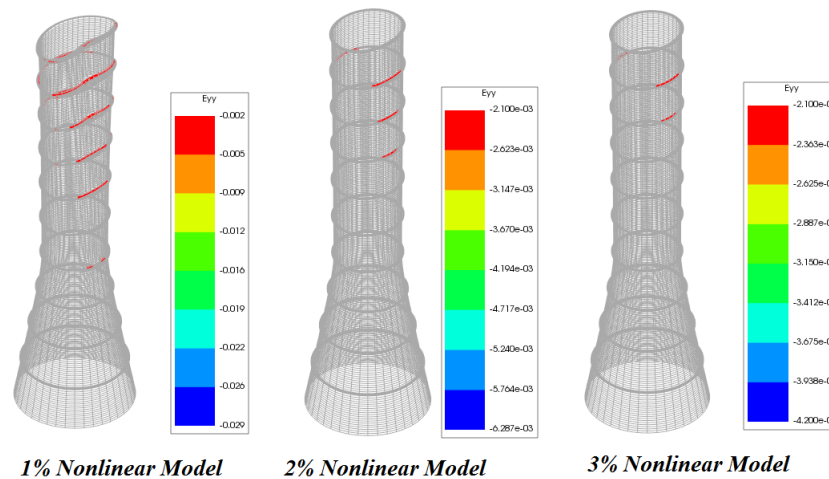


Figure 8.9: The crushed concrete distribution of the tower for 1% Nonlinear Model, 2% Nonlinear Model, 3% Nonlinear Model

in the meridional direction at the last load steps. The large wind load with the additional eccentricity of the rings causes large deformations of the ring which ultimately leads to the concrete crushing. As can be seen, the distribution of the concrete crushing reduced with the increase of the reinforcement ratio, and thus for the maximum compressive strain. The higher reinforcement ratio on the rings gives a greater stiffness and eventually leads to less concrete crushing on the shell walls even if all models have the identical reinforcement ratio setting at the shell walls. For all models, the concrete crushed at the shell walls but not at the rings because the ring is much stiffer and heavier reinforced than the wall.

8.1.8. Reinforcement

Figure 8.10 gives the yielding of the reinforcement distribution in the meridional direction and the circumferential direction. There is a significant reduction of reinforcement yielding with the increase of the reinforcement ratio. Almost no reinforcement yielding is found in 2%NM in the circumferential direction. No reinforcement is yielding at the circumferential direction for 3%NM. Despite increasing the reinforcement ratio till 3%, the reinforcement still yielded in meridional direction at the top three stiffening rings. Since the minimum reinforcement ratio is added to the shell walls, more reinforcement can be embedded in the shell walls near the wall-ring connections.

8.1.9. Stress-resultant

Figure 8.12 shows the tensile stress resultant in meridional direction. As can be seen, the tensile stress resultants in the shell walls are mainly concentrated at the throat height. The wind load tends to lift up the tower from the windward side. Because the shape of the top cone is more flexible than the shape of the hyperbola, their connection can be seen as a boundary constraint of the top cone. The large distributed wind load induced a large bending moment at the constraint of the top cone, a large tension force at windward side and a compression force at leeward side. The area under tension at throat height decreases with increased reinforcement ratio. When the ratio rose to 3%, the whole structural shell wall is under compression in meridional direction.

8.2. Recentered Model

The previous section gives the structural optimization by adding the reinforcement ratio on the rings until the maximum allowable value (3%) for C50/60. There are significant improvements on defor-

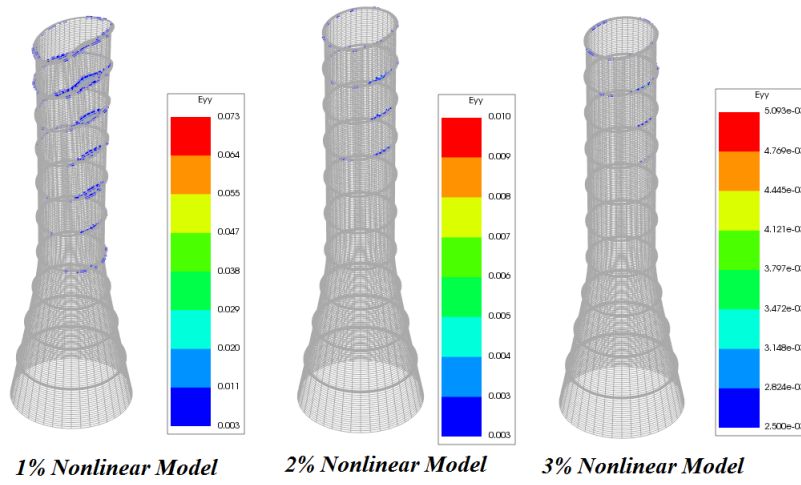


Figure 8.10: The yielding reinforcement distribution in the meridional direction of the model 1% Nonlinear Model, 2% Nonlinear Model, 3% Nonlinear Model

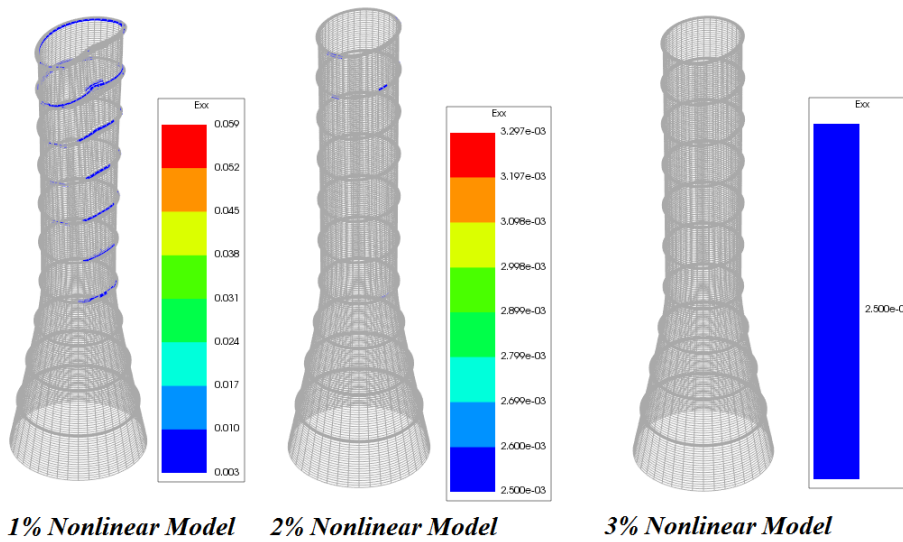


Figure 8.11: The yielding reinforcement distribution in circumferential direction of the model 1% Nonlinear Model, 2% Nonlinear Model, 3% Nonlinear Model

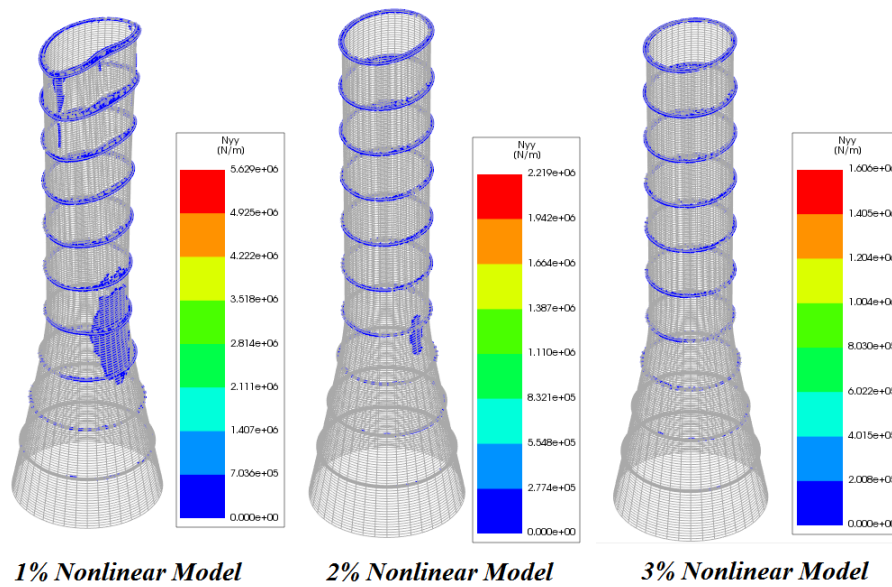


Figure 8.12: The tensile stress resultant in the meridional direction distribution 1% Nonlinear Model, 2% Nonlinear Model, 3% Nonlinear Model

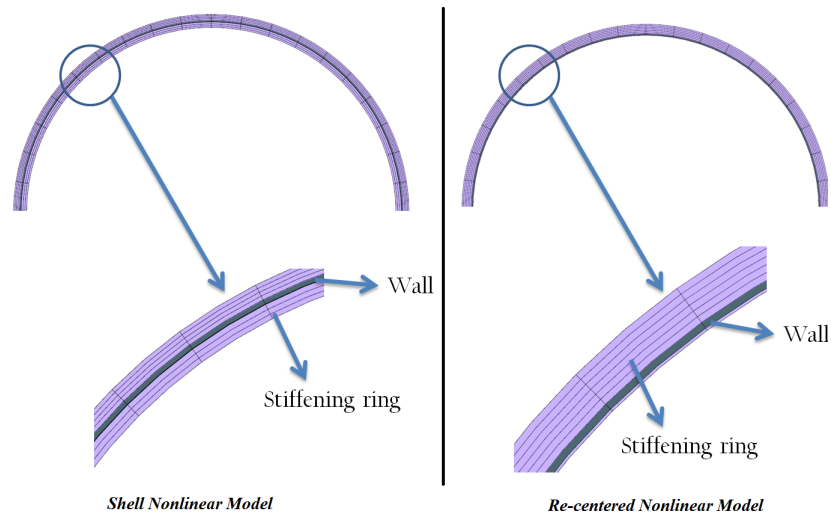


Figure 8.13: The configuration of the ring-wall connection for the Shell Nonlinear Model and Re-centered Nonlinear Model

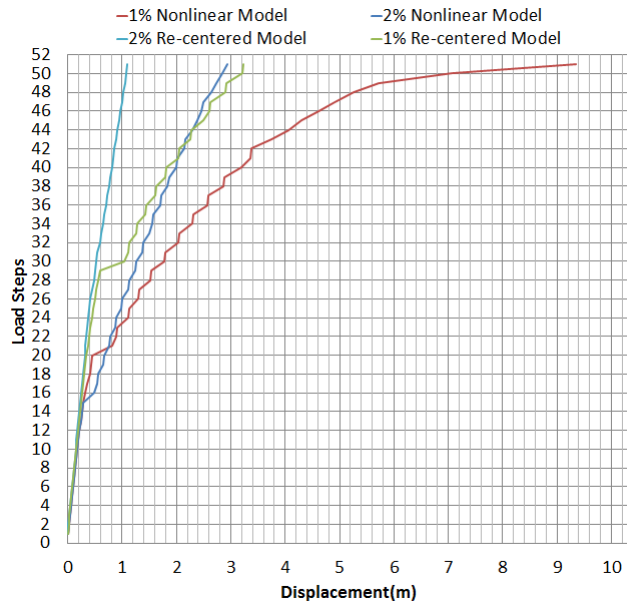


Figure 8.14: Load steps-deflection curve for Recentered model and Shell Nonlinear Model

mation, crack distribution, concrete crushing and reinforcement yielding with the increase of reinforcement ratio. Particularly, a significant increase is found between 1%NM and 2%NM. The concrete crushing and reinforcement yielding still exist for model 2%NM and 3%NM, all located around the stiffening rings. One of the main reasons is the eccentricity of the rings which gives a large deformation at the ring-wall connection. It would be very costly if more reinforcement is added to the shell walls or if the concrete class is replaced by a higher class.

A simple way is to recenter the stiffening ring and diminish the eccentricity. Two models were built and all their stiffening rings mass centers are located at the mid-surface of the shell walls. One model has a reinforcement ratio of 1% on the rings in two directions, named the 1% recentered Nonlinear Model (1%RNM) and the other has a reinforcement ratio of 2% on the stiffening rings in two directions named the 2% Recentered Nonlinear Model (2%RNM). Figure 8.13 gives the configuration of the ring-wall connection of the recentered model and the original model. The nonlinear result will be shown. Except for differences in the geometry of the stiffening rings, the complete model setup is identical to 1%NM for 1%RNM and identical to 2%NM for 2%RNM.

8.2.1. Load steps-displacement curve

Figure 8.15 gives the load step-deflection curve of the two recentered models together with the 2% Nonlinear Model and the 1% Nonlinear Model. This load steps-deflection curve is the displacement of a local point at the windward side at the top of the shell walls. Hence the displacement is a combination of global displacement and local displacement. As can be seen, 2%RNM gives the best performance compared to the three other models. 2%RNM performed almost a linear behavior throughout the complete loading process without any discontinuity. 1%RNM, 1%NM and 2%NM all give a geometrical discontinuity at a certain load step and the stiffness of the structure decreased after the discontinuity. Three kinks are observed at the top cone cross section for these three models.

1%RNM and 1%NM are now being compared. The two curves both develop linearly at the beginning. However the discontinuity occurred much later for the recentered model, Load step 29, compared to load step 20 for 1%NM. Due to the high loading level, a larger displacement at the point of discontinuity is obtained for 1%RNM. Even though two models have the same amount of reinforcement, the structural stiffness of 1%RNM is higher than that of 1%NM after the discontinuity. Consequently,

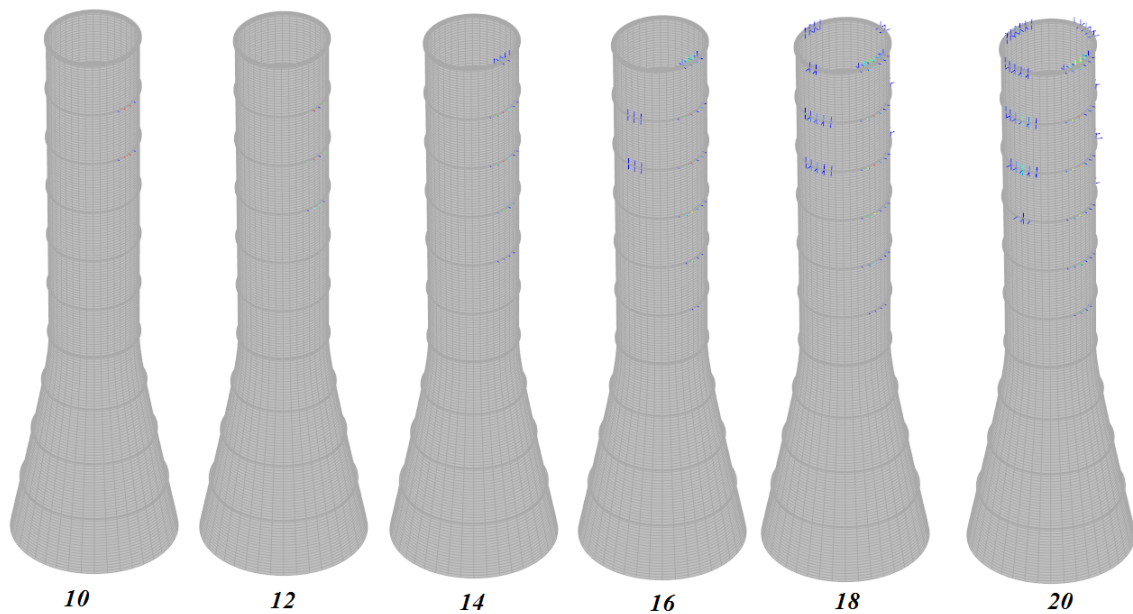


Figure 8.15: The crack initiation of 1% Recentered Nonlinear Model from load step 10 to 20.

1%NM leads to structural failure but 1%RNM did not. For 2%RNM it is observed that the structure is strong enough that the discontinuity did not occur until the last load steps and the structure still performed almost linearly.

8.2.2. Maximum principal strain

It was known, due to the eccentricity of the rings, that 1%NM model experiences crack both at the shell walls and the stiffening rings under self-weight. No crack is observed in 1%RNM until load step 10 with load factor $1.0D+0.18W$. Figure 8.15 gives the crack developing pattern of the 1% Recentered Nonlinear Model. Without eccentricity the crack developing pattern is different from the original design model. Unlike the 1% Nonlinear Model whose crack starts from the whole perimeter of the stiffening rings and the shell walls, the crack starts from windward side first, following the two cross sides and ultimately the leeward side. The crack is not distributed over the whole perimeter for the recentered model. For the 2% Recentered Nonlinear Model, the crack development shows a similar pattern as 1%RNM but with a slower developing speed. Crack initiation starts at load step 10 indicating a slow development of tensile strain. This can explain why the kink occurs at a higher loading level for 1%RNM than that for 1%NM.

Figure 8.16 gives the maximum principal strain development until the last load step. The curves have certain similarities compared to load-step deflection curve: 1) The discontinuities are also observed in the maximum principal strain development curve. 2) There is an increase in crack development after the discontinuities. At the discontinuities for 1%NM, 2%NM and 1%RNM, the maximum principal strain crosses the ultimate tensile strain of the shell walls. However, it should be mentioned that for 2%RNM, the curve development shows a small discontinuity which is not the case in the load-step displacement curve. This discontinuity located at the maximum principal strain exceeds the ultimate strain of the shell walls. From the continuous load-step displacement curve it can be seen that this jump in maximum principal strain did not lead to a large deformation of the structure. The stiffening rings are still able to keep the original cross-section of the structure without kinks.

For the model with same reinforcement ratios, their maximum principal strain development pattern after it exceeds the ultimate strain is rather similar. However, the load-step displacement curves

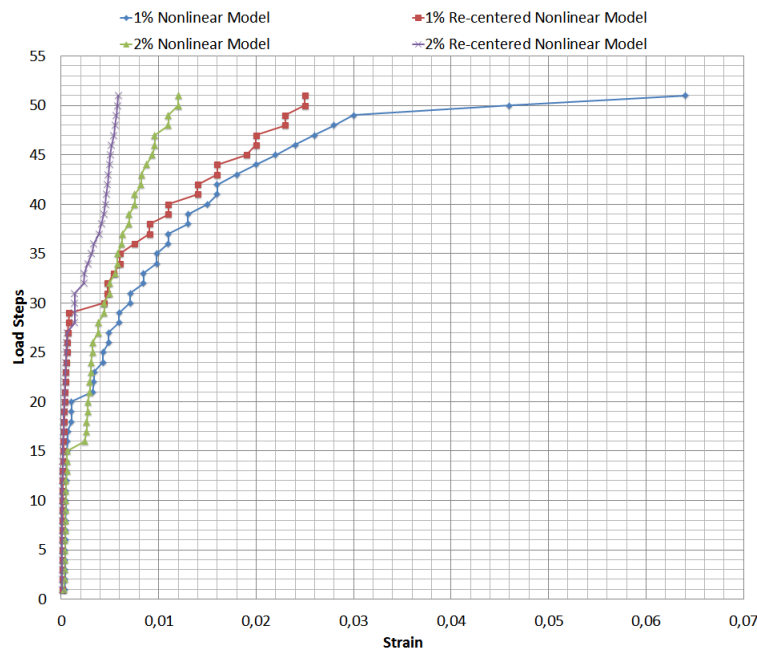


Figure 8.16: Principal strain development for 1%RNM, 2%RNM, 1%NM, 2%NM

after the discontinuity are very different between model 2%NM and 2%RNM. The structural behavior highly depends on whether the failure mechanism occurs. Once three kinks occur at the top cone, the stiffness of the structure will be decreased significantly.

8.2.3. Deformation at the last load step

Figure 8.17 gives the deformed shape of 1%RNM and 2%RNM, combined with their displacement distribution in windward direction. As can be noticed, the maximum displacement of 1%RNM and 2%RNM are around 3m and 1m respectively. According to the Code of Practice for Structural use of Concrete Department (2013), the maximum allowable displacement at the top of the structure is 1/500th of the height, which is 2m for the SUT. 2%NM satisfied the displacement requirement in serviceability limit state. 1%RNM shows a larger deformed ovalization compared to 2%RNM. The maximum displacement of 1%RNM is 3.2m which is one third of the model 1%RNM. A three times improvement is obtained by re-centering the stiffening rings without adding more reinforcement ratio. 2%RNM shows an almost perfect circular cross-section

Figure 8.18 gives the global displacement of the recentered models over the whole height and these curves will be compared with DLM, 1%NM and 2%NM. Except for 1%NM model, all other curves overlap with DLM. With 1% reinforcement ratio on the stiffening rings, the recentered model shows a linear global behavior. However, even though the reinforcement ratio has increased to 2%, no reduction on global displacement is found.

Figure 8.19 gives the local displacement of the recentered models. 1%RNM gives similar displacement as 2%NM. Note that although 2%RNM gives better local displacement than DLM, the global displacement has no significant improvement. The deformation of the cross-section at the top cone of 2%RNM is expected to deform less than DLM. However, even though 2%RNM has reduced displacement, the diminutive protrusions are still found. These protrusions are induced by the wind load pushing the wall inward of the tower and the wall being more flexible than the heavily reinforced stiffening ring. The protrusions can be minimized by increasing the reinforcement ratio at the shell walls near the ring. Figure 8.19 also shows with the same amount of reinforcement, the maximum

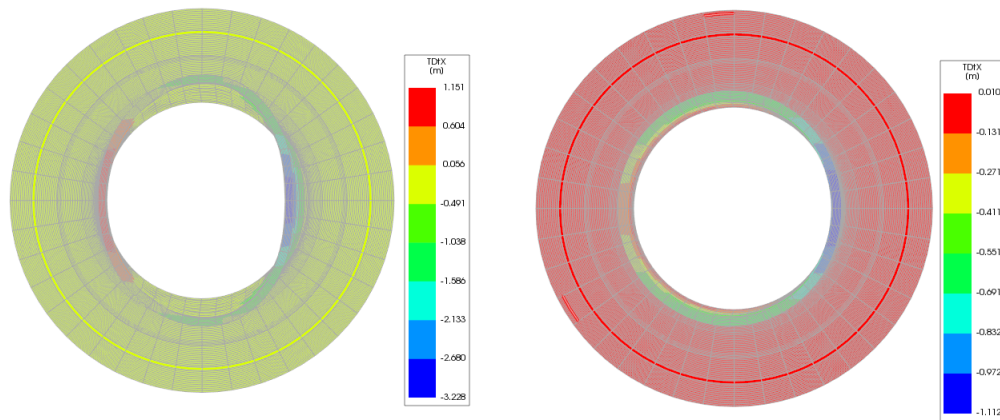


Figure 8.17: Topview of 1%RNM(left) and 2%RNM(right) at the last load step (1D+1W)

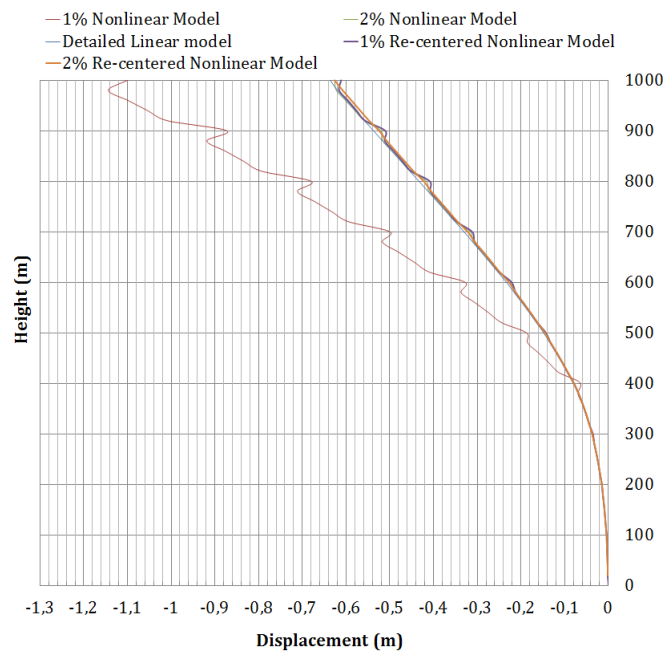


Figure 8.18: The global displacement of in the windward direction 1%RNM, 2%RNM, 1%NM, 2%NM, DLM at the last load step(1D+1W)

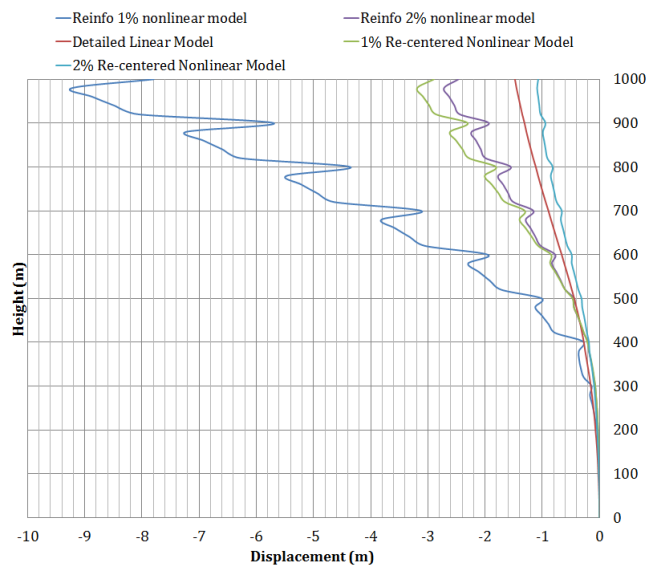


Figure 8.19: The local displacement of 1%RNM, 2%RNM, 1%NM, 2%NM, DLM at the last load step(1D+1W)

displacement of 1%RNM is one-third of 1%NM.

8.2.4. Crack distribution at the discontinuity

Although 2%RNM did not give a structural discontinuity, it still shows a slight jump on maximum principal strain development when the model crosses the ultimate strain. For 2%RNM, this jump will be compared with 1%RNM which also experience the jump but also with a failure mechanism on the cross section. Figure 8.20 shows the deformed shape of 1%RNM and 2%RNM before and after the jump. Three kinks are observed after the discontinuity for 1%RNM. The windward side of the shell walls are pushed into the tower and has been flattened. The two cross-sides were pushed outward. These three sides show large strain concentrations. Before the jump, the strain concentrated at the windward and leeward side with a smooth pattern, after the jump, the strain concentrated both at the windward, the leeward, and the two cross sides. 2%RNM shows a much smaller deformation after the jump than for 1%RNM. The deformed shape stays the same before the jump without the strain concentration at the two cross sides. The shape remains circular. For 2%RNM, the maximum strain is concentrated on the windward side and leeward side before the tower cross the maximum ultimate strain, while after the cross, the shape of the tower remain almost circular and there is no sudden change in shape. As stated before, 2%RNM did not experience the structural failure mechanism even though the maximum principal strain crosses the ultimate tensile strain. 2%RNM did not have a failure mechanism on the cross-section until the last load steps.

8.2.5. Crack distribution at the last load step

Figure 8.21 gives the crack distribution of 1%RNM and 2%RNM. For 1%RNM, at areas where the shell walls cracked, the crack strain is in all cases within the allowable range. All unacceptable cracks are located at the stiffening rings. The maximum crack strain is 0.015. As calculated before, the crack spacing for the shell wall is 476mm, and thus the maximum crack width of the structure is 7mm. Due to the recentered rings, the maximum crack width has been reduced by 10mm compared to 1%NM. However, it is apparent that the crack width grows to a very undesired value since it is 17 times larger than the maximum requirement.

For 2%RNM, the maximum crack strain is 0.0023 which gives the maximum crack width of 1.1mm.

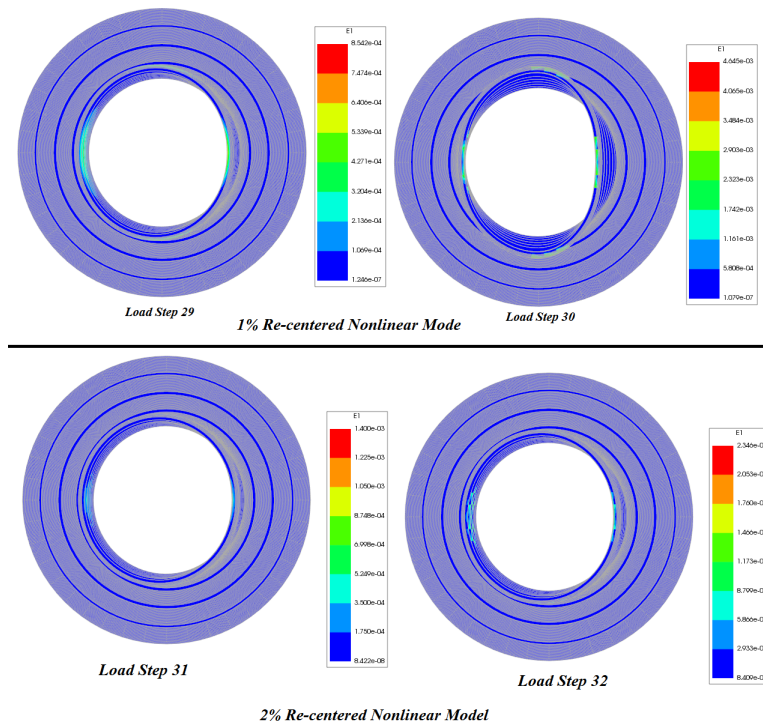


Figure 8.20: The principal strain distribution of 1%RNM and 2%RNM before and after the discontinuity

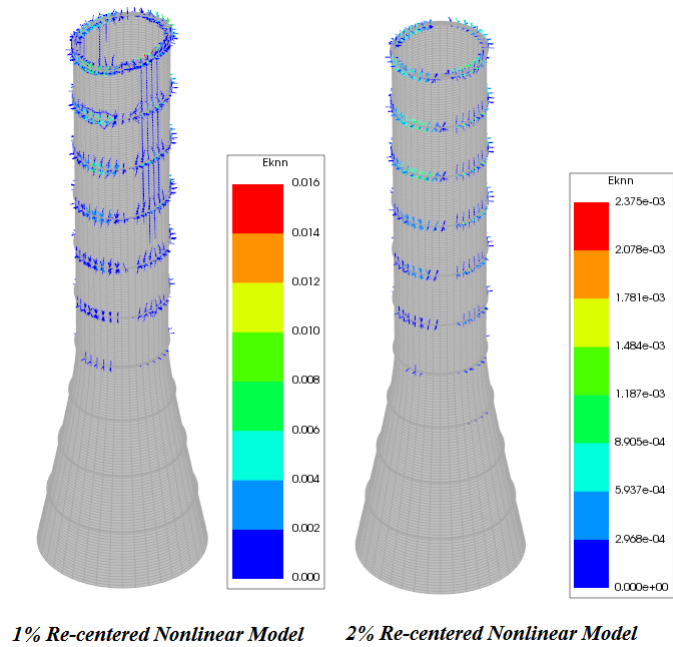


Figure 8.21: The crack strain distribution of 1%RNM and 2%RNM at the last load step (1D+1W)

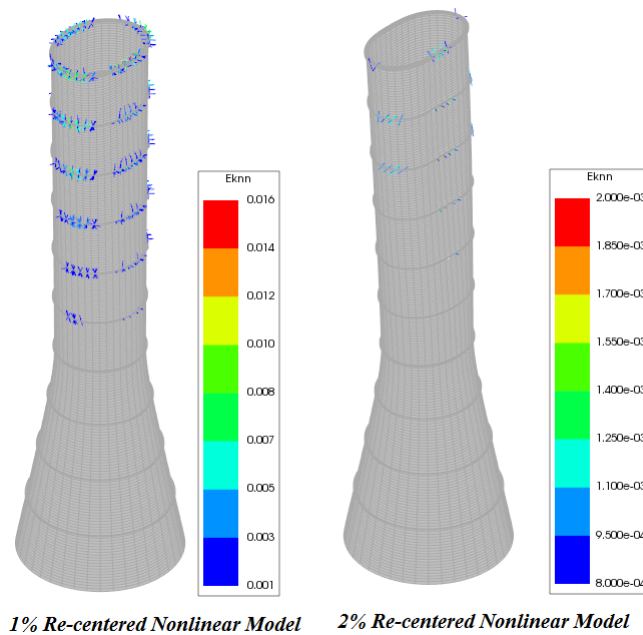


Figure 8.22: The crack strain distribution exceeding the allowable value of 1%RNM and 2%RNM at the last load step (1D+1W))

The increase in reinforcement ratio reduced the crack width significantly. the shell walls are now in a un-cracked stage and cracks only occurred at the stiffening rings.

For the recentered model, considering the overall crack distribution on the ring, the crack is not distributed over the whole perimeter of the ring but at the windward side, the leeward side and the two cross sides. Figure 8.22 shows the crack that exceeds the maximum allowable crack strain(0.0008). For 1%RNM, the non-allowable crack is distributed over the first six stiffening rings but not over the whole perimeter. For 2%RNM, the non-allowable crack is distributed over a few locations with a marginal magnitude at the top five stiffening rings.

8.2.6. Concrete crushing and reinforcement yielding

No concrete crushing is observed in all recentered models, even though 1%RNM gives a larger displacement than 2%NM. This is because without the extra bending moment acting on the shell walls, the concrete is still within the linear stage under static wind load. With recentered ring geometry, concrete class C50/60 is sufficient for the structural design even with reinforcement ratio of 1% on the ring. However, 1%RNM shows the yielding of reinforcement in both circumferential direction and the meridional direction. The yielding distribution is shown in Figure 8.23. Thanks to the increase of the reinforcement ratio, no reinforcement yielding is found in 2%RNM. Large displacement on the cross-section at the top cone is one of the factors causing the reinforcement yielding. However, it is not the cause for the concrete crushing.

8.3. Top ring deformation

The nonlinear analysis in this thesis research is developed and optimized step by step. However, a more systematic comparison was beneficial for understanding the changing of structural behavior from a weak to a strong state. Figure 8.24 to Figure 8.27 show the principal strain distribution of the top ring and the shell walls before and after the discontinuity at the windward side. Their deformed shapes are 30 times the absolute value. The principal strain at the integration point is calculated from

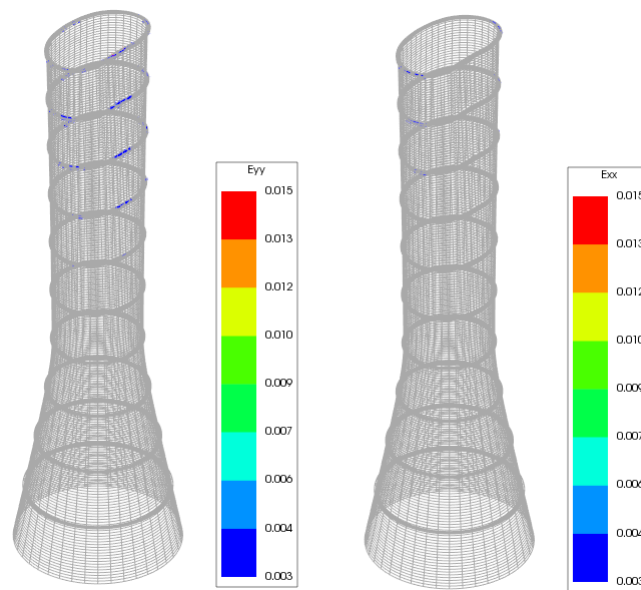


Figure 8.23: Principal strain development for 1%RNM, 2%RNM, 1%NM, 2%NM

the force equilibrium, at the node by quadratic interpolation. The result is not averaged.

8.3.1. Top ring deformation of 1%NM

Figure 8.24 shows the top ring deformation of 1%NM. **Before kink**

- The strain distribution is smooth at the rings.
- The maximum strain is located at the ring-wall connection over the whole perimeter due to the eccentricity of the ring.
- The cross-section is almost a circular shape.
- The outer sides of the ring deflects downwards, the inner sides of the ring deflects upwards.

After kink

- The strain on the stiffening ring is not continuous due to the large crack opening of the ring.
- The maximum strain is located at the ring-wall connection due to the eccentricity over the whole perimeter.
- A significant downward deformation of the outer side of the ring and uplift of the inner side of the ring.
- The ring elongates in the transverse direction which significantly activates the transverse stiffness.
- The windward side of the tower is pushed inward and is flattened.

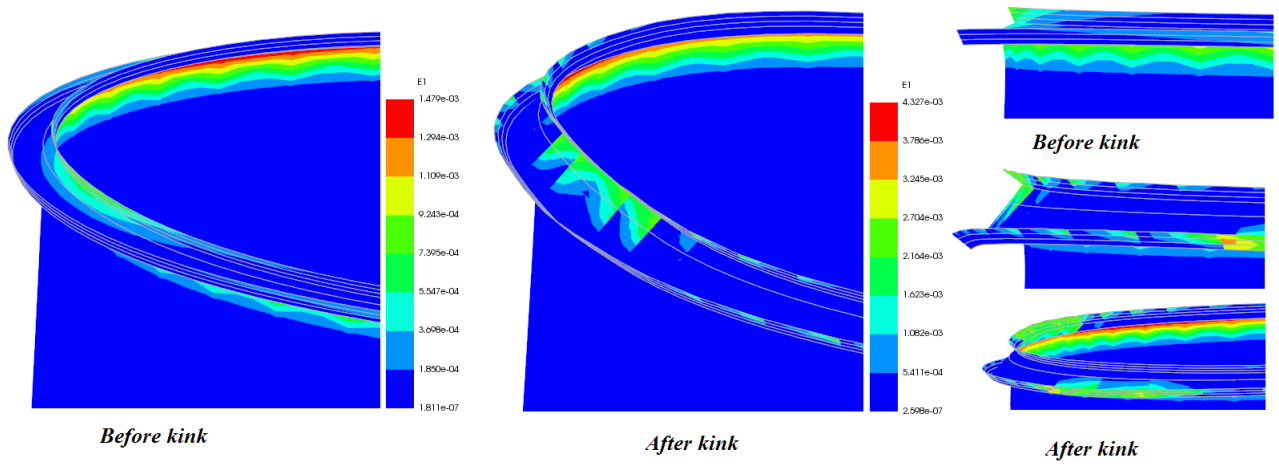


Figure 8.24: The principal strain distribution of the top ring for 1% Nonlinear Model

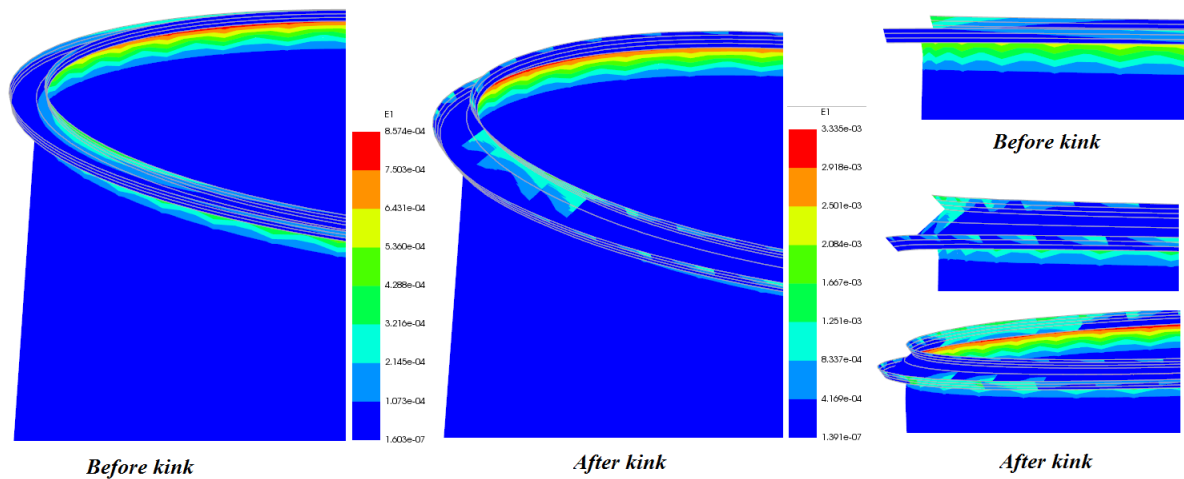


Figure 8.25: The principal strain distribution of top ring for 2% Nonlinear Model

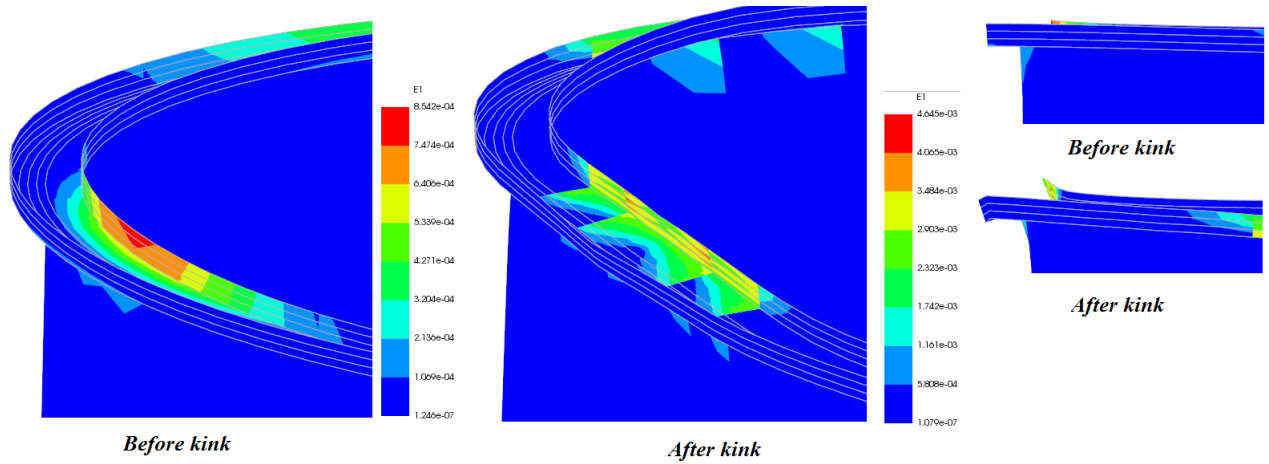


Figure 8.26: The principal strain distribution of top ring for 1% Recentered Nonlinear Model

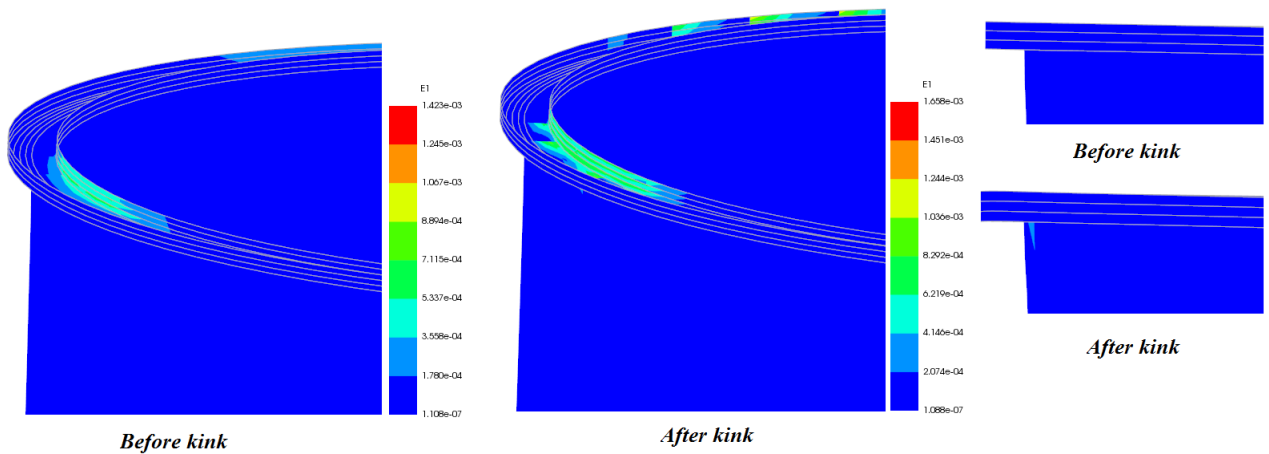


Figure 8.27: The principal strain distribution of top ring for 2% Recentered Nonlinear Model

8.3.2. Top ring deformation of 2%NM

Figure 8.25 shows the top ring deformation of 2%NM **Before kink**

- The strain distribution is smooth and the cross-section is almost a circular shape.
- The maximum strain is located at the ring-wall connection.
- Due to the eccentricity of the stiffening ring the outer ring deforms downward and the inner ring is uplifted with marginal magnitude.

After kink

- The strain is not continuous because of the large crack opening.
- The maximum strain is still located at the ring-wall connection. The increase of the reinforcement ratio has no significant influence on reducing the large strain at the ring-wall connection.
- The large downward deformation at the outer side of the ring and the large uplift of the inner side of the ring but with less magnitude than that for 1%NM.
- The ring is elongated in the transverse direction with less magnitude than that of 1%NM.
- The windward side of the tower is flattened with less magnitude than that of 1%NM

8.3.3. Top ring deformation of 1%RNM

Figure 8.26 shows the top ring deformation of 1%RNM **Before kink**

- The strain is continuously distributed at the ring. The shape of the top cone is almost circular.
- The maximum strain located at the vertical section of the inner side of the ring. No large strain is found at the ring-wall connection.
- No downward or uplift deformation of the ring.

After kink

- The strain is not continuously distributed due to the large crack opening.
- The maximum strain is located in the ring at windward side. No large strain is found at the wall-ring connection.
- The cross-section is not a circular shape anymore, the windward side of the tower is pushed inward and is flattened.
- The ring is elongated in the transverse direction.
- A large deformation of the ring is found but no downward and uplift deflection of the ring occurs.

8.3.4. Top ring deformation 2%RNM

8.27 shows the top ring deformation of 2%RNM. **Before kink**

- The strain distribution is smooth on the ring with an almost circular shape.
- The maximum strain is not located at the top ring, but at the intermediate rings, the inner part of the ring at windward side.
- The ring has no downward or uplift deformation.

After kink

- This model has no kink on the cross-section but it does have a discontinuity on maximum strain development.
- The ring remains an almost circular shape. The strain is not continuous because of the crack opening.
- The maximum strain is not located at the top ring but at the inner side of the intermediate rings at the windward side of the tower.
- The ring has no large elongation because there is no flattened shape of the tower.

8.3.5. Conclusions

1%NM and 2%NM give the same failure behavior and the increase of the reinforcement ratio does help the structure to obtain a smaller failure magnitude.

The recentered ring models provide a different failure mechanism compared to 1%NM and 2%NM. The increase of the stiffness of the ring gives an essential improvement on structural behavior. The stiffening rings give a constraint on each shell wall segment. The large strain at the ring-wall connection immediately decreases the contribution of the stiffness rings on the shell walls, reducing the constraining effect of the stiffness rings. The decreased contribution of the constraint is caused by the weak and cracked wall-shell connection. The kink highly depends on the stiffness of the ring. If the ring-wall connection is weakened, the high reinforcement ratio of the ring will not give any useful contribution. The stiffness of the top stiffening ring plays an important role on the structural behavior.

8.4. Conclusions

This chapter has shown a few attempts to improve the overall structural behavior. The physical non-linear analysis, shown in the previous chapter, revealed the critical area of the structure under the wind load, hence the optimization can be directly to the problem area. Without try and error, the structure shows significant improvement. By adding more reinforcement, the structure gives less deformation, improved cracking behavior and improved reinforcements yielding behavior. The eccentricity caused large cracking and crushing on the concrete and decreases overall structure stiffness. Hence there is a limitation of increasing reinforcement ratio as a method of improving the structural behavior. By recentering the stiffening rings the result show a significant improvement without increasing the reinforcement ratio. The failure mechanism did not occur for the recentered model with reinforcement ratio of 2% while all other models experienced this mechanism together with a sudden decrease in structural stiffness. The deflection is within the allowable range. Without the extra bending moment caused by the eccentricity of the stiffening ring, the structure gives almost a linear behavior until the last load step. Appendix E shows the structural performance of 2%NM under 1D+2W.

9

Discussion

This chapter will give a short discussion and conclusion related to the nonlinear analysis result on each chapter

9.1. Geometry of the solar updraft tower

This research project uses the original design from Krätzig&Partner with minor modification during the optimization process. Hyperboloid shape at the bottom performs superior on the load bearing resistance as well as the stability compared to the upper cone. While even with geometrical matching, the throat where connecting the upper cone and lower hyperbola can be problematic due to the geometrical discontinuity. But with sufficient stiffness of the upper cone, the throat height will be on the safe side, because in that way the ovalization failure mechanism will not occur. Increasing the wall thickness of the upper cone or increasing the stiffness of stiffening ring can be the ways to reduce the ovalizing deformation of the top cone. The stiffening ring geometry and its position profoundly influence the structure behavior and thus determine the amount of material use. Recentering the stiffening rings give significant improvement on structural response. However, the influence of airflow and power output should be further investigated.

9.2. Load on the solar updraft tower

The top of the tower near the boundary layers is found to experience large deformation due to the high wind pressure. The wind speed near the boundary layer is large because it is not influenced by the earth roughness. The means hour wind speed of the selected location plays the most important role in determining the wind load magnitude for 1000m solar updraft tower. An outer surface roughness could alter the pressure distribution and could prevent the upper cone from ovalizing. A smooth surface will give a rather large suction force at two sides of the tower, which can easily cause ovalization.

9.3. Finite element modeling

One or two proper models by considering many model setup possibilities were built. In order to do the nonlinear analysis, detailing the stiffening rings is necessary. With the precise geometry of the stiffening rings modeling, the model is more sensitive to meshing density. Comparing the eigenvalue of each model, a proper meshing density and proper element types were found. Intermediate meshing with the element size of 5m 5m sufficient for modeling the shell wall, but the stiffening rings should be refined due to the detailing of the reinforcement. The element type for the stiffening rings can be beam element and curved shell element, and their differences could not be seen in eigenvalue analysis

but it does give significant differences in nonlinear analysis.

9.4. Linear analysis

The eigenvalue analysis and the linear analysis verification reveal an accurate model setup. On top of an accurate linear model, the geometry of the stiffening rings has changed from the simple rectangular cross-section located at the mid-surface of concrete shell wall to a detailed geometry with a certain eccentricity. The eigenvalue analysis has shown that the stiffening rings has the impact on the shell-like vibration. In the later nonlinear analysis, the stiffer stiffening rings also reduce the shell deformation such as ovalizing significantly. The precise geometry of the stiffening rings gives a higher stiffness compared to rectangular cross-section ring geometry, but the eccentricity of the ring cause massive concrete cracking and crushing in the nonlinear analysis. The accuracy of the model should be sufficient before conducting the nonlinear analysis.

9.5. Nonlinear Material Model

Before conducting physical nonlinear analysis, the reinforced concrete behavior should be understood. Explanation on the material model is given. The total strain rotating crack model provides a robust behavior so that the structure is able to experience massive concrete cracking and crushing under large strain value without divergence. The concrete nonlinear compressive behavior is found to be necessary because the eccentricity of stiffening ring led to the crushing of the concrete even the model is designed with a maximum reinforcement ratio at the stiffening rings. Furthermore, the compression crushing occurred in the material nonlinear analysis concluded that it is essential to add the lateral cracking and lateral confinement into the concrete compressive model. The tension stiffening theory gives a more accurate modeling on reinforced concrete with different reinforcement ratios and it has a significant impact on structural behavior at low loading level and a minor impact on the large loading level. The embedded reinforcement needs the reinforcement properties in one direction, which is a simple and effective way for modeling reinforced concrete.

9.6. Material Nonlinear Analysis

The material nonlinear analysis compared three models. The result reveals that the curved shell element for modeling the stiffening rings is needed in order to add the transverse reinforcement. Tension on the throat height is found in the nonlinear analysis which is not the case for the linear analysis. In the linear analysis, no tension force is found at the throat height. The shell deformation is proved to be large if the stiffness of the upper cone is not sufficient. Eigenvalue analysis shows identical results between the model with the stiffening rings modeled with beam element and the curved shell element. In the nonlinear analysis, the one with curved shell element shows a stiffer behavior than the beam due to the additional transverse reinforcement. Curve shell element for modeling stiffening ring proved to be the proper choice for the material analysis. Tension on the windward side is found due to the large ovalization deformation on the top cone. Concrete cracked under static self-weight due to the eccentricity of the stiffening ring gives a bending moment on the shell walls. Large deformation is found at the ring and the ring-wall connection under wind action.

9.7. Model Optimisation

Increasing reinforcement ratio and re-centering the stiffening ring are the two attempts to improve the structural behavior. A model with 2% reinforcement ratio at the ring and with re-centered rings geometry leads to significant improvements. It might not be the most optimal design while it does shows the problem area. Increasing the reinforcement ratio only gives a stiffer stiffening rings while the ring-wall connection still experiences large crack due to the eccentricity of the ring. However, the structure stiffness does increase with the increment of reinforcement ratio which leads to a better structural performance. The low ultimate strain value gives an early cross-section failure mechanism

even with high reinforcement ratio. This demonstrates that the cracked ring-wall connection did not give enough constraint on the shell walls, even with a high stiffness of the ring, the failure mechanism will still occur. The maximum strain is located at the connection but not the ring for original design model. Without cross-sectional failure mechanism, the structure shows almost a linear behavior to the last load step. The ovalization deformation is half of the value of the linear model with the original design. No concrete crushing and reinforcement yielding are found for the last optimized model. No tension force is found at the throat height, not concrete cracking is found on the concrete wall. The failure kinks on the top cone cross-section is no longer a threat. It is believed by the author that the stiffness of the top stiffening ring contributes to control the failure mechanism and its transverse reinforcement on the top stiffening ring have the potential the flattened deformation at the windward side of the tower.

10

Conclusions and recommendations

In this chapter the conclusion of this thesis research project will be given and the recommendations on the future research

10.1. Conclusions

The research project has been carried out in order to find the realistic structural behavior of the solar updraft tower under static wind actions with nonlinear material behavior. The effort performed also goes in the direction of improving the structural response with minimum modification on the geometry, which can hopefully contribute in a useful way in the design phase of the solar updraft tower. A set of models were built and its load steps-deflection curves are shown in Figure 10.1. Some conclusions related to the nonlinear analysis are drawn below.

- In a physical non-linear analysis of the solar updraft tower, curved shell elements are suitable for modeling the shell walls and the stiffening rings. Beam elements are not sufficient due to the lack of transverse stiffness.
- For the reinforced concrete solar updraft tower originally designed by Krätzig & Partner, a minimum reinforcement ratio in the shell walls and 1% reinforcement ratio in the longitudinal and transverse direction in the stiffening rings give a large ovalization failure at the upper cone under the serviceability limit state. This is caused by a low reinforcement ratio in the stiffening rings which diminished their stiffening ability. In addition, the eccentricity of the stiffening rings caused a large bending moment which weakened the ring-wall connections.
- A weak upper cone will experience an ovalization failure mechanism which leads to a sudden decrease of the stiffness of SUT. The structure with decreased stiffness leads to large concrete cracking, crushing and reinforcement yielding. This failure mechanism can be avoided by the stiffening rings with sufficient stiffness and a strong ring-wall connection.
- The eccentricity of the stiffening rings causes bending failure at the ring-wall connection which decreases the overall contribution of the stiffening rings on the structural behavior of the SUT. It can not be solved only by adding more reinforcement to the stiffening rings. The bending failure at the ring-wall connection can be solved by recentering or prestressing the stiffening rings.
- 2% reinforcement ratio both in the longitudinal and the transverse direction is a feasible amount for the stiffening rings which gives a considerable improvement in structural behavior compared to the model with 1%. Increasing to 3% gives a minor improvement. The concrete quality is difficult to control with a high reinforcement ratio, which might even decrease the structural performance in reality.

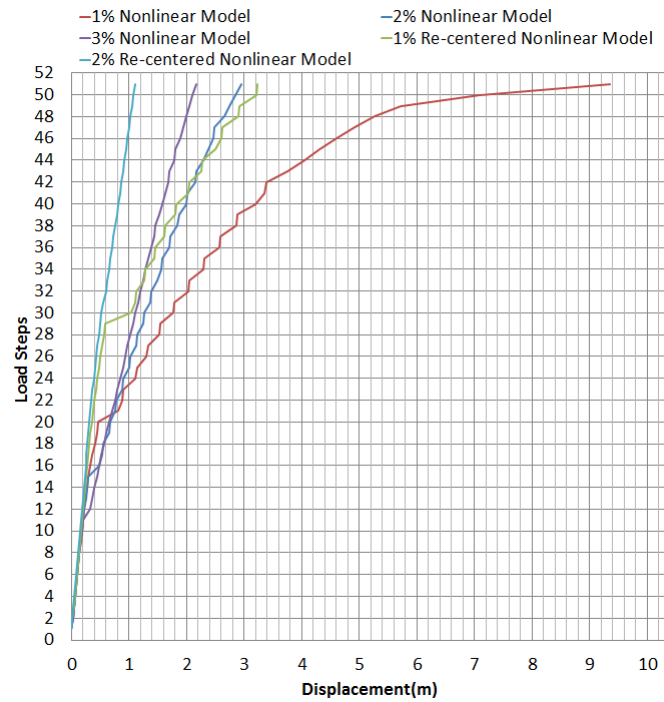


Figure 10.1: Load steps-deflection curve

- The influence of tension stiffening on the SUT structural behavior is high at a low loading level and becomes lower at a high loading level.

Based on the knowledge acquired from the nonlinear analysis, an improved model is found, with 2% reinforcement ratio on the recentered stiffening rings. Some conclusion related to the improved model are drawn below.

- A sufficient reinforcement ratio gives a high stiffness of the stiffening rings and this high stiffness can be fully utilized to constrain the shell walls by recentering the geometry of the stiffening rings.
- With a sufficient reinforcement ratio and recentered geometry of the stiffening rings, the upper cone ovalization failure mechanism vanishes and gives a linear structural behavior in the serviceability limit state. No concrete crushing and reinforcement yielding are found. The influence on the airflow and the power output should be further investigated.
- The improved model has a maximum displacement which is lower than the linear model with the original geometry from Krätzig & Partner. The model meets the requirement on the maximum allowable displacement in the serviceability limit state but an excessive crack width of 1.1mm is found in the stiffening rings which should be further improved. However, the shell walls and the stiffening rings were modeled with one layer reinforcement located at the mid-surface of the shell. In reality, two reinforcement layers with a 40mm concrete over will be built and a smaller crack width is expected.

10.2. Recommendations

This research project focus on the physical nonlinear behavior of the solar updraft towers under static wind action, much further research is needed before it can be built. Some interesting research direc-

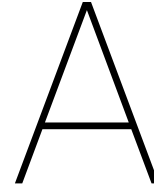
tions are found during the current research by the author. Five topics are of the most interest.

- **Temperature effect.** In this research, only the dead load and static wind load is considered. The temperature effect was not taken into account. Temperature differences may cause cracks on the shell wall due to structural fixation, which could reduce the stiffness of the structure and finally decrease the first and second natural frequency of the SUT. The temperature load in SUT includes the temperature rise in the collector, operational force the action of the heated air, asymmetrical due to ambient air temperature, non-asymmetrical due to solar irradiation of the tower shell. A nonlinear model can be done including all these temperature effects, the wind load, and the self-weight.
- **Plastic buckling analysis.** Thin shell structure is high sensitive to the shell buckling instabilities under dead load, wind load, and wind suction. The buckling strength is lower if the material of the member is stressed beyond the elastic material range. The cracking of the concrete might give a lower stiffness of the structure so as the buckling strength. The plastic buckling analysis might of interest to research.
- **The transient analysis.** The natural frequency of the solar updraft tower is rather low, which is close to the frequency of gust wind fluctuation. Along-wind oscillation is vulnerable to occur. Wind load is rather random and unpredictable; it might be interesting to investigate the structure under stochastic wind action with material non-linearity. A transient analysis is a dynamic analysis with time integration. Geometrical or physical nonlinear analysis or both can be added to the transient response.
- **Detail optimization.** With the reference of current research result, it reveals that the stiffening rings gives a significant impact on the structural response. But the shell walls thickness, the shape of the tower, the concrete class, the reinforcement of the shell walls and the detailed foundation of structure also can influence the overall structural behavior and they were not considered in this research project. A more detailed structural optimization should be done including all these aspects mentioned above. By detailing the structural optimization, less material can be used.
- **Detailed design of the stiffening rings.** From this research project, it was found that the original design from Krätzig & Partner gives an eccentricity of the stiffening rings which lead to a relatively weak structural behavior. This eccentricity is designed mainly for keeping the airflow and power output because the long stiffening ring inside the shell walls will interrupt the airflow and thus influence the power output. Some solutions can be done, such as designing the prestressed tendon to balance the load and to reduce the bending moment acting on the ring-wall connections. There might be other better solutions. A detailed design of the stiffening ring to increase the structural behavior without interrupting the air flow can be further researched.

Bibliography

- Goldack Arndt, Bergermann Schlaich, and Partner Solar. Natural frequencies and mode shapes of towers for solar updraft power plants. 79:104–113, 2011.
- ASCE7. *ASCE7:Minimum Design Loads for Building and Other Structures*, volume 4. 2013.
- K J Bathe. *The Finite Element Analysis of Shells*. Number 2010937756. Springer, second edition edition, 2011. ISBN 9783642164071.
- Schlaich Bergermann. Solar Updraft Tower. *Schlich Bergermann Solar GmbH, Stuttgart*, 2011.
- Le Bourget. *Solar Energy*. 2013. ISBN 978-1-4614-5805-0. doi: 10.1007/978-1-4614-5806-7. URL <http://link.springer.com/10.1007/978-1-4614-5806-7>.
- Hong Kong Buildings Departement. Code of Practice for Structural Use of Concrete. *Technical report*, 2013.
- DIANA. *User Manual Element Library*. 2016.
- C.V. Dyk. A methodology for Radical Innovation-illustrated dy application to a radical Civil Engineering structure. *PhD thesis*, 2008.
- Steven van Eck, Jeroen Coenders, and Rob Doomen. Solar updraft tower – structural optimisation under dynamic wind action. (August), 2015.
- EN1991-1-4. Eurocode 1: Actions on structures-part 1-4: General actions wind actions. 4(2005), 2011.
- EN1992-1-1. Eurocode 2: Design of concrete structures - part 1-1 general rules and rules for building. 4(2005), 2011.
- P.H. Feenstra. Numerical Simulation of Stability Analysis of Crack Dilatancy Models. Tech, Rep.. *TNO Building and Constrction Research, Rijswijk The Netherlands*, 1989. ISSN BI-89-191.
- Anthony John Gannon. Solar Chimney Turbine Performance. 2002.
- Goto.Y. Cracks formed in concrete around deformed tension bars. 68(4):244–251, 1971.
- Reinhard Harte and Wilfried B. Krätzig. On structural characteristics of solar chimney power technology. *Proceedings of the 8th International Conference on Structural Dynamics*, (July):3561–3566, 2011.
- Reinhard Harte, Martin Graffmann, and Wilfried B. Krätzig. Optimization of Solar Updraft Chimneys by Nonlinear Response Analysis. *Applied Mechanics and Materials*, 283:25–34, 2013. ISSN 1662-7482. doi: 10.4028/www.scientific.net/AMM.283.25. URL <http://www.scientific.net/AMM.283.25>.
- John D. Holmes. *Wind load of structure*. Taylor Francis, second edition edition, 2007. ISBN 9780415409469.
- D.A. Hordijk. Local Approach of Ftigue of Concrete. *PHD thesis, Delft University of Technology*, 1991.
- ISO04353. *ISO 4354 2012: Wind actions on structures*, volume 4. 2012.

- Rots J.G. Computational modeling of concrete fracture. 1988.
- J Blaauwendraad J.G Rots. Crack models for concrete: discrete or smeared? Fixed, multi-directional or rotating? 34, 1989.
- L. Lohaus and Y. A. Abebe. Concrete Concepts for Solar Chimneys. *SCPT 2010 Proceedings*, 2010.
- F Lupi. Structural behaviour, optimization and design of a solar chimney prototype under wind loading and other actions. *Master Thesis, University of Florence in cooperation with Ruhr University Bochum*, 2009.
- F Lupi, C. Borri, R. Harte, W.B. Krätzig, and H.-J. Niemann. Facing technological challenges of Solar Updraft Power Plants. *Journal of Sound and Vibration*, 334:57–84, 2015. ISSN 0022460X. doi: 10.1016/j.jsv.2014.03.010. URL <http://www.sciencedirect.com/science/article/pii/S0022460X14001904>.
- Hans-j Niemann and R. Höffer. Wind Loading for the design of the Solar Tower. 24(2), 2009.
- Hans-jürgen Niemann, Francesca Lupi, R. Höffer, Wolfgang Hubert, and Claudio Borri. The Solar Updraft Power Plant: Design and Optimization of the Tower for Wind Effects. *Proceedings of the 5th European & African Conference on Wind Engineering*, (July):1–12, 2009.
- N. Haritos A. Hira B. Smali P. Mendis, T. Nogo and J. Cheung. Wind loading on Tall Buildings. pages 41–54, 2007.
- Kratzig Phillip L. Gould; Wilfried B. *Handbook of Structural Engineering*, volume 4. 2005.
- Robert H. Scanlan and Emil Simiu. *WIND EFFECTS ON STRUCTURES Fundamentals and Applications to design*. JOHN WILEY SONS,INC, third edition edition, 1996. ISBN 0471121576.
- Jorg Schlaich. Solar updraft tower.
- Aleksandr Sokolov. Tension stiffening model for reinforced concrete beams. 2010.
- FJ. Vecchio and ASCE M.P. Collins, Members. Compression Response of Cracked reinforced Concrete. *Journal of Structural Engineering*, 119, 1994.
- VGB-R-610E2010. *Structural Design of Cooling Towers: VGB Guideline on the Structural Design, Calculation, Engineering and Construction of Cooling Towers.*, volume 4. VGB PowerTech, 2010.



Background information

A.1. Solar Updraft Tower

Solar updraft tower is the new technology using the solar and wind energy without the supplying of cooling water (Schlaich). It is one of the solutions to the climate change crisis if the SUT is economically feasible. A conventional solar updraft power plant design is used in this thesis research. The economical feasibility of constructing the SUT are listed below,

- A rather clear and simple working principle with worldwide available constructing materials gives a possibility of realizing the SUT in the environmental brutal area. The required construction materials are mainly steel, concrete, glass, which is accessible for most of the countries.
- The solar updraft tower use only solar and wind renewable energy, and can operate for 24hrs with the help of absorber. The absorber stores the energy during the sunny days, and then releases the heat during the night and cloudy day.
- The power output and the efficiency are increased with the increase of the area of the air collector and the height of the tower.
- The SUT has a zero carbon footprint and is nearly pollution-free during operation.
- A service life of 100 years with low operation and maintenance needs is rather beneficial.

There are also some disadvantages for constructing SUT and realizing it in the market.

- Large cost for constructing the SUT with 1000m high is a big disadvantage. A high amount of water served as the heat absorber is needed at the starting stage.
- Realizing the solar updraft tower with height over 1000m is rather difficult due to external wind load, earthquake, and other structural challenges.
- The constructing of reinforced concrete solar updraft towers may give a negative effect on the local environment such as plant, animals species.

A.2. Wind-induced effects on SUT

Lupi (2009) performed the structural optimization of an SUT under the self-weight and the wind load with load factors of 1 and 1.5 respectively. The 1000 m SUT models with different stiffening ring layouts were built and analyzed. It was concluded that the upper cone gives a more shell-like deformation with ovaling of the cross section. The stiffness of the stiffening rings shows a decisive effect on

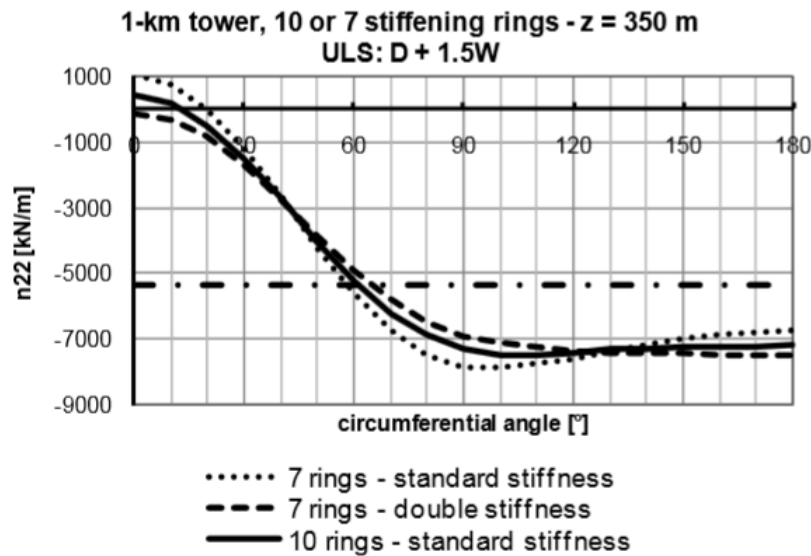


Figure A.1: Circumferential distributions of meridional resultant stresses at the ultimate limit state (D+1.5W) Comparison between 1-km tower with ten or seven rings (Lupi (2009))

whether the tower behaves more like a beam or more like a shell. It was found, when the number of stiffening rings reduced from 10 to 7, a larger ovaling deformation and a larger tension force acting on the throat height are observed.

Some models were built with the configuration of 10 stiffening rings, while the ring stiffness is gradually increased. The C50/60 concrete class is adopted. The stiffness rings give a cross-sectional area of $6.48m^2$ and inertia $J = 30.88m^4$. The tension at the windward side is reduced with doubled increased stiffness of the 10 stiffening rings. A more beam-like behavior is shown with a better distribution of the internal forces. It was also found that the increasing of the stiffness on the top cones gives greater benefits while the increasing of the stiffness rings along the hyperboloid is not necessary. Figure A.1 gives the circumferential distribution of the meridional stress resultant at the ultimate limit state (D+1.5W). As can be seen in the figure, the configuration of 7 stiffening rings with doubled stiffness shows a similar value of stress resultant distribution compared to the one with 10 stiffening rings with standard stiffness. The performed analysis is a linear static analysis without including nonlinearities and local bending moment caused by the eccentricity of the rings. The result does show the fundamental roles that the stiffness of the stiffening rings played for the structural behavior.

A.3. Concrete models

A.3.1. Concrete compressive curve

The Thorenfeldt curve is adopted in this research project. The factor n and k are determined by the default value. However, by modifying the n and k value, the curve got from the experimental data can also be modeled. DIANA provides several compressive curves, and the feasibility of the chosen model is discussed in Chapter 6. Some other models with their background theory will be explained in this section.

Parabolic

In DIANA, there are three other compressive models for smeared crack rotating model. One is a

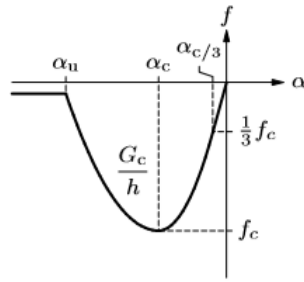


Figure A.2: Parabolic curve for concrete in compression (DIANA (2016))

parabolic curve. This curve is referred to a thesis research of Feenstra (1989). The post-peak behavior of concrete in compression is based on the fracture energy. The fracture energy for concrete in tension describes the energy for a single crack, which means the size of the element should have a similar dimension of a crack bandwidth. It works same for the fracture energy in compression which describes the fracture energy of a small element. The compressive curve and the formula are shown below. Fracture energy can be derived from experimental data and ultimately used as an input of Parabolic model. The curve is divided into four sections. The first linear section is from the starting point to the one-third of the maximum compressive strength(f_c).

$$\alpha_{c/3} = -\frac{1}{3} \frac{f_c}{E} \quad (\text{A.1})$$

The formula for the first linear section is shown below

$$f = -f_c \frac{1}{3} \frac{\alpha_j}{\alpha_{c/3}} \quad (\text{A.2})$$

The second section is the parabolic curved from $\frac{1}{3} f_c$ till the maximum compressive strength. This curve is not fracture energy-dependent.

$$\alpha_c = -\frac{5}{3} \frac{f_c}{E} = 5\alpha_{c/3} \quad (\text{A.3})$$

The formula for the second parabolic section is shown below.

$$f = -f_c \frac{1}{3} \left(1 + 4 \left(\frac{\alpha_j - \alpha_{c/3}}{\alpha_c - \alpha_{c/3}} \right) - 2 \left(\frac{\alpha_j - \alpha_{c/3}}{\alpha_c - \alpha_{c/3}} \right)^2 \right) \quad (\text{A.4})$$

The third section is the post-peak behavior of concrete in compression. Formula describes the curve from the maximum compressive strength until the ultimate strain. The concrete softening in compression stops when the ultimate strain is reached. This curve is calculated from the fracture energy.

$$\alpha_u = \alpha_c - \frac{3}{2} \frac{G_c}{h f_c} \quad (\text{A.5})$$

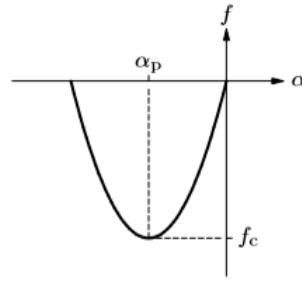


Figure A.3: Hognestad stress-strain relation for concrete in compression (DIANA (2016))

$$f = -f_c \left(1 - \left(\frac{\alpha_j - \alpha_c}{\alpha_u - \alpha_c}\right)^2\right) \quad (\text{A.6})$$

After the material reached the ultimate strain, the compressive strength of concrete becomes zero. The fracture energy of concrete in compression is normally about 50 to 100 times of the tensile fracture energy Feenstra (1989). Figure A.2 gives the parabolic compressive curve.

Hognestad Parabola

Hognestad Parabola (Figure A.3) has a relatively simple definition compared to other curves. It is determined by compressive strength. In DIANA, the influence of lateral confinement on concrete in compression is not included in Hognestad Parabola model. This curve is not related to fracture energy which means the element size has no effect on the compressive behavior of the structure. The formula shows below:

$$f = -f_c \left(2 \frac{\alpha}{\alpha_p} - \left(\frac{\alpha}{\alpha_p}\right)^2\right) \quad (\text{A.7})$$

The strain at maximum compressive strength gives,

$$\alpha_p = -\frac{2f_c}{E} \quad (\text{A.8})$$

Eurocode 2 EN 1992-1-1

In finite element modeling, if the input data is not according to the experimental result, it would be convenient to use the model from regulations. Once a concrete class is chosen, a concrete compressive model can be determined. DIANA offer the concrete compressive curve according to Eurocode 2 (EN 1992-1-1). This codified model does not take the lateral confinement into consideration. Figure A.4 is the given curve from Eurocode 2. It can be noticed that this model gives an ultimate strain with a relatively high compressive stress, and after material reached to ultimate strain, the stress will drop to zero suddenly.

$$f = -f_c \left(k \left(\frac{\alpha}{\alpha_c}\right)^2 / \left(1 + (k-2) \left(\frac{\alpha}{\alpha_c}\right)\right)\right) \quad (\text{A.9})$$

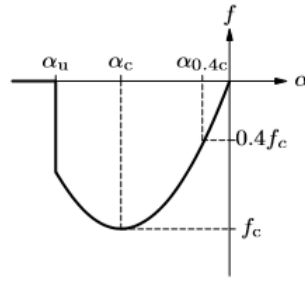


Figure A.4: Stress-strain relation according to EN 1992-1-1 for concrete in compression(DIANA (2016))

with

$$k = 1.05E_{cm}|\alpha_c|/f_c \quad (\text{A.10})$$

where E_{cm} is the Young's modulus approximated at $0.4f_c$:

$$E_{cm} = \frac{0.4f_c}{\alpha_{0.4c}} \quad (\text{A.11})$$

A.3.2. Cracking models

DIANA offers different types of concrete crack models; the total strain rotating crack model is adopted for this research project, the comparison of different cracking models has been done. The theory of other two types of crack models will be explained in this section.

Fixed smeared crack concept

Fixed smeared crack concept is a rather traditional cracking concept. Once the tensile strength of concrete is violated, the isotropic linear elastic law will switch to orthotropic law with a reduced stiffness. In the orthotropic law, a fixed principal n, s, t axis is applied. n is the direction perpendicular to crack which represents Mode I crack, and s and t are the directions tangential to the crack surface, which represents Mode II and Mode III crack.

In the fixed smeared crack model, the total strain is subdivided into a crack strain and a solid material strain. For global coordinate system

$$\Delta \varepsilon = \Delta \varepsilon^{cr} + \Delta \varepsilon^{co}$$

$$\Delta \varepsilon^{cr} = [\Delta \varepsilon_{xx}^{cr}, \Delta \varepsilon_{yy}^{cr}; \Delta \varepsilon_{zz}^{cr}, \Delta \gamma_{xy}^{cr}; \Delta \gamma_{yz}^{cr}; \Delta \gamma_{zx}^{cr}]$$

For n,s,t -coordinate system

$$\Delta e^{cr} = [\Delta \varepsilon_{nn}^{cr}; \Delta \gamma_{ns}^{cr}; \Delta \varepsilon_{nt}^{cr}]$$

Three component represent the three cracking modes.

The relation between local and global crack strain is connected by a transformation matrix who relates to the orientation of the crack. If N is a fixed matrix, the fixed cracked concept is applied. A traction increment at the crack is applied on a local coordinate system. The local traction increment and global stress increase are linked by the transformation matrix.

$$\Delta \varepsilon^{cr} = N \Delta e^{cr} \quad \Delta t^{cr} = N^T \Delta \sigma^{cr}$$

Both solid material and crack have its own constitutive model.

$$\begin{aligned}\Delta\sigma^{co} &= D^{co}\Delta\varepsilon^{co} \\ \Delta t^{cr} &= D^{cr}\Delta e^{cr}\end{aligned}$$

Multi-directional fixed smeared crack

Based on the concept of the single fixed smeared crack, a more advanced model can be introduced. The crack strain is further decomposed into multi-directional cracks.

$$\Delta\varepsilon^{cr} = \Delta\varepsilon_1^{cr} + \Delta\varepsilon_2^{cr} + \dots\dots\dots$$

Each crack contribute to the total crack strain at one sampling point. The local crack strain, the local traction increment and transformation materix shows below

$$\begin{aligned}\Delta e^{\hat{cr}} &= [\Delta e_1^{cr}; \Delta e_2^{cr} \dots\dots\dots] \\ \Delta t^{\hat{cr}} &= [\Delta t_1^{cr}; \Delta t_2^{cr} \dots\dots\dots] \\ \hat{N} &= [\Delta N_1; \Delta N_2 \dots\dots\dots]\end{aligned}$$

Follow the same theory of the single fixed crack, we have

$$\begin{aligned}\Delta\varepsilon^{cr} &= \hat{N}\Delta e^{\hat{cr}} \\ \Delta t^{cr} &= \hat{D}^{cr}\Delta e^{\hat{cr}}\end{aligned}$$

For concrete under biaxial or triaxial tension, the crack tends to crack orthogonal to each other. In this loading condition, the multi-directional fixed crack model is a good approach to simulate. For concrete under tension and shear, the principal axis tends to rotate after the crack formation. Once the angle between the principal axis and crack exceed a threshold value, a new crack will initiate.

A.3.3. Concrete tensile behavior

In total strain crack model, DIANA provides wide varieties of tensile models. Figure A.5 lists all available tensile models. These can be divided into two types. One is tension softening, and the other is tension stiffening. As discussed in this research, tension softening is not a feasible model for a large reinforcement concrete structure with element size around 5m. DIANA provides the different shape of the curve from simple to complex which gives the modeling flexibility. The most commonly used curve is linear fracture energy based model and exponential model. For cyclic loading or concrete in fatigue, the model of Hordijk offers good functionality and flexibility, more detailed please refer to Hordijk (1991). JSCE model gives tension softening without considering tensile fracture energy. CEB-FIP model code gives a material model that concrete starts microcracking before the tensile strength is reached. The CEB-FIP 1990 model is a concrete aggregate size dependent curve. For tension softening, DIANA also offers a fiber-reinforced concrete model. Multilinear is fully described stress-strain behavior, the definition of tensile strength is not needed.

In this thesis research, the concrete tensile behavior includes the tension stiffening effect. The Figure A.6 gives the tension stiffening model and calculated linear ultimate strain model that used in the FEM.

A.4. Finite element software

In this section, a comparison with a variety of software tools for nonlinear finite element modeling of reinforced concrete is done. The most commonly used programs are ABAQUS, ADINA, ATENA, DIANA. Table A.1 gives the comparison of different programs on simulating concrete material, and table A.2 gives the one for reinforcement.

ABAQUS

ABAQUS is general finite element software used in the variety of applications. To tackle all these different applications, ABAQUS has different analysis package.

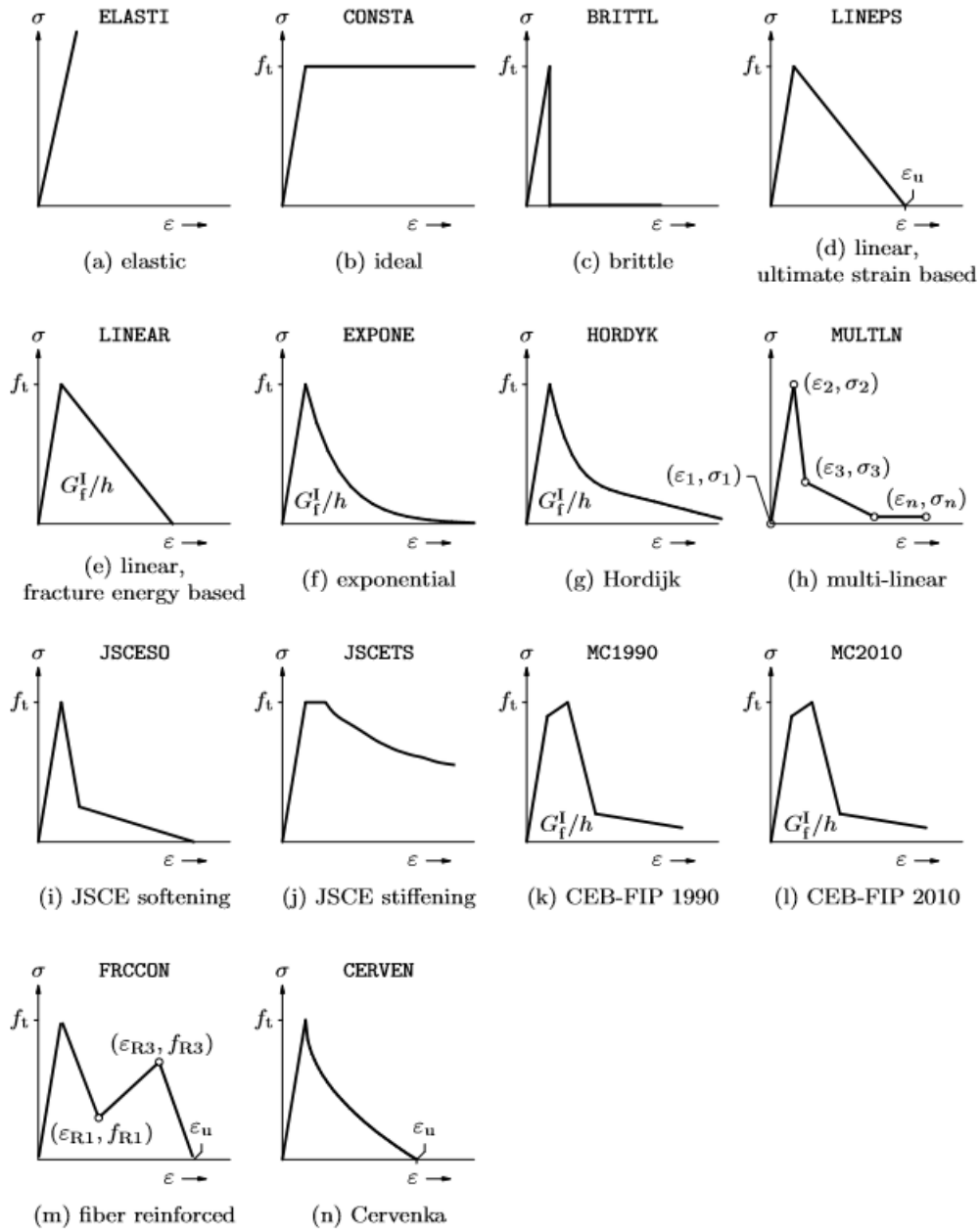


Figure A.5: Stress-strain relation of different concrete cracking model (DIANA (2016))

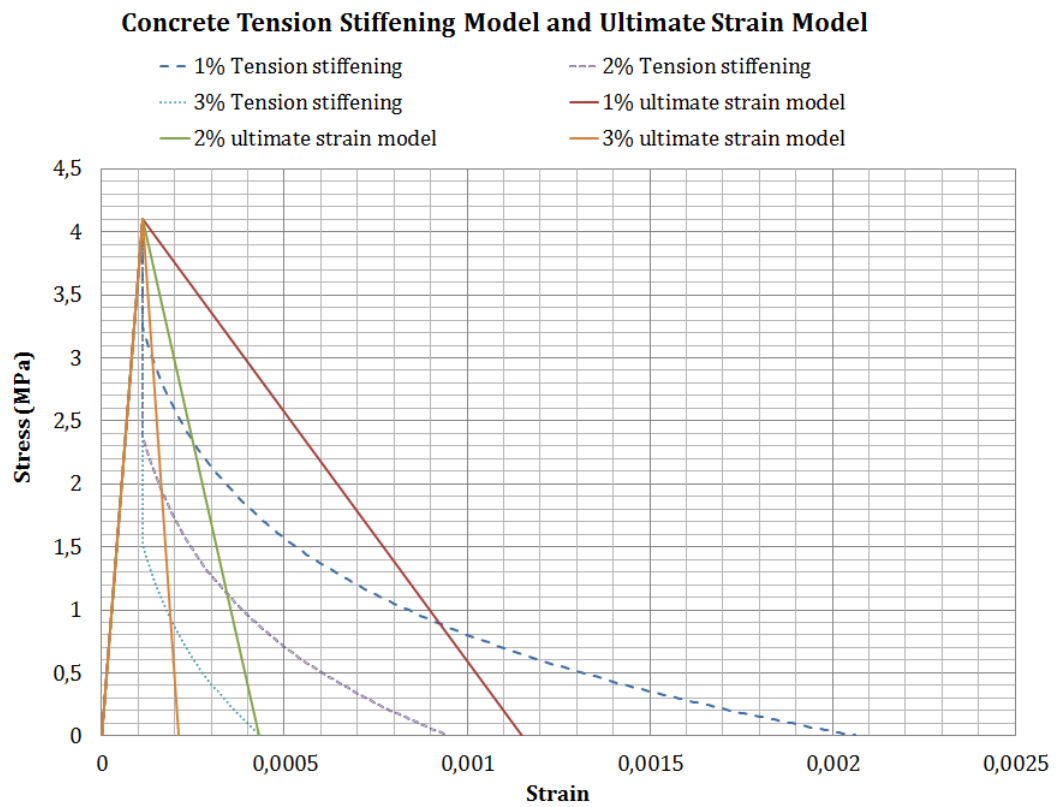


Figure A.6: The tension stiffening model and the linear ultimate strain model used in the FEM

Table A.1: Comparison of different finite element modeling software on modeling concrete

Concrete simulation					
		ABAQUS	ADINA	ATENA	DIANA
Structural elements	Beam	△	△	△	△
	Plate/shell	△	△	△	△
Continuum elements	2D solid	△	△	△	△
	3D solid	△	△	△	△
Constitutive	Compression Softening		△	△	△
	Tension Stiffening	△	△	△	△
	Plastic Offset	△			△
Cracking model	Smearred	△	△	△	△
	Discrete	△			△
Shear Strength Check		△	△	△	△
Crack Width Check					△

Table A.2: Comparison of different finite element software on modeling reinforcement

Reinforcement simulation					
		ABAQUS	ADINA	ATENA	DIANA
Elements	Discrete	△	△	△	△
	Smearred	△		△	△
Constitutive Relations	Strain Hardening	△	△	△	△
	Plastic Offset	△	△	△	△
Bond	Specific Element	△		△	△
	Bond slip relation	△		△	△

ADINA

ADINA superior on automatic dynamic incremental nonlinear analysis and it can also proceed nonlinear analysis of solids and structures.

ATENA

ATENA is specialized in the modeling reinforced concrete. It is capable of doing load carrying capacity analysis, push-over analysis, crack width calculations and areas of concretes crushing.

DIANA

DIANA is the software developed by The Department of Computational Mechanics at the TNO Building and Construction Research. It provides finite element analysis for reinforced concrete for different applications. The analysis such as structural eigenvalue, modal response structural response spectrum, structural nonlinearity and so on are included.

A.5. Wind load on the SUT

Niemann and Höffer (Niemann and Höffer (2009)) proposed a method of wind loading calculation for the solar updraft towers. The wind load coefficient distribution according to Niemann and Höffer over the circumference is changing vertically, which causes difficulty on modeling in FEM. The external wind pressure coefficient over the circumference for these two models is shown in FigureA.7. In order to compare the research of Eck et al. (2015) with current research, the one according to VGB Guideline will be used.

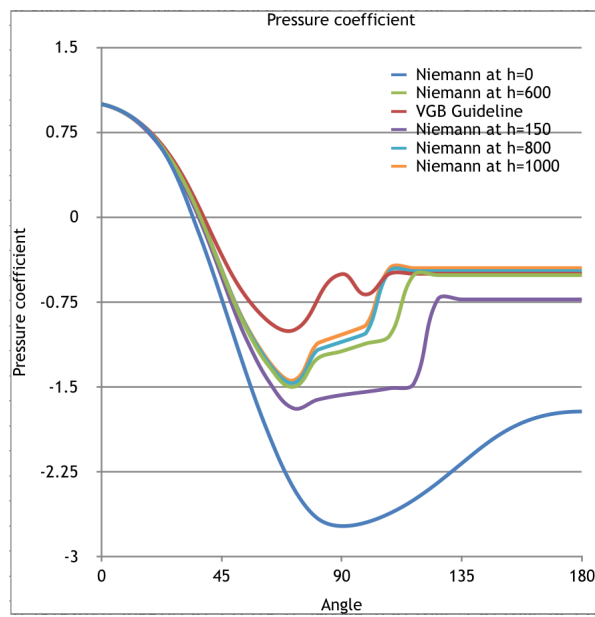


Figure A.7: Pressure coefficient over circumference of solar updraft tower

B

Reinforcement layout analysis

According to VGB guideline(VGB-R-610E2010 (2010)), a minimum reinforcement ratio is required for the shell wall. The ratios are 0.3% in the meridional direction and in the lower half is 0.3% and in the upper half 0.4% in the circumferential direction. Two reinforcement layouts are considered. One is modeling a one layer of reinforcement grid located at the center of the shell in both directions. The other is modeling two layers reinforcement grid in both directions with a calculated concrete cover of 40mm at both sides of the shell wall. Both two layouts have same reinforcement ratio of 0.4%, while their bending moment capacity might be different. Compared to the one layer reinforcement grid, two layers reinforcement grid needs twice of the elements and calculation time of the one layer reinforcement grid needed. A one layer reinforcement model would be a preference if these two layouts have no significant difference in structural behavior.

B.1. Finite element modeling

B.1.1. Geometry

Two rectangular slabs are modeled with dimensions of 10mx5m and a thickness of 0.25m Reinforcement will be modeled at the mid-surface of the slab for the one layer layout, and two layers reinforcement will be modeled at a distance of 40mm to the upper and lower surfaces of the shell.

B.1.2. Material model

TableB.1 and TableB.2 give the nonlinear material properties of these two models.

B.1.3. Concrete cover

The nominal concrete cover is subdivided into a minimum cover and a deviation. For in-situ concrete, the deviation would be 10mm. Calculation of minimum concrete cover should satisfy both for the structural class and the exposure class according to EN1992-1-1 (2011). To prevent the splitting of concrete cover, the concrete over has to be thicker than the reinforcing bar diameter. With an external concrete that is constructed in a dry area, the exposure class would be XC3. For design working life of 100-year with strength class of C50/60, the minimum concrete cover is 30mm. The nominal concrete cover for the solar updraft tower would be 40mm.

B.1.4. Element type, meshing and boundary conditions

The curved shell elements CQ40S is chosen for modeling the concrete slab, and the reinforcement grid elements is chosen for modeling the reinforcement layout. The meshing size is 0.5mx0.5m in a square shape. The two edges with a length of 5m will be constrained in translation x-,y-,z-direction and are

Table B.1: Concrete material properties

Linear properties	Material type	Concrete
	Smearred crack model	Total strain based crack model
	Young's modulus	$37000N/mm^2$
	Poisson's ratio	0.2
Crack model	Mass density	$2500N/m^3/g$
	Crack rotation	Rotation
Tensile behavior	Crack bandwidth	
	Tensile model	Linear-ultimate crack strain
	Tensile strength	$4.1N/mm^2$
	Ultimate strain	0.001
	Residual tensile strength	$0N/m^2$
	Reduction by lateral cracking	No reduction
Compressive behavior	Poisson's ratio reduction	No reduction
	Compressive curve	Ideal
	Compressive strength	$58N/mm^2$

Table B.2: Material properties of reinforcement

f_{yk}	500MPa
E_p	200GPa
ν_c	0.3
f_{uk}	540MPa
ε_u	0.05

free to rotate. FigureB.1 shows the finite element modeling with its meshing density and boundary conditions. Only self-weight is considered in this nonlinear analysis.

B.1.5. Results and conclusions

The results give an inside comparison of the influence of different reinforcement layout on structural behavior. The one layer reinforcement model experiences a failure at a load factor of 1.32 with excessive crack width. The two layers reinforcement model fails at a load factor of 1.39. A 5% of the difference is observed on load bearing capacity. At the load level of 1.32D, the model for one layer reinforcement has a maximum deflection of 0.048m, while for the one with two layers reinforcement is 0.044m. An 8% of differences is observed. FigureB.2 gives the crack strain at bottom fiber in the middle strip of the slab. Due to the effective depth of 125mm for one layer layout, the beam needs the crack to propagate to the middle fiber in order to activate the reinforcement. A large crack strain at bottom fiber is observed. Once the crack is initiated, all reinforcement located at the middle surface is activated and starts bearing the tensile force. For two layers reinforcement layout, the reinforcement is activated with a smaller crack opening and then the reinforcement starts bearing the tensile force. The level arm for two layers layouts is 206mm. However, an only half amount of reinforcement is under tension which gives a lower the bending moment capacity compared to the bending moment capacity due to a small level arm in the one layer reinforcement layout. These two layouts have a maximum difference around 12%. For the current research, one layer reinforcement layout is chosen for the sake of simplification and reducing the number of elements and the calculation time.

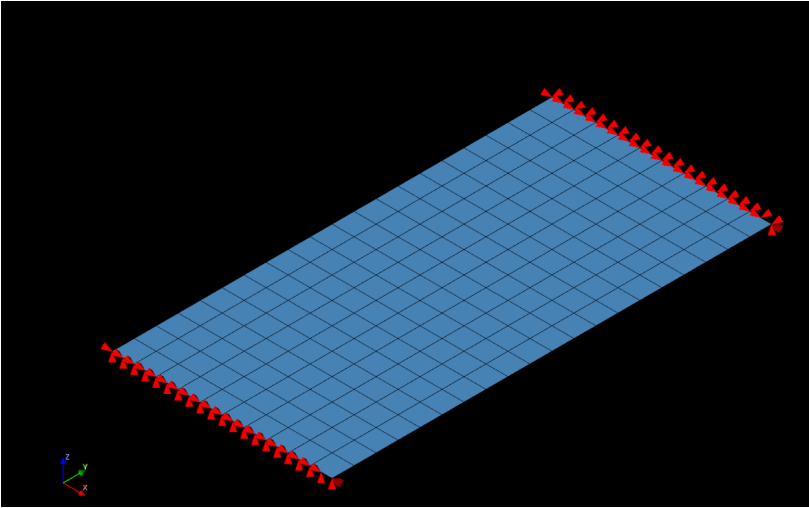


Figure B.1: 5x10m slab model with meshing and boundary conditions details

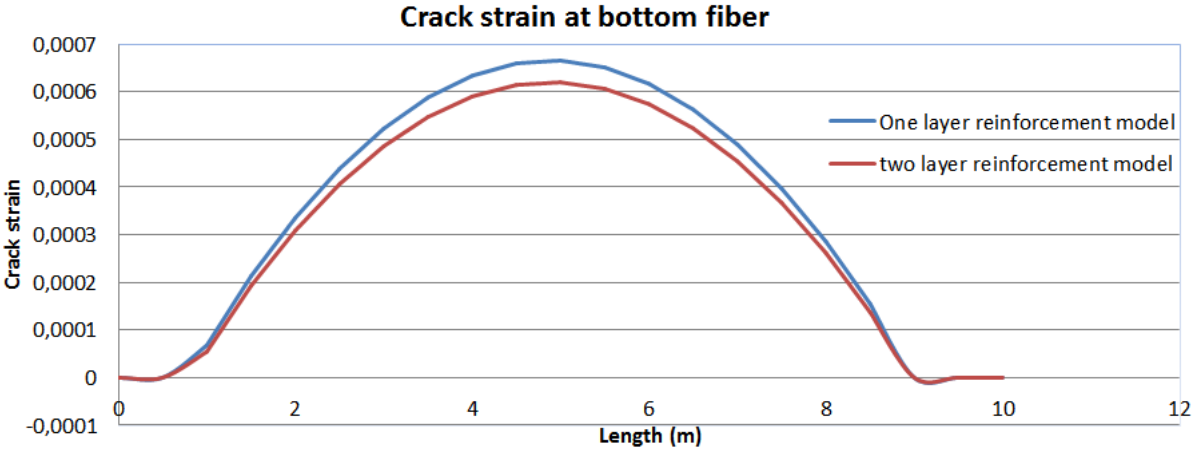
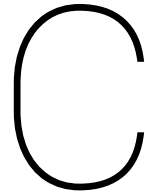


Figure B.2: Crack strain for one layer reinforcement and two layer reinforcement layout



Stiffening ring analysis

C.1. Structural elements for modeling the stiffening rings

Among all different types of shell element, for modeling circular stiffening ring, only curved shell element is the available element type. For beam element, DIANA offers three classes of the beam elements. Given the objectives of this research is to conduct a physical nonlinear analysis, only Class III beam element is applicable. The following explanation gives the theory assumption used in both elements.

These two element types both base on Reissner-Mindlin kinematical assumptions. The assumption is applied to the line normal to the un-deformed mid surface for curved shell and the cross section normal to the undeformed beam axis for beam element. Reissner-Mindline assumption applied to shell element and beam element in 3D and 2D respectively.

- *For curved shell elements*, the material line that orthogonal to the mid-surface of the in-deformed shell remains straight after deformation, but it does not have to be perpendicular to the surface at the undeformed stage. The normal stress perpendicular to the mid-surface is assumed to be zero.
- *For Class III 3D beam elements*, the mean cross-section remains planer but not necessarily perpendicular to the deformed beam axis.

C.1.1. Variable

Though both element types apply the same Reissner-Mindlin kinematical assumption, the available variables are different. Table C.1 gives the comparison of availability of 3D stresses and strains for both element types. A number of variables of beam element is half of that of shell element. The stress

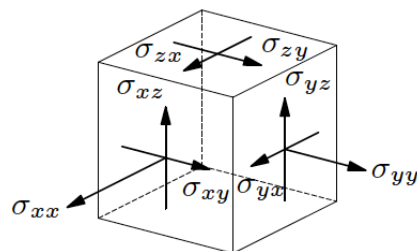


Figure C.1: Cauchy stress on a unit cube in their positive direction (DIANA (2016))

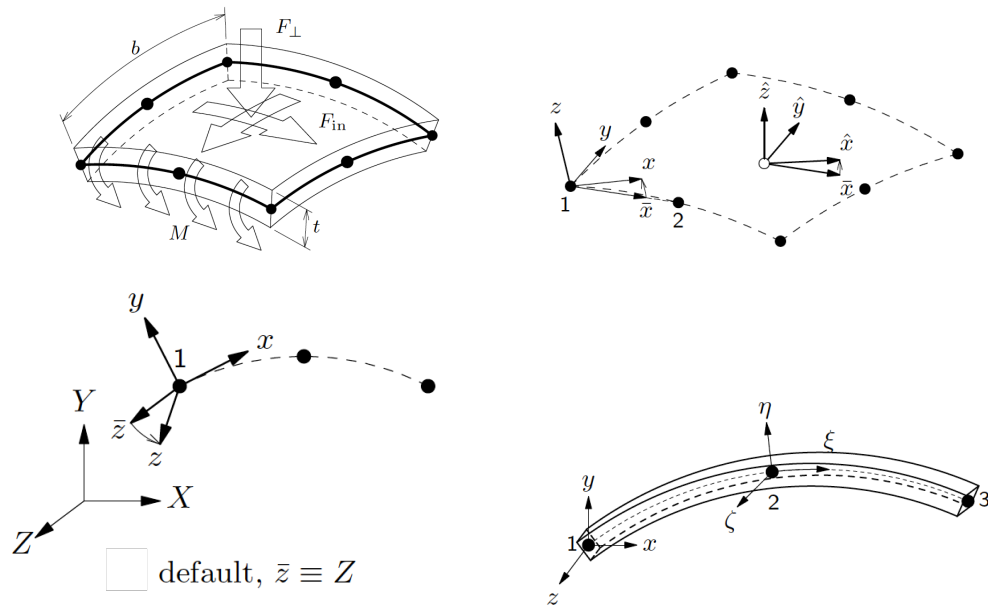


Figure C.2: CQ40S-QUADRILATERAL, 8 nodes and Axis for three dimensional beam (DIANA (2016))

and strain related to the y -direction are not taken into account in beam element, which means the stiffness in the transverse direction of the stiffening ring is not considered, so as to the transverse reinforcement added in the stiffening ring. Figure C.1 shows the notation of stress location and their positive direction on a cubic block. Figure C.2 shows the CQ40S shell element and CL18B beam element. For result output, stress and strain distribution are required. Due to the differences between element types, it is necessary to understand the distribution role for different stress:

- *In curved shell element*, $\varepsilon_{xx}; \varepsilon_{yy}; \gamma_{XY}$ vary linearly in thickness direction. The transverse shear strains $\gamma_{YZ}; \gamma_{ZX}$ are kept constant over the thickness. While the actual transverse shear strains vary parabolically over the thickness, a shear reduction factor with the magnitude of 1.2 is applied to get the correct shear strain energy. Figure C.2 shows the eight nodes quadrilateral curved shell element and its nodal axis and element axis.
- *In Class III 3D beam element*, the normal strain ε_{xx} varies linearly over cross-section area, and shear strain is forced to be constant over the cross-section. In reality, the shear stress and strain vary quadratically over the cross section, a shear reduction factor with a magnitude of 1.2 is applied to get the right shear strain energy. Figure C.2 also shows the 3 point Class III 3D curved beam element and its nodal and element axis.

C.2. Sub-research on the stiffening rings analysis

The purpose of the study is not ensure the Beam Nonlinear Model and Shell Nonlinear Model has a accurate modeling on stiffening rings. Modelling stiffening ring in a simple loading condition, if BRM and SRM gives a similar result, it can be conclude the modeling of ring is accurate and can be used in a rather complex modeling. Due to the beam element does not consider the transverse stiffness, only the longitudinal reinforcement modeled. This modeling setup is also identical to the Beam Nonlinear Model in the main thesis research.

Table C.1: Variable for curved shell element and Class III 3D beam element

		Curved shell element	Class III 3D beam element
	Degree of freedom	$u_X, u_Y, u_z, \phi_x, \phi_y$	$u_X, u_Y, u_z, \phi_X, \phi_Y, \phi_Z$
Strain	ϵ_{xx}	Δ	Δ
	ϵ_{yy}	Δ	
	ϵ_{zz}	Δ	
	γ_{xy}	Δ	Δ
	γ_{yz}	Δ	
	γ_{zx}	Δ	Δ
Stress	σ_{xx}	Δ	Δ
	σ_{yy}	Δ	
	σ_{zz}	$= 0$	
	σ_{xy}	Δ	Δ
	σ_{yz}	Δ	
	σ_{zx}	Δ	Δ

C.2.1. Introduction

In this section, two simple were built. A simply supported beam with a cross-section built according to the intermediate stiffening rings and 25m long. The beam is simply supported at the two ends and under a distributed load.

- **Beam Ring Model (BRM)** the beam is modeled by Class III 3D beam element.
- **Shell Ring Model (SRM)** the beam is modeled by Curved shell element.

A nonlinear analysis was done and with increasing distributed load. A detailed calculation on how to modeling the stiffening rings and meshing the element on the beam element will be described in the next section. TableB.1 and TableB.2 gvies the nonlinear material properties. Their ultimate strain for concrete tensile model is 0.001.

C.2.2. Mesh

For SRM, the beam are divided into 20 equal segment in longitudinal direction. The horizontal section of the beam is divided into 8 parts and the vertical section of the beam is divided into 4 parts. Figure C.3 shows the geometries of two models together with meshing are shown.

C.2.3. Reinforcement setup

In the first assumption, the reinforcement ratio of stiffening ring would be 1%. The expression for reinforcement ratio is the following:

$$\rho = \frac{A_s}{bd} \quad (C.1)$$

Where

ρ is the reinforcement ratio

A_s is the total cross-sectional area of reinforcement

b is the width of RC beam

d is the effective depth of RC beam

There is a horizontal and a vertical section of stiffening ring. Two sections have different effective depth, which means they have different cross-sectional area for the reinforcement per meter width. Assume a horizontal beam with height of 800mm and 1m width. The reinforcement will located in

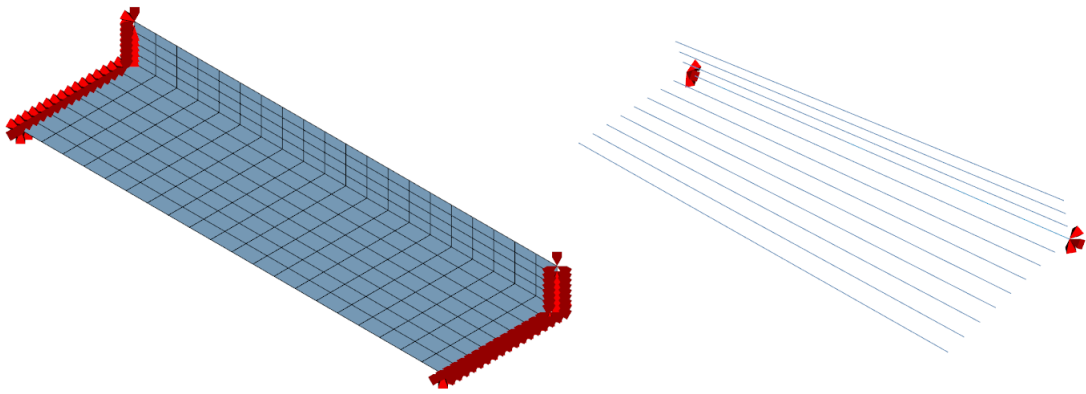


Figure C.3: Drawing of top and intermediate stiffening ring by Krätzig & Partner, Germany (Lupi et al., 2015)(Niemann et al., 2009)

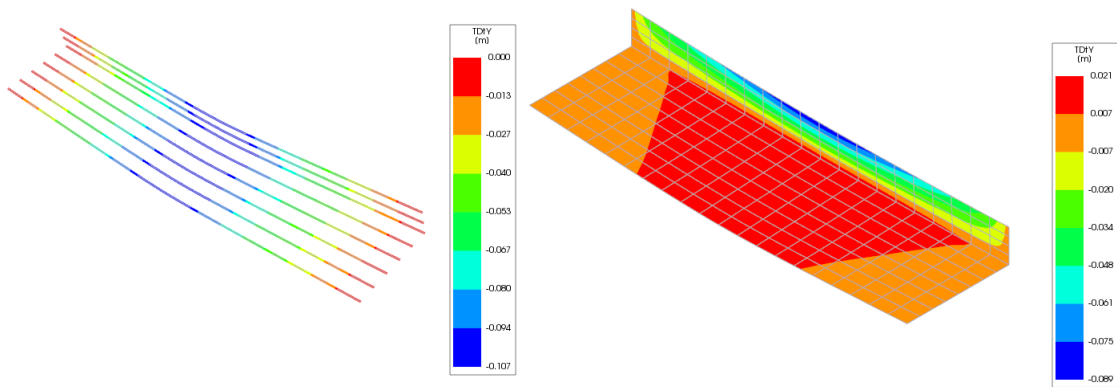


Figure C.4: Displacement distribution in vertical direction for Beam Ring Model(left) and Shell Ring Model(right) at load step 71

position with concrete cover of 40mm. The effective depth would be 760mm. Assume the vertical beam with 500m height and 1m width. The concrete beam has a cover of 40mm. The effective depth of vertical beam would be 460. Their cross-sectional area of horizontal section and vertical section reinforcement per meter width would be $7600\text{mm}^2/\text{m}$ and $4600\text{mm}^2/\text{m}$ in each direction. As input thickness, the vertical reinforcement layer thickness is 0.0076m and the horizontal reinforcement layer thickness is 0.0046m for reinforcement ratio equal to 1%. For reinforcement ratio equal to 2%, the thickness will be doubled.

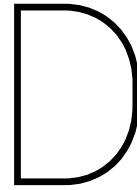
In the 3D Mindlin beam model, for simplification, 8 reinforcement bars will be modeled in longitudinal direction and no transverse reinforcement will be modeled. The reinforcement bar will be evenly distributed over the width of beam. For reinforcement in horizontal section and vertical section, the cross-sectional area of each reinforcement bar is 6650mm^2 and 2933mm^2 in longitudinal direction respectively.

C.3. Results and conclusions

For Beam Ring Model, the model diverged at load steps 75, while for Shell ring model is load step 77. A rather similar load bearing capacity is found for two model with differences of 2.6% of differences.

Figure C.4 gives the displacement comparison at the load step 71. The maximum displacement of SRM is 0.089, while for BRM is 0.107. Their differences is 16%. This can be explained in the following: the beam element does not take the transverse stiffness taken into account. It only consider the stress in bar direction. In the 3D Class III beam element, the cross-section of the beam remain planar after the deformation, which gives a certain constraint on the response on the transverse direction. However, a sufficient reinforcement is added in transverse direction in SRM. With addition stiffness in transverse direction of SRM, the beam shows a stiffer behavior than BRM.

The deformed shape as well as the magnitude for BRM is identical in transverse direction and their displacement distribution and magnitude is similar. each reinforcing bar followed the same deformed shape. But for SRM, the displacement gives a complex distribution. A upwards displacement at the middle of the horizontal section of the ring and a downwards displacement at the middle of the vertical section of the ring are observed. Even their loading capacity are similar, their deformed shape and displacement distribution still have a certain differences. The curve shell elements gives a much more realistic behavior on the structure behavior.



Nonlinear Result

This chapter displays most of the results in nonlinear analysis models.

D.1. Displacement

The displacements in x direction for all nonlinear models were shown in chapter 7 and 8. The displacement in the y direction gives a direct visualization on the extend of ovaling deformation of the upper cone. Figure D.1 shows the displacement in y direction for models 1%NM, 2%NM, 3%NM, 2%RNM and 1%RNM. The displacement in y direction decreases with the increase of the reinforcement ratio. The maximum value is found in 1%NM with magnitude of 7.15m and 2%RNM shows a minimum displacement with magnitude of 0.432m.

D.2. First principal strain distribution

The total strain rotational crack model gives that the crack is always rotating with the first principal strain. It is of interest to show the first principal strain distribution over the whole tower. The large strain shows not only the structural critical area but also the crack distribution. The maximum strain will be shown in two parts. One is the strain distribution from 0-0.0009018, which is the strain distribution of the tower that within the maximum allowable crack strain. The second part is the crack distribution that exceeds the maximum allowable value. Figure D.2 and D.3 show these two distributions of the first principal strain models 1%NM, 2%NM, 3%NM, 2%RNM, 1%RNM respectively.

D.3. Stress-resultant in the meridional direction

The meridional stress distribution can be affected by the stiffness of the stiffening rings significantly. A weak stiffness of upper cone leads to an ovalization deformation which causes a large tensile force acting on the throat height in the meridional direction. Figure D.4 and Figure D.5 give the meridional stress resultant distribution in the windward direction for individual models. The left-hand side of Figure D.7 shows the changing of the stress resultant with increasing reinforcement ratio. The right-hand side of Figure D.7 gives the recentered models with increasing reinforcement ratios, and they are compared with Detailed Linear Model. In the original design model, the force distribution moves to the compression sides with the increasing of the reinforcement ratio. Large stress fluctuations are observed in both models near the stiffening rings. No large stress fluctuations are found in the Recentered Models.

Figure D.8 and Figure D.9 show the meridional stress resultant distribution over the circumference at the throat height of the tower. The weak structure gives a larger tensile peak and larger compressive peak. The stress distribution is not uniform. The force distribution in 2%RNM is more linearly

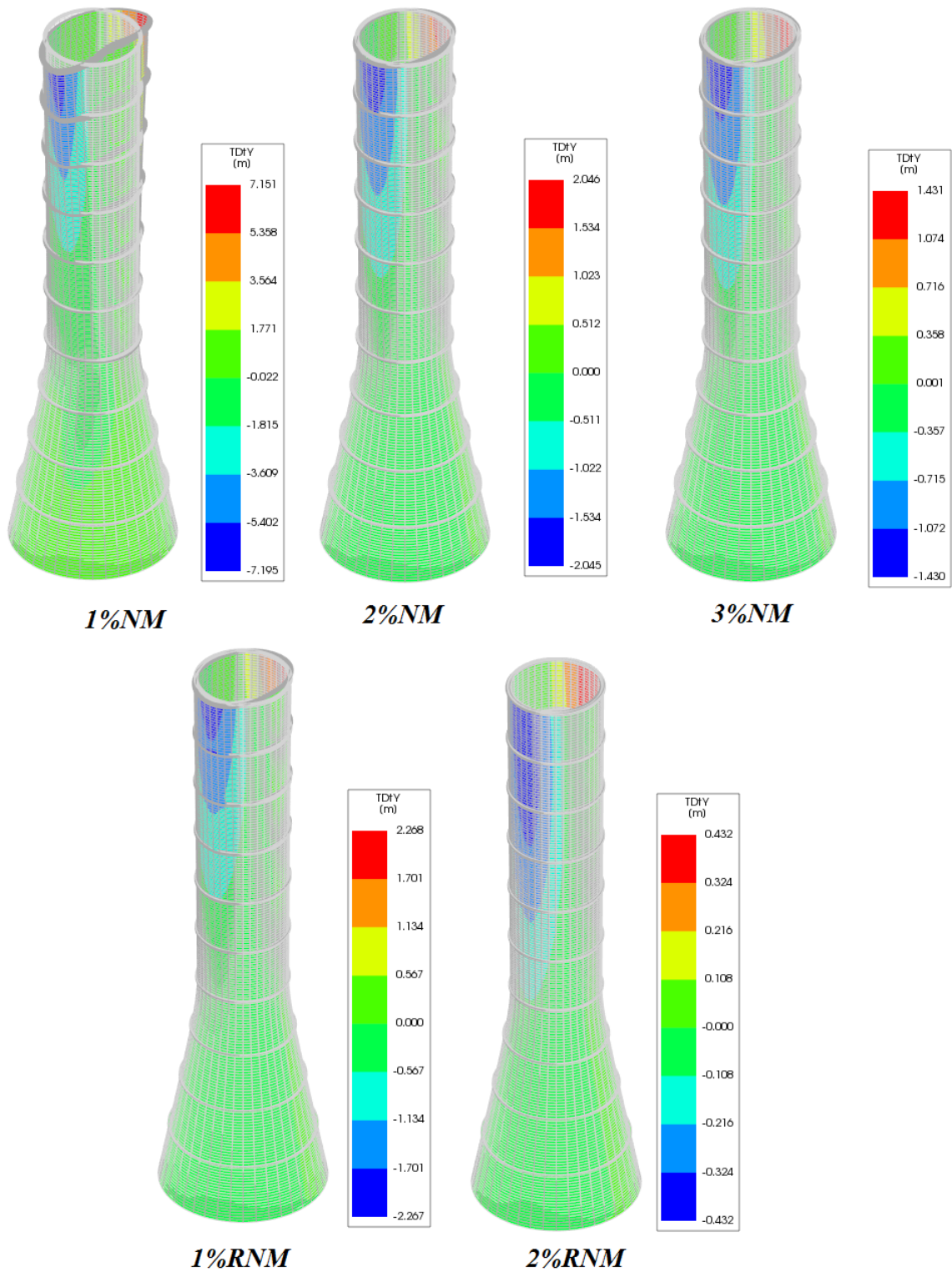


Figure D.1: Displacement in y direction for models 1%NM, 2%NM, 3%NM, 2%RNM, 1%RNM

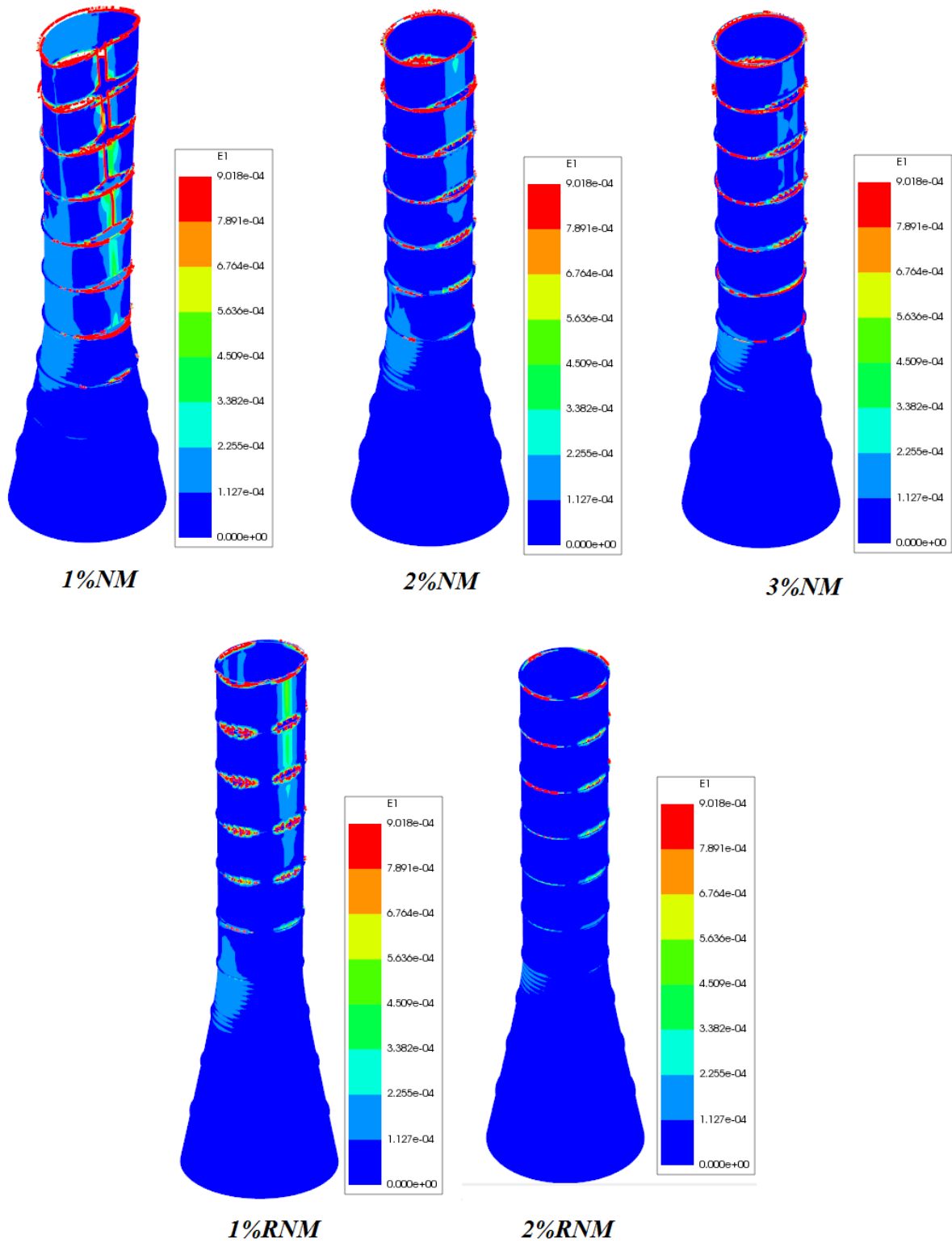


Figure D.2: The maximum principal strain distribution(0-0.0009018) for models 1%NM, 2%NM, 3%NM, 2%RNM,1%RNM

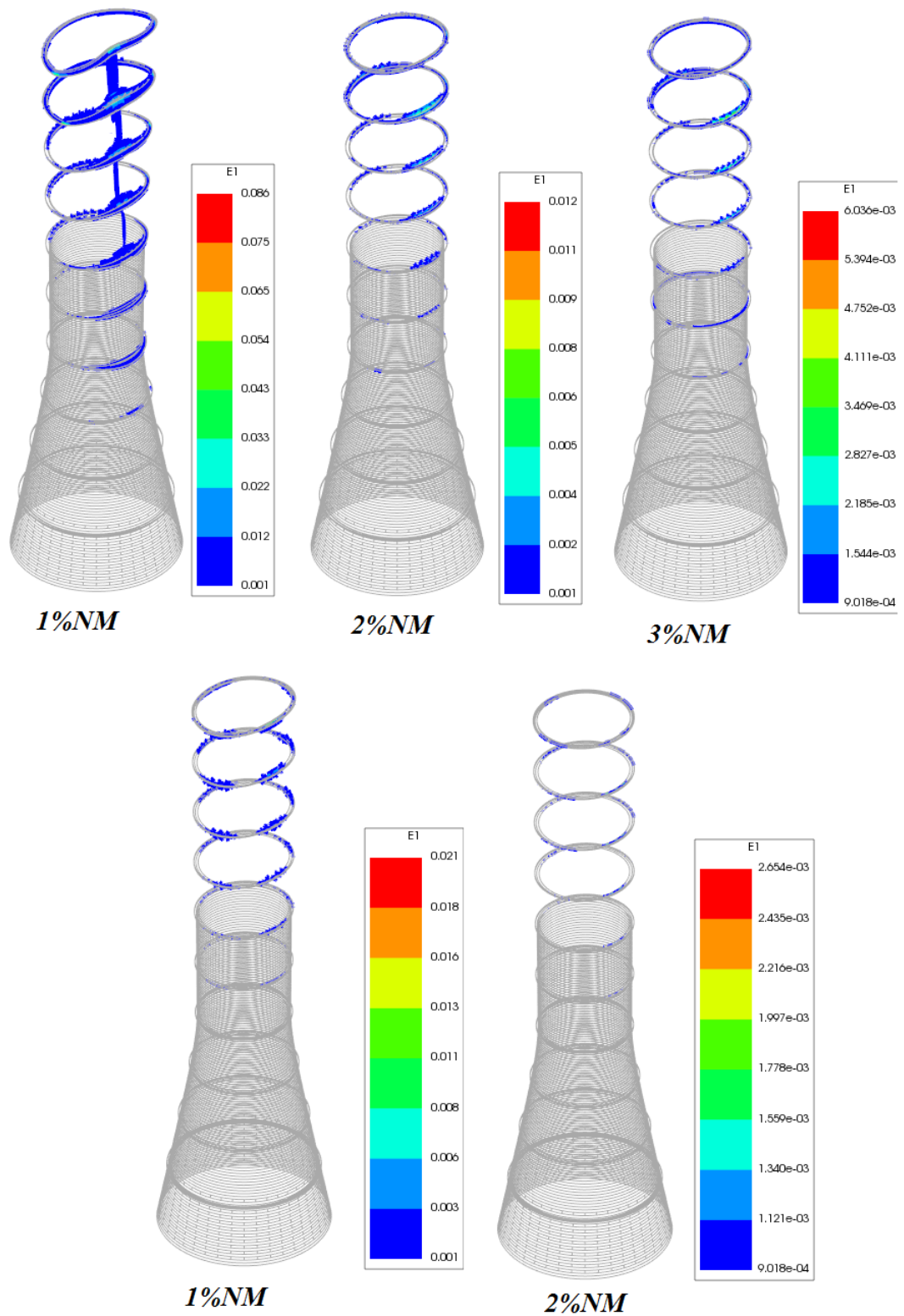


Figure D.3: The maximum principal strain distribution(0.0009018-max) for models 1%NM, 2%NM, 3%NM, 2%RNM,1%RNM

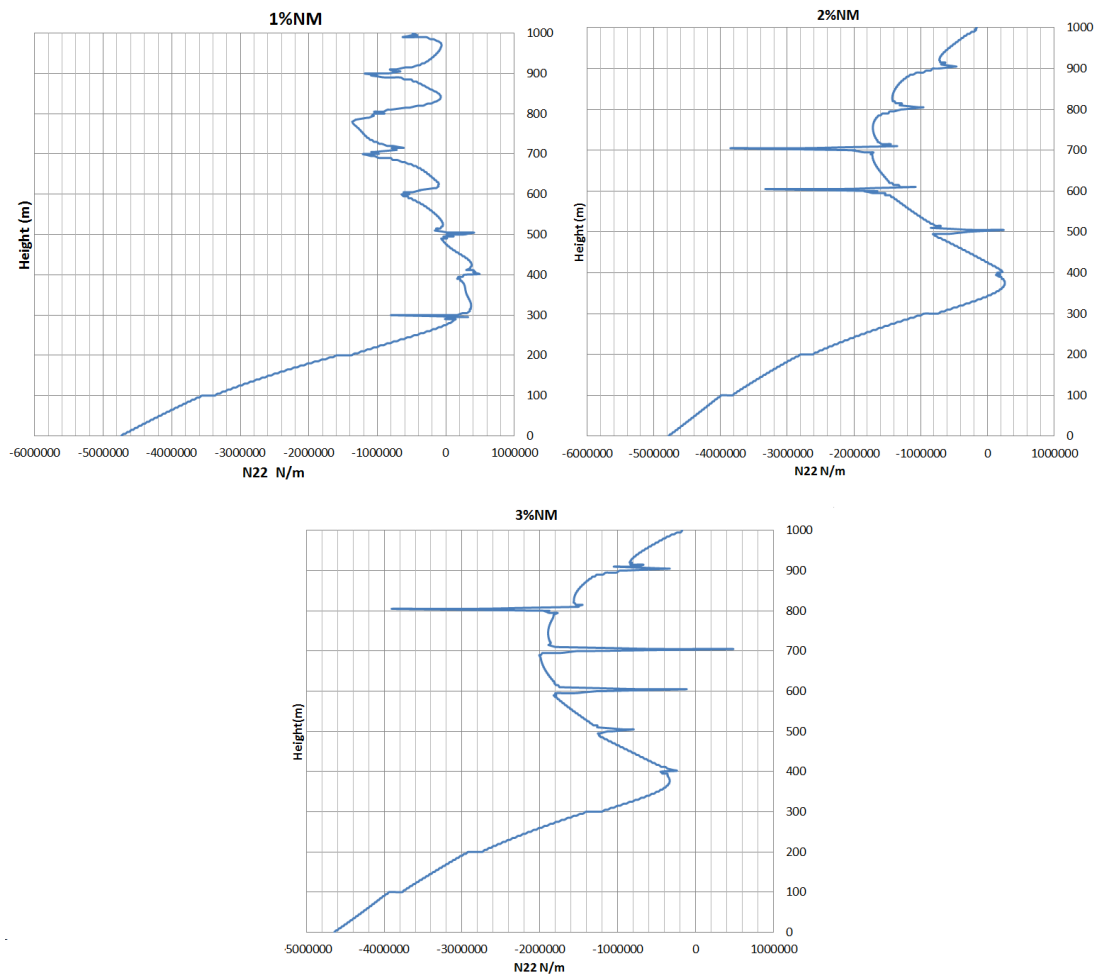


Figure D.4: The meridional stress distribution at the windward direction for 1%NM, 2%NM, 3%NM

distributed. 2%RNM and 3%NM gives distributions without tensile forces. But 2%RNM gives a more linear distribution compared to the 3%RNM. In addition, 2%RNM shows an even better stress distribution compared to DLM, which gives a fewer stress fluctuations.

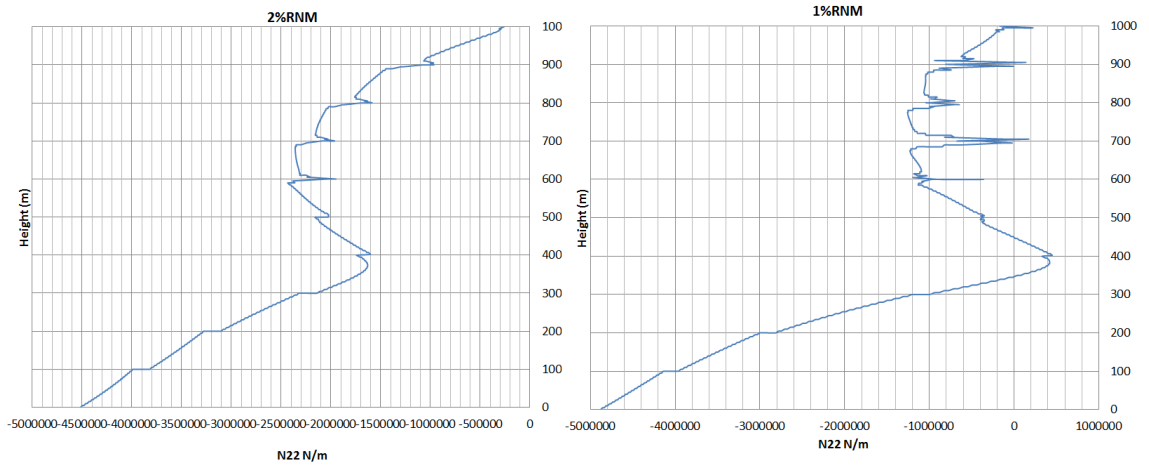


Figure D.5: The meridional stress distribution at the winward direction for 2%RNM,1%RNM

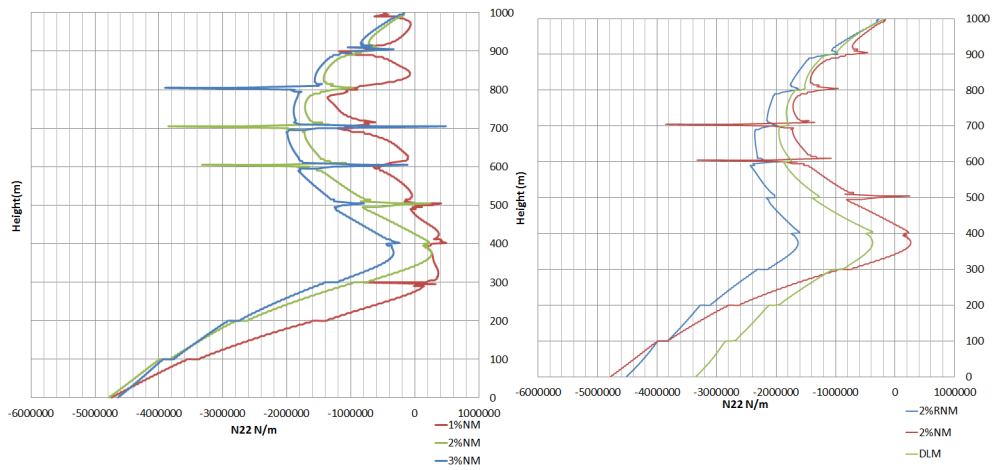


Figure D.6: The comparison of meridional stress distribution at the windward direction for 1%NM, 2%NM, 3%NM(left);the comparison of meridional stress distribution at the windward direction for 2%RNM, 2%NM, DLM(left)

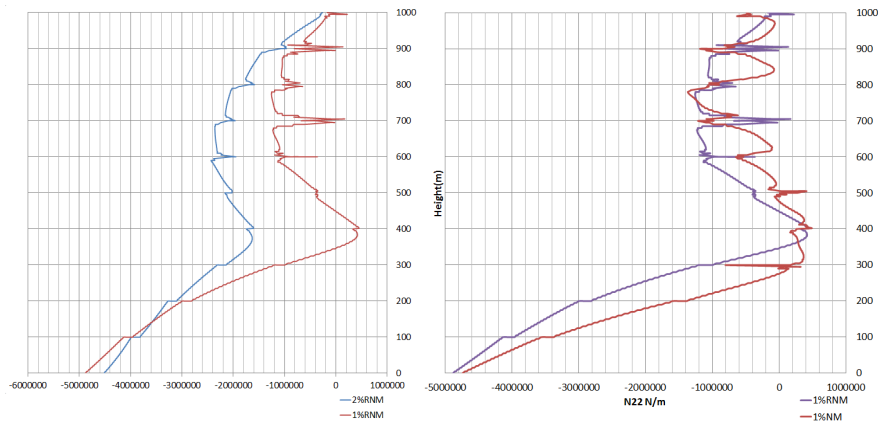


Figure D.7: The comparison of meridional stress distribution at the windward direction for 2%RNM, 1%RNM(left);the comparison of meridional stress distribution at the windward direction for 1%RNM, 1%NM,(right)

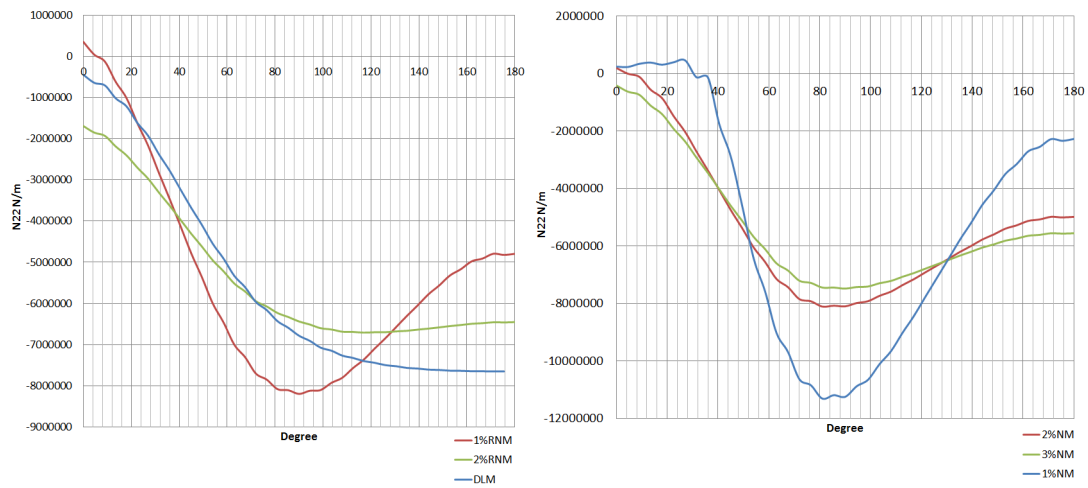


Figure D.8: The comparison of meridional stress distribution at the windward direction at the throat height over the circumference for 1%RNM, 2%RNM, DLM; the comparison of meridional stress distribution at the windward direction at the throat height over the circumference for 2%NM, 3%NM, 1%NM

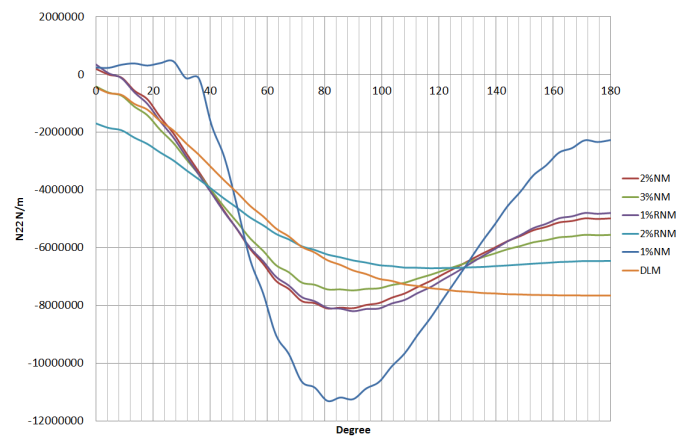
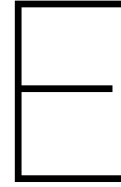


Figure D.9: The comparison of meridional stress distribution at the windward direction at the throat height over the circumference for 2%NM, 3%NM, 1%NM, 1%RNM, 2%RNM, DLM



2% Recentered Nonlinear Model

In this chapter, 2%RNM will be further analysis with a higher horizontal wind load. Since a linear behavior is found when solar updraft tower under static wind action in the serviceability limit state, this analysis is done by increasing the wind load until the load factor 2. The structural behavior is shown in this chapter by providing the displacement, the principal stress distribution, the reinforcement yielding distribution and the stress resultant distribution.

E.1. Load steps-displacement curve

The load steps-displacement curve of 2%RNM with D+2W loading conditions is compared with other nonlinear material models (Figure E.1). As can be seen, 2%RNM kept its initial slope until the last load step (1D+2W). No discontinuities are found in the load steps-displacement curve. A maximum displacement (2.66m) at D+2W of 2%RNM is similar to the maximum displacement of 3%NM at D+W.

E.2. Deformations

Figure E.3 gives the displacement distribution in x-direction (left) and y-direction (right). The maximum displacement at the windward direction is 2.66m. The displacement in y-direction shows the ovalization deformation of the upper cone and it has a maximum displacement around 1m.

E.3. First principal strain distribution

Figure E.3 gives the first principal crack distribution within the allowable value (0.0009018) and exceeding the allowable range. A maximum principal strain with a magnitude of 0.024 is found at the throat height at the last load step. The large strains are located at the stiffening rings and the shell walls near the stiffening rings.

E.4. Crack strain distribution

Figure E.4 is the cracking distribution on the inner and outer shell wall under wind load D+2W. No kinks are observed in the upper cone, while the circular cross-section does change to an ellipsoid shape. The crack on the shell walls at the windward side and two cross sides are observed. The largest crack is observed at the throat height. A large horizontal crack is found at the throat height due to the overturning effect of the large horizontal wind load. The maximum crack width is 6.188mm.

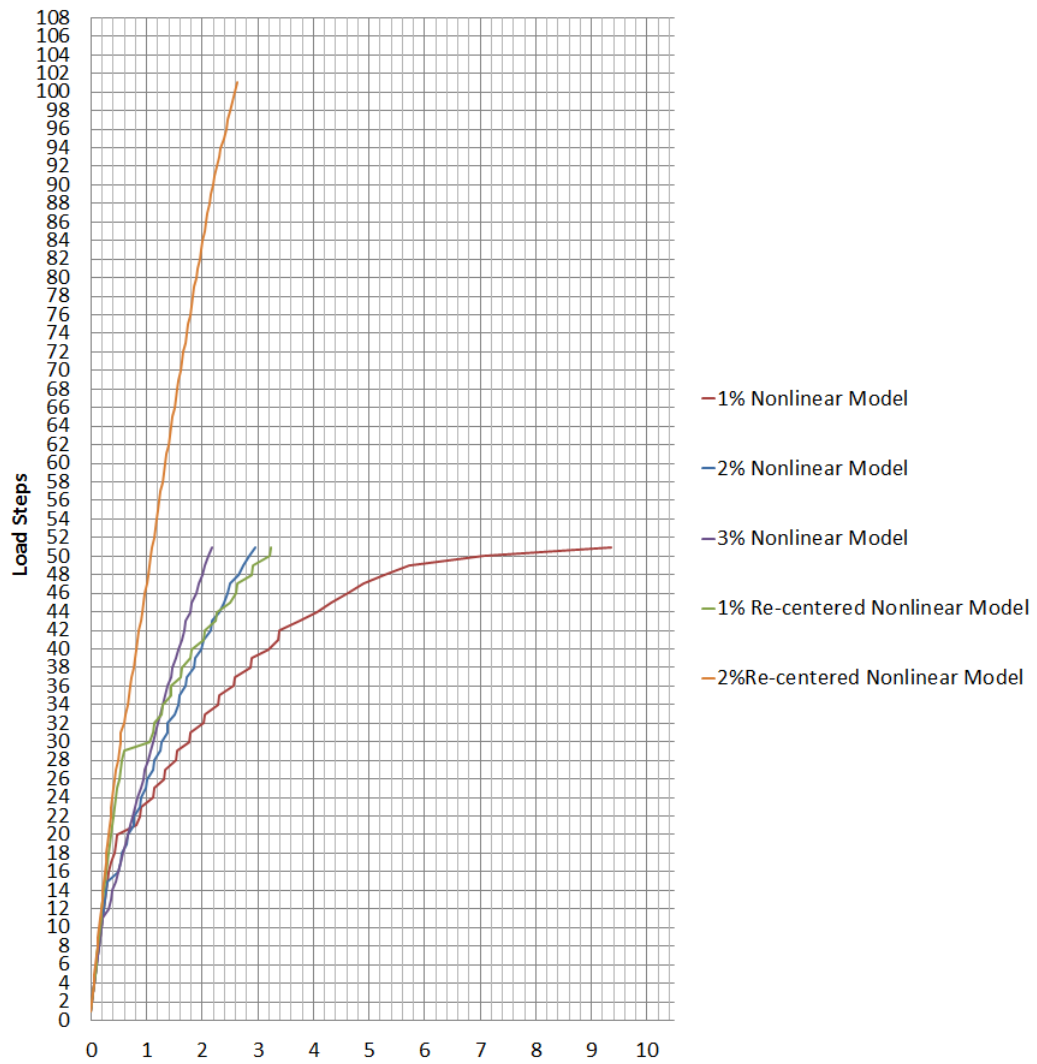


Figure E.1: Load steps-displacement curve for 1%NM, 2%NM, 3%NM 2%RNM, 1%RNM

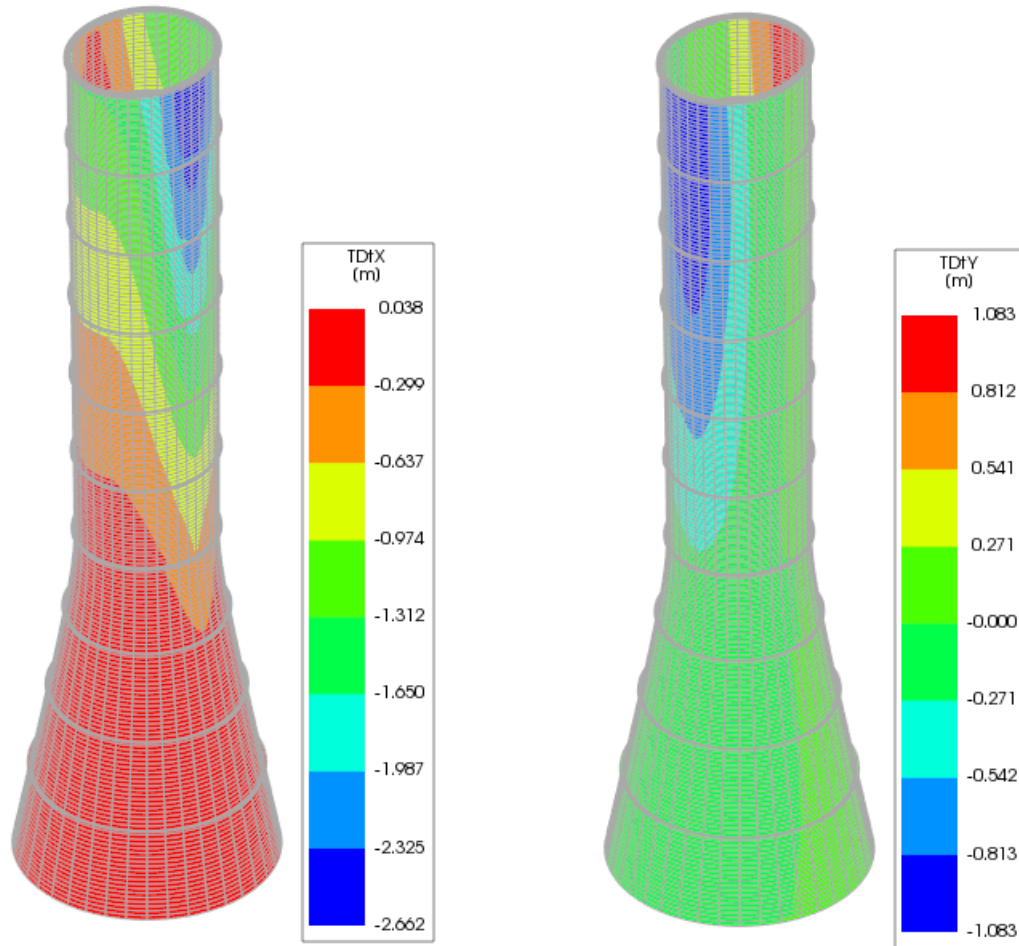


Figure E.2: The deformed shape with displacement distribution in x direction (left) and y direction (right) for 2%RNM under D+2W

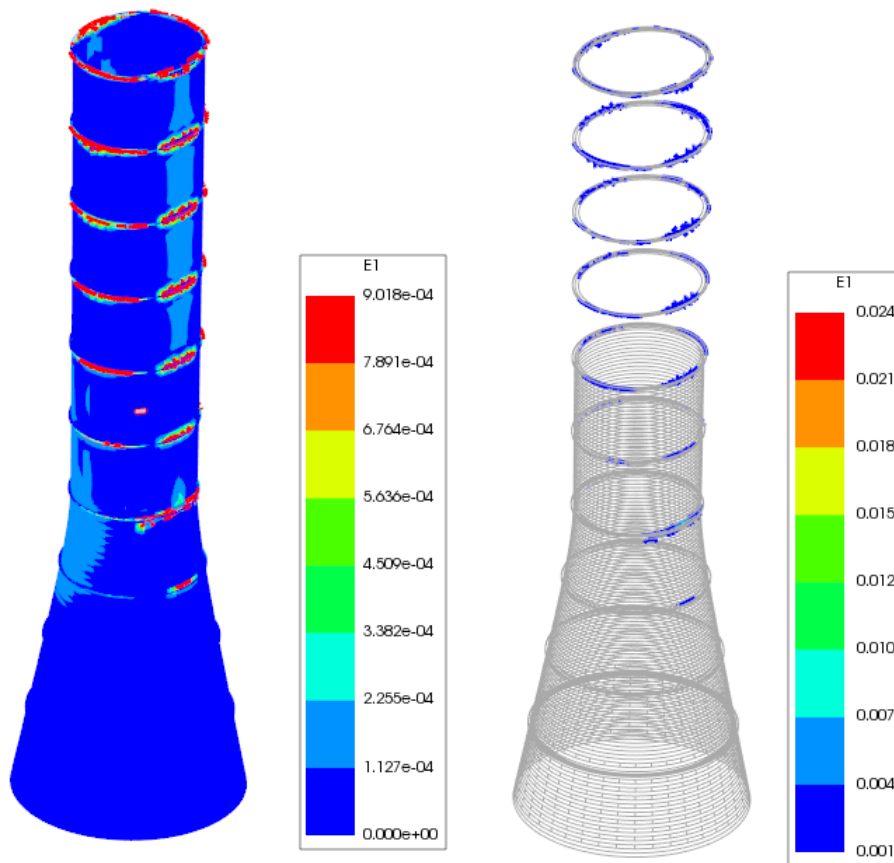


Figure E.3: The maximum principal strain within the allowable range(0.0009018)(left) The maximum principal strain that exceed the allowable rang (right) for 2%RNM at D+2W

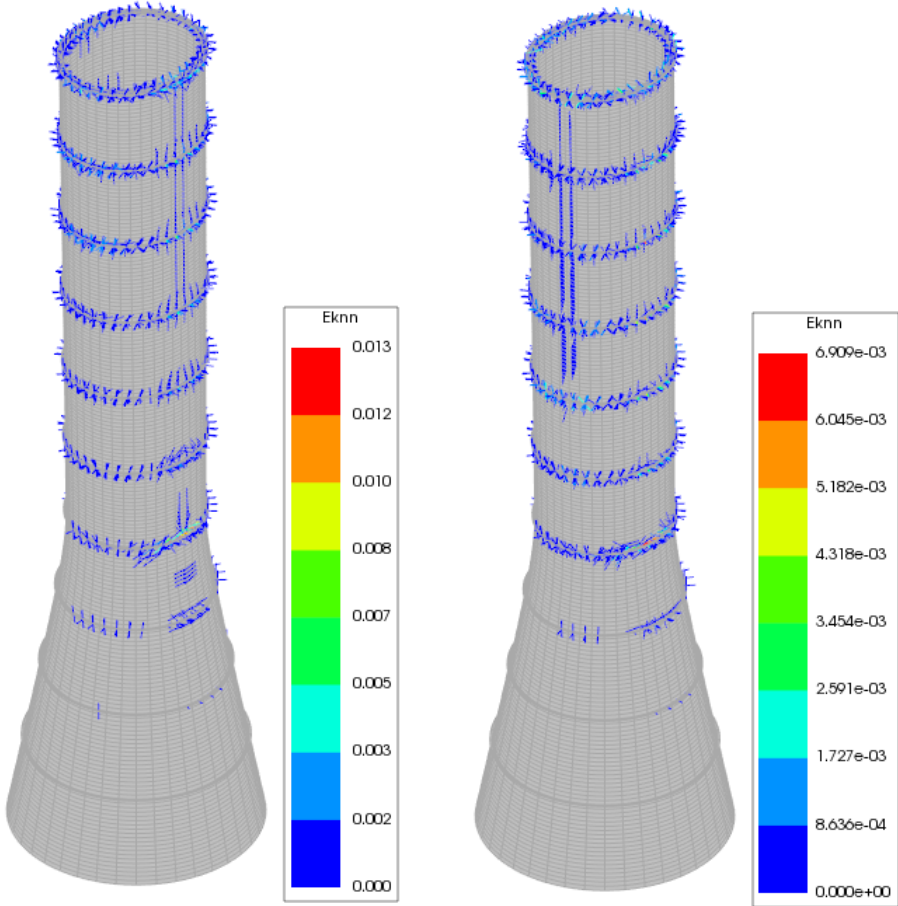


Figure E.4: The crack strian distribution at outer layer(left) and inner layer(right) for 2%RNM at D+2W

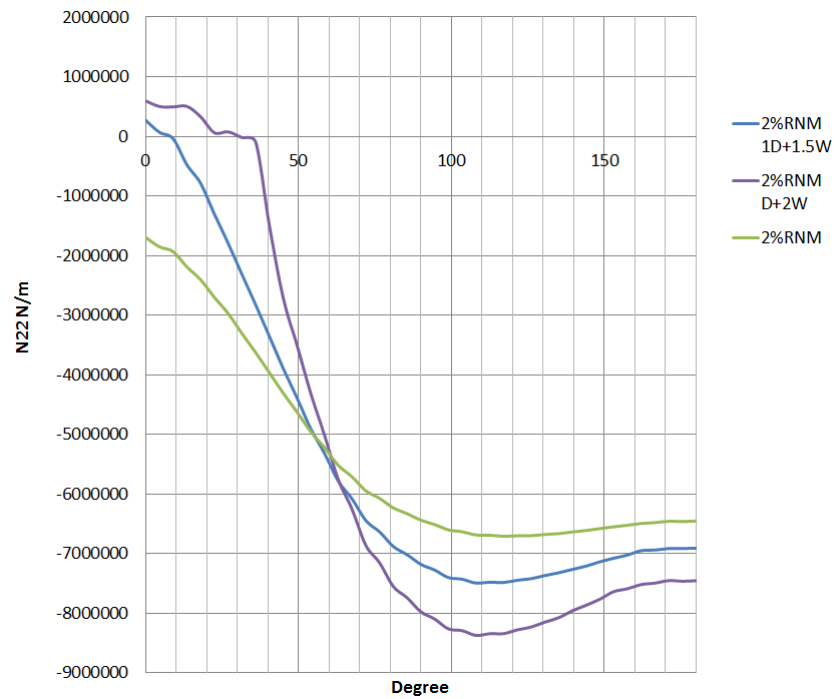


Figure E.5: The crack strain distribution at outer layer(left) and inner layer(right) for for model 2%RNM at D+W, D+1.5W and D+2W

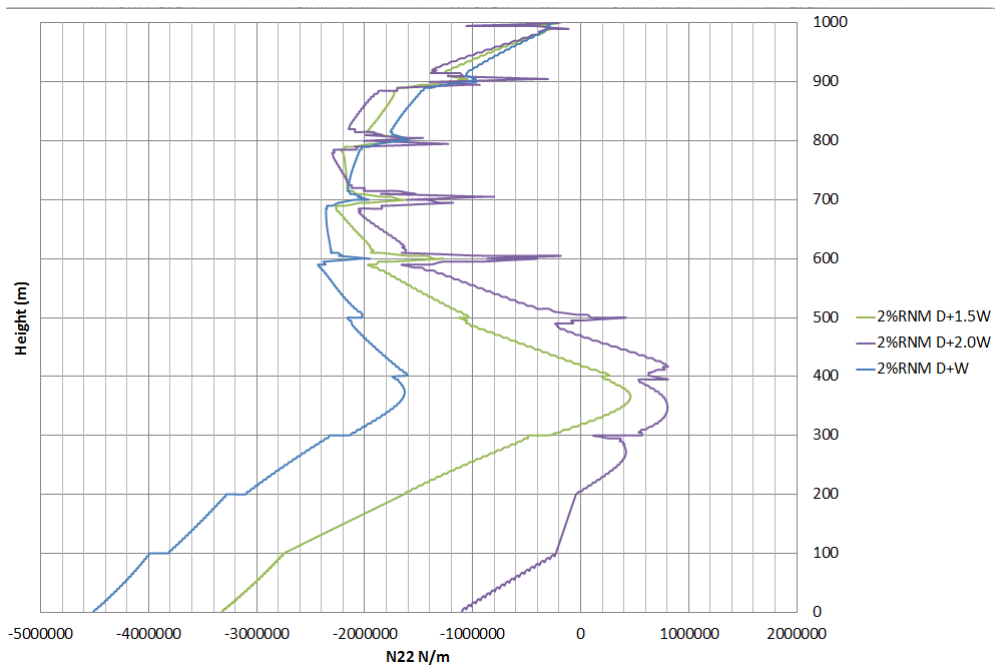


Figure E.6: The meridional stress resultant over height for model 2%RNM at D+W, D+1.5W and D+2W

E.5. Stress resultant in the meridional direction

Figure E.5 gives the meridional stress resultant at the throat height over the circumference. As can be seen, at ultimate limit state with wind load factor of 1.5, a tensile force is found at the throat height, which should be further improved in the future research.

List of Figures

1.1	The solar updraft tower power plant schematic (Gannon (2002)).	2
2.1	Parameter indication on the geometry and the shell wall thickness over height.	9
2.2	Minimum tilt angle of hyperbola at the base.	12
2.3	Geometry of design model of Krätzig & Partner	14
2.4	Drawing of the top and intermediate stiffening rings by Krätzig & Partner, Germany (Lupi et al., 2015)(Niemann et al., 2009)	14
3.1	The Ekman spirial (Lupi et al. (2015))	18
3.2	The mean wind profiles for different terrains (P. Mendis and Cheung (2007)).	19
3.3	Description of terrain roughness lengths, z_o (ISO04353 (2012)).	21
3.4	Free stream wind velocity[m/s](left); free stream wind pressure[Pa](right).	23
3.5	Types of circumferential pressure distribution (Phillip L. Gould; Wilfried B (2005)).	25
3.6	Surface roughness and types of pressure distribution (Phillip L. Gould; Wilfried B (2005)).	26
3.7	Pressure coefficient in the circumferential direction	27
4.1	Procedures for building up the FEM, 1 st Determine the compound points, 2 nd Connect point by 3D lines, 3 rd Revolution around central z axis, 4 th Mesh the geometry, 5 th Setting boundary conditions, 6 th Adding loads.	30
4.2	Stress-strain relation for reinforcement (EN1992-1-1 (2011))	32
4.3	Mesh scale from very coarse(1 st) coarse(2 nd), intermediate(3 rd), fine(4 th), very fine(5 th).	33
4.4	The mesh refinement of the top stiffening ring before(left) and after refinement(right)	33
4.5	Natural frequencies with different mesh densities with curved shell element modeling the stiffness rings(top) and Natural frequencies with different mesh densities for beam element modeling the stiffening ring ((Eck et al., 2015))(bottom)	34
4.6	Finite element model of solar updraft tower(left) and finite element model of the connection between the shell wall with the intermediate ring(middle) and top stiffening ring(right)	35
4.7	Natural frequencies of curved shell element model and 3D solid element model	36
4.8	Mesh of cross-section of the top(right) and intermediate(left) stiffening ring	37
4.9	Eigenfrequencies of curved shell model with precise geometry and beam model with precise geometry	37
4.10	Bar particles in beam element (top) and grid reinforcement in curved shell element (bottom) (DIANA (2016))	38
4.11	Integration schemes in quadrilateral zone (DIANA (2016))	40
4.12	Boundary conditions of the solar updraft tower	40
5.1	Comparison among the calculated eigenfrequencies of Simple Linear Model, results from Eck et al. (2015) and results from the literature Harte and Krätzig (2011)	45
5.2	The first 6 free vibration mode shapes for Simple Linear Model the 1 st (most left) and the 6 th (most right)	46
5.3	Deformed chimney (factor 30) with displacement distribution in the windward direction(left) and the cross-wind direction(right) under D+1.5W -Simple Linear Model	47

5.4	Comparison of in-plane meridional stress resultant distribution over height between literature Eck et al. (2015)(left) and Simple Linear Model(middle), the location that stress resultant distribution is calculated (right)	47
5.5	Circumferential stress distribution on the shell walls (left) meridional stress distribution on the shell walls(middle) and circumferential stress distribution on the stiffening rings(right) for Simple Linear Model (1D+1.5W)	48
5.6	The first 15 natural frequencies of Simple Linear Model and Detailed Linear Model . . .	49
5.7	First 6 free vibration mode shapes for Detailed Linear Model (1 st (most left)-6 th (most right))	49
5.8	Global and local displacement of Simple Linear Model and Detailed Linear Model (left) and top view of deformed tower for Simple Linear Model and Detailed Linear Model(right) (1D+1,5W)	50
5.9	In-plane meridional stress resultant distribution over height of Simple Linear Model and Detailed Linear Model(left) and In-plane meridional stress resultant distribution at throat height over the circumference (right) (1D+1.5W)	51
6.1	Development of equivalent shear retention factor for coaxial rotating crack result (J.G (1988))	55
6.2	The formation of secondary crack (Goto.Y. (1971))	57
6.3	Stages of load-deformation behavior of a reinforced concrete tensile member (Goto.Y. (1971))	57
6.4	The tension stiffening curve with varying reinforcement ratios(left) Stress-strain relationship of concrete in tension(right)	58
6.5	Thorenfeldt curve for concrete compressive behavior (DIANA (2016))	59
6.6	The reduction factor by lateral crack(left) The stress-strain compressive curve for concrete after the lateral crack is taken into account(right) (DIANA (2016))	61
6.7	Influence of lateral confinement on compressive stress-strain curve(left); Compressive behavior under lateral confinement (right) (DIANA (2016))	62
6.8	Stress-strain relation for reinforcement bar	64
7.1	Modified Newton-Raphson iteration (DIANA (2016))	67
7.2	Load steps-displacement curve for 1%NM integration scheme of 5-points Simpson and 7-points Simpson in thickness direction	68
7.3	Load steps-deflection curve for nonlinear analysis for Shell Nonlinear Model, Beam Nonlinear Model, Shell no Transverse Nonlinear Model	70
7.4	The meridional stress resultant for shell walls at windward side of the tower of SNM under self-weight	71
7.5	The crack strain distribution on the shell wall under self-weight(left); the crack distribution on the stiffening rings (right up); the deflected shape of stiffening rings under self-weight(right-down) (SNM)	71
7.6	The maximum crack strain at the stiffening rings under self-weight (SNM)	72
7.7	The crack distribution of SNM from load step 3 to 17	73
7.8	Principal strain distribution of the intermediate ring (900m) for SNM	73
7.9	The comparison between concrete cracking model of the stiffening rings with maximum crack growth until load step 20 for SNM	74
7.10	The comparison between concrete cracking model of stiffening ring with maximum crack growth until load step 23 for SNM	75
7.11	The crack distribution of SNW of step 19 (1 st), step 20 (2 nd), step 21 (3 rd), step 22 (4 th) and their deformed shape of the top stiffening ring	75
7.12	The deformation of Beam Nonlinear Model from load step 16 to 23 with normalized deformation	76

7.13	deformed shape for SNM and DLM with factor of 10 and the contour plot is the displacement in windward direction	77
7.14	Global displacement of Shell Nonlinear Model and Detailed Linear Model at last load step(1D+1W)	78
7.15	Local displacement of SNM and DLM at the last load step(1D+1W)	78
7.16	Crack strain distribution that exceeds the maximum allowable value for the 5 layer from inner to outer (top) Crack strain distribution for 5 layers from inner to outer of SNM(bottom)	80
7.17	Concrete stress-strain curve at a critical point(left); the strain distribution in the circumferential direction(right)	81
7.18	The distribution of concrete crushing in the circumferential direction(left) and the meridional direction(right) for SNM at 1D+1W	82
7.19	N22 stress resultant distribution over height for Shell Nonlinear Model and Detailed Linear Model at 1D+1W	82
7.20	Tensile stress distribution in the meridional direction for Beam Nonlinear Model(left) Shell Nonlinear Model(middle) and Linear Model(right)	83
7.21	N22 in the circumferential direction at throat height for Shell nonlinear Model and Beam Nonlinear Model	84
7.22	Yielding reinforcement distribution in the meridional direction(left) and the circumferential direction(right)	85
8.1	The load steps-deflection curve for model 1%NM, 2%NM, 3%NM	88
8.2	The load steps-displacement curve for A1, A2, A3 (left); The load steps-displacement curve for B1, B2 (right).	89
8.3	The load steps-displacement curve for model 1%NM(red), A1 (blue), B1 (purple)	90
8.4	The maximum tensile principal strain development at inner shell layer for model 1% Nonlinear Model, 2% Nonlinear Model, 3% Nonlinear Model	91
8.5	The deformed shape for 3%NM(left), 2%NM(middle), 1\$NM(right)	91
8.6	the global displacement in the windward direction over height (1D+1W) for model 1% Nonlinear Model, 2%Nonlinear Model, 3%Nonlinear Model (left),The local displacement in the windward direction over height (1D+1W) for model 1% Nonlinear Model, 2% Nonlinear Model, 3% Nonlinear Model(right)	92
8.7	The crack strain distribution of the model 1% Nonlinear Model; 2% Nonlinear Model; 3% Nonlinear Model	93
8.8	The crack strain distribution exceeds the allowable value of the model 1% Nonlinear Model; 2% Nonlinear Model; 3% Nonlinear Model	93
8.9	The crushed concrete distribution of the tower for 1% Nonlinear Model, 2% Nonlinear Model, 3% Nonlinear Model	94
8.10	The yielding reinforcement distribution in the meridional direction of the model 1% Nonlinear Model, 2% Nonlinear Model, 3% Nonlinear Model	95
8.11	The yielding reinforcement distribution in circumferential direction of the model 1% Nonlinear Model, 2% Nonlinear Model, 3% Nonlinear Model	95
8.12	The tensile stress resultant in the meridional direction distribution 1% Nonlinear Model, 2% Nonlinear Model, 3% Nonlinear Model	96
8.13	The configuration of the ring-wall connection for the Shell Nonlinear Model and Recentered Nonlinear Model	96
8.14	Load steps-deflection curve for Recentered model and Shell Nonlinear Model	97
8.15	The crack initiation of 1% Recentered Nonlinear Model from load step 10 to 20.	98
8.16	Principal strain development for 1%RNM, 2%RNM, 1%NM, 2%NM	99
8.17	Topview of 1%RNM(left) and 2%RNM(right) at the last load step (1D+1W)	100
8.18	The global displacement of in the windward direction 1%RNM, 2%RNM, 1%NM, 2%NM, DLM at the last load step(1D+1W)	100

8.19	The local displacement of 1%RNM, 2%RNM, 1%NM, 2%NM, DLM at the last load step(1D+1W)	101
8.20	The principal strain distribution of 1%RNM and 2%RNM before and after the discontinuity	102
8.21	The crack strain distribution of 1%RNM and 2%RNM at the last load step (1D+1W) . . .	102
8.22	The crack strain distribution exceeding the allowable value of 1%RNM and 2%RNM at the last load step (1D+1W))	103
8.23	Principal strain development for 1%RNM, 2%RNM, 1%NM, 2%NM	104
8.24	The principal strain distribution of the top ring for 1% Nonlinear Model	105
8.25	The principal strain distribution of top ring for 2% Nonlinear Model	105
8.26	The principal strain distribution of top ring for 1% Recentered Nonlinear Model	106
8.27	The principal strain distribution of top ring for 2% Recentered Nonlinear Model	106
10.1	Load steps-deflection curve	114
A.1	Circumferential distributions of meridional resultant stresses at the ultimate limit state (D+1.5W) Comparison between 1-km tower with ten or seven rings (Lupi (2009))	120
A.2	Parabolic curve for concrete in compression (DIANA (2016))	121
A.3	Hognestad stress-strain relation for concrete in compression (DIANA (2016))	122
A.4	Stress-strain relation according to EN 1992-1-1 for concrete in compression(DIANA (2016))	123
A.5	Stress-strain relation of different concrete cracking model (DIANA (2016))	125
A.6	The tension stiffening model and the linear ultimate strain model used in the FEM . . .	126
A.7	Pressure coefficient over circumference of solar updraft tower	128
B.1	5x10m slab model with meshing and boundary conditions details	131
B.2	Crack strain for one layer reinforcement and two layer reinforcement layout	131
C.1	Cauchy stress on a unit cube in their positive direction (DIANA (2016))	133
C.2	CQ40S-QUADRILATERAL, 8 nodes and Axis for three dimensional beam (DIANA (2016))	134
C.3	Drawing of top and intermediate stiffening ring by Krätzig & Partner, Germany (Lupi et al., 2015)(Niemann et al., 2009)	136
C.4	Displacement distribution in vertical direction for Beam Ring Model(left) and Shell Ring Model(right) at load step 71	136
D.1	Displacement in y direction for models 1%NM, 2%NM, 3%NM, 2%RNM,1%RNM	140
D.2	The maximum principal strain distribution(0-0.0009018) for models 1%NM, 2%NM, 3%NM, 2%RNM,1%RNM	141
D.3	The maximum principal strain distribution(0.0009018-max) for models 1%NM, 2%NM, 3%NM, 2%RNM,1%RNM	142
D.4	The meridional stress distribution at the windward direction for 1%NM, 2%NM, 3%NM	143
D.5	The meridional stress distribution at the windward direction for 2%RNM,1%RNM	144
D.6	The comparison of meridional stress distribution at the windward direction for 1%NM, 2%NM, 3%NM(left);the comparison of meridional stress distribution at the windward direction for 2%RNM, 2%NM, DLM(left)	144
D.7	The comparison of meridional stress distribution at the windward direction for 2%RNM, 1%RNM(left);the comparison of meridional stress distribution at the windward direction for 1%RNM, 1%NM,(right)	145
D.8	The comparison of meridional stress distribution at the windward direction at the thorat height over the circumference for 1%RNM, 2%RNM, DLM; the comparison of meridional stress distribution at the windward direction at the thorat height over the circumference for 2%NM, 3%NM, 1%NM	145
D.9	The comparison of meridional stress distribution at the windward direction at the thorat height over the circumference for 2%NM, 3%NM, 1%NM, 1%RNM, 2%RNM, DLM	146

E.1	Load steps-displacement curve for 1%NM, 2%NM, 3%NM 2%RNM, 1%RNM	148
E.2	The deformed shape with displacement distribution in x direction (left) and y direction (right) for 2%RNM under D+2W	149
E.3	The maximum principal strain within the allowable range(0.0009018)(left) The maximum principal strain that exceed the allowable rang (right) for 2%RNM at D+2W	150
E.4	The crack strian distribution at outer layer(left) and inner layer(right) for 2%RNM at D+2W	151
E.5	The crack strian distribution at outer layer(left) and inner layer(right) for for model 2%RNM at D+W, D+1.5W and D+2W	152
E.6	The meridional stress resultant over height for model 2%RNM at D+W, D+1.5W and D+2W	152

List of Tables

2.1	Geometry details of the design model of Krätzig & Partner	13
3.1	Averaging peak factors and evaluation of reference averaging time factor (ISO04353 (2012)).	20
3.2	Correction factor for other return period (ASCE7 (2013)).	21
3.3	Roughness parameter and pressure distribution n curve with different types of ribs(Phillip L. Gould; Wilfried B (2005)).	25
3.4	Function of pressure coefficient over circumferential direction(Phillip L. Gould; Wilfried B (2005)).	26
4.1	Cross-sectional properties of stiffening ring	38
5.1	Verification of eigenfrequency and their error margin among Simple Linear Model and result from Eck et al. (2015) and from Harte and Krätzig (2011)	46
7.1	Concrete material properties for nonlinear analysis	66
7.2	Reinforcement material properties for nonlinear analysis	66
7.3	Reinforcement ratio setup for the shell walls	66
7.4	Reinforcement setup for stiffening rings	66
8.1	The calculated ultimate strain with different reinforcement ratios	87
8.2	The reinforcement ratio and ultimate strain of different models	89
A.1	Comparison of different finite element modeling software on modeling concrete	127
A.2	Comparison of different finite element software on modeling reinforcement	127
B.1	Concrete material properties	130
B.2	Material properties of reinforcement	130
C.1	Variable for curved shell element and Class III 3D beam element	135